THE UNIVERSITY OF MICHIGAN
DEPARTMENT OF ATMOSPHERIC AND OCEANIC SCIENCE
HIGH ALTITUDE ENGINEERING LABORATORY

Technical Report

AN INVESTIGATION INTO THE GEOCORONAL AND INTERPLANETARY HYDROGEN BALMER EMISSIONS

Sushil Kumar Atreya

ORA Project 010179

supported by:
NATIONAL SCIENCE FOUNDATION
GRANT NO. GA-28690X2
WASHINGTON, D. C.

administered through:
OFFICE OF RESEARCH ADMINISTRATION ANN ARBOR

June 1973

engn.
UMR4140

TABLE OF CONTENTS

TABLE OF CONTENTS (continued)

TABLE OF CONTENTS (continued)

LIST OF TABLES

LIST OF FIGURES

LIST OF FIGURES (continued)

LIST OF FIGURES (continued)

LIST OF FIGURES (continued)

LIST OF FIGURES (continued)

LIST OF APPENDICES

LIST OF SYMBOLS

a	azimuth angle of observation
A	etalon plate area exposed to the incident radiation
Å	angstrom
A_{ij}	Einstein transition probability from state i to state j
$A(\lambda)$	absorptivity of an optical component at wavelength λ
$A(\sigma)$	Airy function
AU	Astronomical Unit (1.5×10^{13} cm.)
b	parameter, Equation (B. 4-23)
B	constant, Appendix G
c	velocity of light
CE	charge exchange
CSR	counts per second per Rayleigh, the efficiency of the Fabry Perot interferometer used.
$\frac{du_H}{dt}$	rate of energy exchange in elastic collisions between H and O
D_α	deuterium Balmer Alpha line
D_β	deuterium Balmer Beta line
$D_f(\sigma)$	spherical plate defect function
$D_g(\sigma)$	gaussian micro-defect function
e	electronic charge
$\overline{E}$	average kinetic energy of a Maxwellian gas
f_{12}	oscillator strength for n = 1 to 2 transition
^oF	degrees Fahrenheit
$F(\sigma)$	aperture function
$\mathcal{J}_{esc}$	atomic hydrogen energy excape flux from the exobase
FSR	free spectral range

FWHM	full width at half the maximum amplitude
G	universal Gravitational constant
$G(\sigma)$	spectral density
h	Planck's constant
h	hour angle of a star or point on the celestial sphere (h = HA*), Appendix E
H	atomic hydrogen
H^+	proton
H_a	scale height at a reference altitude z_o
H_H	atomic hydrogen scale height at z_o
H_o	atomic oxygen scale height at z_o
H_α	atomic hydrogen Balmer Alpha line (6562.8Å)
H_β	atomic hydrogen Balmer Beta line (4861.3Å)
HI	neutral atomic hydrogen
HII	fully ionized atomic hydrogen
H_2^+	ionized molecular hydrogen
HA*	hour angle of a star or a point on the celestial sphere
HAO	Huntsville Airglow Observatory
HAΥ	hour angle of the first point of Aries
He	helium
i	angle of incidence of the radiation
I	a point in the interplanetary medium
ID	inner diameter
IGY	International Geophysical Year
IQSY	International Quiet Sun Year

$I_\lambda(R)$	integrated intensity (in Rayleighs) of the emission of wavelength λ
$\vec{J}$	total angular momentum
k	Boltzmann constant
k'	constant, Equation (2-19)
^oK	degrees Kelvin
$K_o(y)$	Modified Bessel function of zero order
$K_1(y)$	Modified Bessel function of the first order
$\ell n2$	natural logarithm of 2.0
$\vec{L}$	orbital angular momentum
L_α	atomic hydrogen Lyman Alpha line
L_β	atomic hydrogen Lyman Beta line
m	parameter, Equation (4-2)
m_H	mass of a hydrogen atom in gm.
m_o	mass of an oxygen atom in gm.
$(mfp)_{CE}$	mean free path for charge exchange between H and H^+
M	mass of the sun
M_H	atomic mass number of hydrogen
MAO	Michigan Airglow Observatory
MSFC	Marshall Space Flight Center
n_H	atomic hydrogen number density
n_o	atomic oxygen number density, Chapt. VI and App. G
n_o	number density of the interstellar medium surrounding the solar system
n_p	solar wind proton number density

n'_p	solar wind proton number density downstream of the shock boundary
$n(H\mid 1)$	number density of interplanetary hydrogen atoms in the ground state
N_n	population of the n^{th} excited state of atomic hydrogen, normalized by the ground state hydrogen number density
N_2	molecular nitrogen gas
Ne	neon
NES	North - East - South quadrants
NWS	North - West - South quadrants
O	atomic oxygen
OD	outer diameter
OGO	Orbiting Geophysical Observatory
OH	hydroxyl
OI	neutral atomic oxygen
O_2	molecular oxygen
p	pressure of the scanning gas in PSI
pc	parsec (1 pc = 2.5 AU)
$P_n(\text{direct})$	direct production rate of the n^{th} excited state of atomic hydrogen
PSI	pressure of the gas in pounds per square inch
Q_e	quantum efficiency of the photomultiplier tube
r	distance from the sun in AU, Appendices B. 1 and B. 3
$\vec{r}$	radius vector between I and the earth, Fig. 6
r_c	characteristic distance from the sun where the interplanetary hydrogen density drops to 1/eth its value at infinity
r_e	radius of the earth

r_o	mean distance between the earth and the sun, Appendix B. 1
R	Rayleigh, unit of the intensity of radiation
$\vec{R}$	radius vector between I and the sun, Fig. 6
R_e	mean distance between the earth and the sun, Fig. 6
R_{rs}	ratio of L_α radiation pressure to the solar gravitational force
R_{sc}	satellite critical altitude
R_y	intensity of the source in Rayleighs
$R(\lambda)$	reflectivity of an optical component at wavelength λ
RA	Right Ascension
S	spin angular momentum
$S(\lambda)$	intensity of the source - Dark current, Appendix C
SF_6	sulfur hexafluoride gas
t	spacing between the Fabry - Perot plates
T	temperature of the emitting gas
T'	difference between T_H and T_O
T_H	kinetic temperature of hydrogen gas
T_O	kinetic temperature of the oxygen gas
$T(\lambda)$	transmission of an optical component at wavelength λ
UV	ultraviolet
v	velocity of hydrogen atoms at the moment of release from the cosmic dust
v_o	orbital velocity of the earth
v_p	solar wind velocity
V_o	velocity vector of the interplanetary hydrogen gas

$V_\odot$	solar system apex velocity
V_r	line of sight component of the interplanetary hydrogen velocity
V_{IP}	velocity vector of interplanetary hydrogen gas
V_{IS}	interstellar hydrogen velocity vector
w	variable, Equation (B. 4-24)
$W(\sigma)$	instrument function
x	dimensionless wavelength shift parameter, Equation (2-17)
x	celestial body, Fig. E-1
y	parameter related to z
y_u	parameter related to the exobase height z_u
Y_{max}	signal count at the peak of emission
$Y(\lambda)$	transmitted intensity - dark current, Appendix C
$Y(\sigma)$	observed signal count rate
z	altitude parameter
z	zenith angle of observation, Appendix E
z_d	height of the exobase above a certain reference altitude z_o
z_o	reference altitude
z_u	altitude of the exobase
α	coefficient, Appendix G
α_λ	atomic hydrogen absorption cross section
β	variable, Equation (B. 4-27), constant Appendix G
γ	m_H /2 kT
γ- Vel	γ- Velorum

δ	declination
$\delta(\sigma - \sigma_o)$	Dirac delta function
$\Delta\ell$	optical path difference, Equation (4-1)
$\Delta D_{1/2}$	Doppler half width in Å
$\Delta\lambda_{FSR}$	free spectral range in Å
$\Delta\sigma_{FSR}$	free spectral range in cm^{-1}
ζ- Pup	ζ- Puppis
η_λ	volume emission rate of a line of wavelength λ
θ	angle between the radii vectors $\vec{R}_s$ and $\vec{r}$, Fig. 6
λ	wavelength of emission in Å
λ_o	reference wavelength in Å
λ_o	coefficient of thermal conductivity, Chapt. VI and App. G
λ_{H_α}	wavelength of the H_α line (6562.8 Å)
ν	frequency of emission
$\overline{\nu}_{12}$	average collision frequency
$\pi\mathfrak{F}_\lambda$	solar ultraviolet flux at wavelength λ, in photons cm^{-2} sec^{-1}
σ	wavenumber (cm^{-1})
$\overline{\sigma}$	average momentum transfer cross section
σ_{CE}	charge exchange cross section for ($H^+ + H \rightleftharpoons H + H^+$)
ϕ	angle between the radii vectors $\vec{R}_e$ and $\vec{r}$, Fig. 6
ϕ	latitude of the observer, Appendix E
Ω	instrument solid angle
μ	refractive index of the scanning gas
μ'	parameter, Appendix G

ABSTRACT

AN INVESTIGATION INTO THE GEOCORONAL AND INTERPLANETARY HYDROGEN BALMER EMISSIONS

by

Sushil Kumar Atreya

The night time emission of the terrestrial hydrogen Balmer Alpha line results from the radiation transport of the solar Lyman Beta to the darkened hemisphere of the earth by multiple scattering on the atomic hydrogen of the geocorona. The volume emission rate of this line peaks quite high in the exosphere. Therefore, the temperature retrieved from the Doppler profile of such radiation should indicate the true exospheric temperature. A straightforward determination of the Doppler profile of the geocoronal Balmer Alpha line is, however, hampered by the possible presence of extraterrestrial sources of Balmer Alpha emission such as interplanetary, galactic and discrete stellar sources, or even zodiacal light and gegenschein.

In this study, the focus was on the Doppler profile measurement of the geocoronal Balmer Alpha line. In addition, the most controversial of the extraterrestrial sources, the interplanetary hydrogen was also investigated theoretically to predict its Balmer emission rates and Doppler profiles. Calculations indicate a

maximum interplanetary Balmer Alpha intensity of the order of 0.06 to 0.1 Rayleighs, with perhaps a factor of two uncertainty in this estimate. In the process of making the geocoronal hydrogen Balmer Alpha measurements, some interesting regions of the Galaxy were also looked at for the Doppler profile of the Balmer Alpha emission originating there.

Modifications were made in the existing 150 mm. diameter Fabry-Perot interferometers of the Michigan and Huntsville Airglow Observatories to measure the Doppler signature of the geocoronal and possibly extraterrestrial Balmer Alpha emission. Observations with a Fabry-Perot interferometer of maximum resolution of 0.065 Å and 0.2° field of view, were made between December 1971 and October, 1972. Several regions of the celestial sphere, believed to be devoid of any appreciable amounts of galactic and discrete stellar Balmer Alpha emission, were selected for different observing periods.

A feeble, single-line, Doppler-stationary geocoronal Balmer Alpha emission was observed. The observed emission was so weak that usually it was necessary to add the fringes obtained during a night to detect any emission features. The average measured intensity of the geocoronal Balmer Alpha emission was less than 10 Rayleighs. The measured intensities are in basic agreement with the earlier measurements and theoretical predictions for the appropriate level of the solar activity and the geometry of illumination. The measured temperatures are found to be consistently lower than the theoretical predictions of the Jacchia-model exospheric

temperatures, usually by 50 to 150°K. A closed form analytic expression for the difference between the hydrogen and the oxygen temperatures is obtained by solving the continuity equation of energy exchange in elastic collisions between the hydrogen and oxygen atoms below the exobase; and it is shown that the measured geocoronal hydrogen temperatures do indeed represent the exospheric temperatures. The heat transfer analysis also shows that at high exospheric temperatures, however, the hydrogen temperatures will be up to several hundred degrees lower than the oxygen temperatures.

No definite evidence of interplanetary hydrogen Balmer Alpha emission was found in the present measurements.

A few scans were also made in the plane of the Galaxy. Only scans made with the viewing mirrors looking into the Vela-Puppis region showed any detectable amount of Balmer Alpha emission. An enhancement of the emission was noticed in the vicinity of γ - Velorum - ζ-Puppis region. A double-line profile, characteristic of the recombination line emission, was observed. It was found to be somewhat Doppler shifted from the laboratory position of the Balmer Alpha line. The lower limits on its temperature and intensity were found to be approximately 5500°K and 16 Rayleighs respectively. The concentration of emission in the Vela region is in agreement with the theory and the Mariner 5 measurements, but is contrary to the Mariner 6 results.

CHAPTER I

INTRODUCTION

It is only over the past two decades that the presence of atomic' hydrogen in the upper atmosphere of the earth has been well understood. Fig. 1 taken from Wegener (1911) illustrates the state of knowledge about terrestrial hydrogen in the early part of the twentieth century. According to Wegener, hydrogen in the 'molecular' form was believed to be present as a minor constituent in the lower regions of the atmosphere and it became the dominant species in the 'Wasserstoff-Sphäre.' The outermost region of the atmosphere was called 'Geocoronium Sphäre' and thought to be composed entirely of a hypothetical element called 'Geocoronium' with atomic weight less than 1/2 that of atomic hydrogen. Geocoronium was believed to exist as a trace element (5.8 parts to a million) in the troposphere. Over the next forty years, with improved understanding of the thermal structure, escape phenomenon of light gases, and the diffusive separation of gases in the terrestrial atmosphere, Wegener's (1911) picture of the atmosphere was considerably modified.

However, it was only after Meinel's (1950) discovery of the hydroxyl vibration-rotation bands in the nightglow and Bates and Nicolet's (1950) investigation of the Dand E region photochemistry, that the presence of atomic hydrogen in the upper atmosphere of the earth was truly established. Below 100 km., atomic hydrogen is mainly produced by the photodissociation of water vapor, methane and ammonia (Nicolet, 1970). From the region of its production, atomic hydrogen diffuses upward and, because of its low mass and

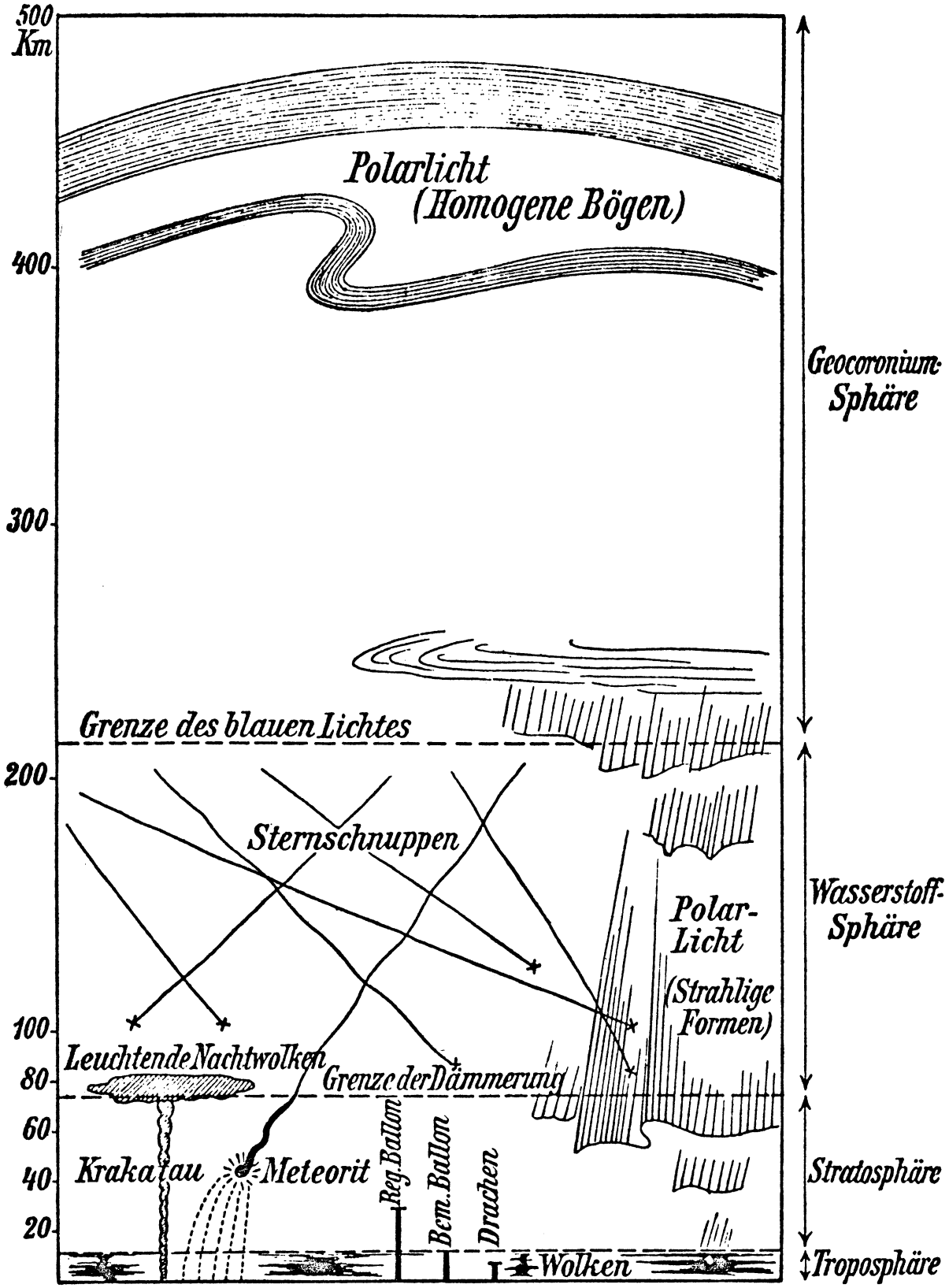

Fig. 1. Querschnitt der Atmosphäre (Wegener, 1911).

the large temperature prevalent in the exosphere, it eventually escapes the terrestrial atmosphere. The outermost region of the atmosphere is therefore compœs ed mostly of atomic hydrogen. Since 1950, many people in the U. S. S. R., France, Bolivia and U. S. A. have attempted to investigate this outermost part of the earth's atmosphere, the geocorona, by making photometric measurements of the hydrogen emissions which might originate there. However, since hydrogen is the most abundant element in the cosmos, there are other possible sources of hydrogen emission besides the geocoronal one.

The non-auroral hydrogen emissions can be classified into two broad categories - the terrestrial and the extraterrestrial hydrogen emission. Hydrogen emissions resulting from the excitation of neutral atomic hydrogen in the earth's extended atmosphere, either on fluorescence scattering of the solar UV or by electron excitation, are classified in the first group. Amongst the extra-terrestrial sources, the significant ones are interplanetary, discrete stellar and galactic emissions and the zodiacal light and gegenschein.

The emission rate of the geocoronal hydrogen Balmer Alpha (H_α) line peaks quite high in the exosphere (Meier 1969), therefore, its Doppler profile is capable of yielding the 'true' exospheric temperature. Thus it is possible to obtain information of geophysical interest by studying the Doppler profiles of the geocoronal H_α line.

The present study concentrates on the investigation of

the Doppler profile of the geocoronal H_α emission line by means of a ground based, high resolution optical device. Theoretical calculations leading to the intensity and Doppler profile of the interplanetary H_α lines are also carried out. In the process of making the geocoronal H_α measurements, a few selected regions of the Galaxy were also looked at for the Doppler profiles of the H_α emission originating there.

A straightforward measurement of the geocoronal H_α Doppler profile is not possible because of the possible contamination by the non-geocoronal sources. Therefore, in order to design an experiment which will spectroscopically discriminate the geocoronal H_α Doppler profile from the various undesired sources of H_α emission, it is essential to examine the nature of each of these sources individually.

Chapter II is devoted to a discussion of the most important extraterrestrial sources of H_α emission, namely the galactic, zodiacal light and gegenschein, and the interplanetary sources. In Sec. 2.2 and 2.3, the nature of the galactic emission, zodiacal light and the gegenschein is reviewed and it is concluded that, for certain selected viewing directions and geometries of illumination, these sources of H_α emission will not interfere with the high resolution measurement of the geocoronal H_α line. In order to evaluate the intensity and the Doppler signature of the interplanetary H_α emission, certain basic parameters such as density distribution, temperature, velocity and the trajectory of the interplanetary atomic hydrogen are needed. Therefore, both the observations and the theoretical models

of the interplanetary atomic hydrogen are critically reviewed in Sec. 2.4 and 2.5. Having established the most feasible values for the required parameters from this review, a general calculation of the fluorescence scattering of the solar UV on interplanetary atomic hydrogen is carried out and the maximum possible H_α and H_β intensities evaluated in Sec. 2.6. Finally, the expected Doppler profiles of the interplanetary hydrogen emissions are evaluated theoretically in Sec. 2.7. It is concluded that the interplanetary H_α is extremely feeble.

The observations of the geocoronal H_α emission, atomic hydrogen distribution and the results obtained from the radiative transport theory of earlier authors are reviewed in Chapter III. The knowledge gathered in Chapters II and III is essential to the design of an experiment for the proposed study.

An outline of the theory of the instrument used, and a discussion on the selection and justification of the values of various instrument parameters are contained in Chapter IV. A Fabry-Perot interferometer of full field of view of 0.2° and a resolution of nearly $0.065\ \mathring{A}$ at the H_α wavelength ($6562.8\ \mathring{A}$), with an H_α filter of pass-band $\leq 3\mathring{A}$, was found to be most suitable for making the Doppler profile measurements of the geocoronal and possibly the interplanetary H_α line.

For both the geocoronal and the extraterrestrial hydrogen emission measurements and, especially for the spectroscopic discrimination of one from the other, the viewing directions, integration periods, and the moon and sky conditions play a very important

role. Chapter V contains the observation schemes for the various observing periods, the representative raw data and the techniques of data reduction.

The results obtained from the reduced data and discussions are presented in Chapter VI. In particular, geocoronal temperatures and intensities are retrieved from the measured H_α Doppler profiles. Wherever possible, the results are compared against the theoretical predictions and measurements of earlier authors. The measured geocoronal hydrogen temperatures are discussed by considering the energy exchange in elastic collisions between hydrogen and oxygen atoms below the exobase. For this purpose, the appropriate continuity equation is solved and a closed form expression for the difference between hydrogen and oxygen temperatures is obtained. Finally, this chapter contains the information derived from a few isolated galactic H_α scans.

Conclusions and suggestions for future research are presented in Chapter VII.

CHAPTER II

EXTRATERRESTRIAL HYDROGEN EMISSIONS

2.1 INTRODUCTION

The nature of the galactic emission, zodiacal light, gegenschein, and the interplanetary hydrogen emission is first reviewed in this chapter. The main emphasis is on discussing the available information pertinent to high resolution observations, such as maximum intensities, regions of concentration and the Doppler widths and shifts of these various extraterrestrial components of H_α emission. Next the theoretical models and measurements of the interplanetary hydrogen are reviewed and a general theoretical formulation is carried out to evaluate the maximum possible intensity and the Doppler profile of the interplanetary H_α emission.

2.2 GALACTIC HYDROGEN EMISSIONS - REVIEW

Münch (1962) and Burbidge (1964) have presented theoretical discussions on the galactic L_α emission. Their work is based on Osterbrock's (1962) calculations of the transfer of resonance line radiation. Biermann (1970) discussed galactic L_α from the viewpoint of average life span of a galactic L_α photon. The galactic L_α photons are originally created by recombination in the fully ionized region of the interstellar gas (referred to as the H II region). Münch (1962) has pointed out that the major contribution to the galactic L_α arises from the flux beyond the Lyman limit from the OB-type stars which are highly concentrated to the plane of the Galaxy. According to Münch (1962) the diffuse galactic L_α may be more intense in the vicinity of nearby B-type stars and

in that part of the H II region excited by γ-Velorum (γ -Vel) and ζ-Puppis (ζ -Pup). Tinsley (1969) has suggested the possibility of L_α sources along the galactic equator associated with gaseous nebulae.

The L_α photons created in the H II region must escape it before they can enter the neutral interstellar region (referred to as the H I region). Auer (1968) points out that if there is any appreciable amount of dust in the H II region, the L_α photon may be absorbed by it without ever getting a chance to escape the H II region. If the L_α photon does escape the H II region, it will have a double peaked profile with each peak nearly three Doppler widths (at $10^4\,^oK$) removed from the line center (Auer, 1968). The galactic L_α photon after escape from the H II region, undergoes multiple scattering in its passage through the H I region and is eventually annihilated by the dust grains in the interstellar H I region.

Münch (1962) estimated that the mean free path for annihilation of a galactic L_α photon in the H I region is 50 pc (1 pc (parsec) = 2×10^5 AU). The L_α photons perform random walk over such large distances and in the process undergo multiple scattering. Consequently, the probability of photon absorption on the dust grain becomes more pronounced toward the line center than in the wings. In addition, thermal motion of the scattering atoms causes redistribution or diffusion in frequency space (Auer, 1968). The result of such propagation of the L_α photon through the interstellar medium is that the galactic emission will appear significantly broadened. Adams (1971) has carried out calculations to determine the galactic L_α line widths. In his approximation, Adams (1971) assumed that all L_α

photons escape the H II region without ever getting destroyed there. Depending upon the suspected range of values for the thickness of the galactic plane, Adams (1971) found the galactic L_α line widths of the order of 1 to 3 Å.

Adams (1971) has calculated a highly isotropic galactic L_α emission of 200 R, a value surprisingly close to the one measured by the OGO V L_α detectors in the 'downwind' direction (i.e., opposite the direction of approach of interplanetary hydrogen into the inner solar system). This 200R of isotropic galactic L_α emission forms the basis for the 'cold model' of Thomas (1971) and Bertaux et. al. (1972) discussed in Section 2.5.7. Blum (1972) estimated an isotropic galactic L_α emission of 140R, a value nearly 60R smaller than seen by OGO V in the downwind region. Blum notes that there are considerable uncertainties in his estimate of this isotropic galactic L_α emission. According to Blum's (1972) model 60R difference in the downwind region L_α is provided by an anisotropic distribution of interplanetary hydrogen. Barth (1970) has reported the L_α measurements made in the plane of the Galaxy by Mariner 6 more than 8 million km past Mars. The Mariner 6 measurements showed no enhanced L_α emissions near the Vela region as were seen by Mariner 5. Also, the Mariner 6 results of Barth (1970) indicate, contrary to Münch's (1962) suggestions, that the L_α emission was concentrated not along the galactic equator nor in the H II region, but in Ophiuchus. Barth's (1970) Mariner 6 ultraviolet photometer had a spectral resolution of 10 Å and the spectrum about L_α was sampled every 2.2 Å. It is therefore difficult to discern Doppler widths and shifts from such measurements, and one can go only by Adams' (1970, 71)

predictions. Indications of isotropic galactic L_α emission over the sky were provided by the Venera 2 and 3 (Kurt and Syunyaev, 1968) and by the Venera 4 (Kurt and Dostovalov, 1968) L_α measurements. They also noticed enhanced emission in the plane of the Milky Way.

On the basis of numerous conflicting experimental evidences, it is difficult to unambiguously ascertain the regions of maximum galactic L_α brightness. There are indications of diffuse isotropic galactic L_α emission over the entire celestrial sphere and also of definite regions of enhancement toward low galactic latitudes. Galactic emission may be rendered isotropic depending upon the density of the interstellar medium in which our solar system is immersed. Galactic H_α is excited in the same manner as L_α.

Therefore, if there are regions of concentration in galactic H_α emission, they can be avoided by directing the viewing mirrors away from these regions. Likewise, the discrete stellar sources can also be avoided. This is further facilitated by the small field of view (0.2°) of the instrument used. Any diffuse, isotropic galactic H_α emission should be extremely feeble and is expected to appear as a broad continuum background over which the relatively narrow geocoronal H_α signal is superimposed. Furthermore, the geocoronal H_α emission line can be distinguished from the possible galactic H_α line by its Doppler signature. The geocoronal H_α should be Doppler stationary while the galactic H_α line is expected to be Doppler removed from the laboratory position of H_α . In addition, as explained in Appendix A, the geocoronal H_α should consist of only one fine structure component while the galactic H_α emission, which is a recombination line, should consist of two, almost equally

bright fine structure components removed from each other by nearly 0.14 Å.

2.3 ZODIACAL LIGHT AND GEGENSCHEIN - REVIEW

On clear moonless nights, zodiacal light may be observed in the early morning and early evening twilight (i.e., for solar depression angles less than 10 - 15°). The light is oriented along the ecliptic with intensity increasing toward the sun. The visible faint cone is sometimes 20 to 30° wide at the base and nearly extends to the zenith. It is best observable from low latitudes where the ecliptic is almost overhead.

The zodiacal light shows normal solar spectra without enhancement of the nightglow emissions (Roach et. al., 1954, Weinberg, 1967). It is therefore suspected to be the result of the sunlight scattered by the interplanetary matter. Such scattering has two major implications in regard to the Doppler profile of the solar lines. The original solar Fraunhofer absorption lines are typically an angstrom in half width. The interplanetary matter is composed, mainly of high energy free electrons and microscopic dust grains. The scattering of sunlight off these high velocity free electrons results in the Doppler broadening of the absorption lines and the dust grains in orbit around the sun (supposedly in the same sense as the earth) introduce a Doppler shift in the already broadened absorption lines. Therefore, the zodiacal light absorption lines may be expected to be several angstroms in half width and also Doppler shifted (Clarke et. al., 1967). The zodiacal light, therefore, acts like a broad continuum on which the normal nightglow emission features are superimposed.

In regard to the source of the dust component of zodiacal light, Piotrowski (1953) and Fesenkov (1959) argue that the possible source is fragmentation of the asteroid belts and Whipple (1955) finds that cometry debris plays a major role in supplying the interplanetary dust.

In addition to zodiacal light, which is more intense in the vicinity of the sun, there exists a faint patch of light in almost the antisolar point, which is referred to as 'counterglow' or gegenschein. It is located approximately 3^{o}W of the antisolar point and it can be detected out to about 20^{o} from its center. Gegenschein, like the zodiacal light, is suspected to be sunlight scattering off dust particles. The reason for its peculiar angular distance from the sun is yet a matter of controversy. It is hypothesized that the lunar dust cloud about the earth could be the source of the earth's dust tail blown away by solar radiation pressure and detected visually as the gegenschein.

Since the zodiacal light and gegenschein manifest themselves as a broad continuum on which the discrete emission features are superimposed, they are not expected to interfere with the proposed high resolution measurements of the geocoronal H_{α} emission. Zodiacal light can be further avoided by restricting the observations to the duration when the solar depression angle is larger than 15^{o}.

2.4 INTERPLANETARY HYDROGEN - REVIEW OF OBSERVATIONS

Clear evidence of the possible extraterrestrial source of hydrogen emission was provided by one of Morton and Purcell's (1962) high resolution measurements of Lyman Alpha (L_{α}) profile from a rocket. Morton and Purcell (1962) monitored the ultraviolet nightglow with the help of a hydrogen absorption cell flown to 177 km. altitude in

April 1961. For the absorption of L_α, atomic hydrogen in the cell was provided on dissociation of molecular hydrogen by heated tungsten filaments. L_α was transmitted to the cell through Lithium fluoride windows. The laboratory absorption profile had a maximum half width of 0.08 ± 0.02 Å.

From an altitude of 176 km. when the absorption cell unit scanned both the sky above and the earth below the rocket, two interesting results were obtained. The absorption cell completely absorbed all of the L_α radiation from below (i.e., looking down on the earth) while 15% of the L_α intensity from the sky above the rocket managed to transmit through the wings of the absorption profile of the cell. The absorption of only 85% of L_α radiation from the sky above indicated that the 'residual' 15% which was not absorbed by the cell must lie outside the 0.06 Å bandpass of the cell (0.06 Å was the smallest half width of the absorption line produced by the cell). Since geocoronal or other non-auroral terrestrial hydrogen emissions are expected to be Doppler stationary, Patterson et. al., (1963) invoked the possibility of an interplanetary neutral hydrogen source to explain the aforesaid 15% residual L_α.

Indications of extraterrestrial hydrogen were also provided by Reay and Ring's (1969) hydrogen Balmer-Beta (H_β) measurements made by means of a Fabry-Perot interferometer of 0.4 Å limiting resolution and 0.5° field of view. A slightly Doppler shifted H_β emission with intensity between 0.1 and 0.2R was recorded. In the latter part of this chapter it will be argued that this H_β emission is not likely to be of interplanetary origin.

Interplanetary L_α emission has also been measured by the L_α photometers on board a number of satellites, especially Vela-4 (Chambers et. al., 1970) and OGO-V (Thomas, 1971; Bertaux et. al., 1972). In June 1967, Vela 4 was in near circular orbit of radius 110,000 km. and its L_α detectors measured a maximum L_α intensity of 160R, in the direction:right ascension, RA= 265°; and declination, $\delta = +32^\circ$ (Chambers et. al., 1970). This direction almost coincides with the solar apex and lends support to the Blum-Fahr anisotropic model to be discussed later in this chapter.

On the basis of the OGO-V L_α measurements in December 1969, Bertaux and Blamont (1970) reported a maximum of 280R attributable to solar L_α scattering off the interplanetary atomic hydrogen. Any possible contributions due to the isotropic, diffuse galactic L_α were not subtracted out of the data. In September 1969 and April 1970, OGO-V recorded the interplanetary L_α distribution over the whole sky. (Thomas 1971; Bertaux and Blamont, 1971; Bertaux et. al., 1972). Thomas (1971) noticed in these maps that the maximum L_α intensity does not occur in the direction of the solar apex (RA=270°, $\delta = +30^\circ$) as predicted by the Blum-Fahr model. Instead, the OGO-V L_α maps showed a wide maximum region, centered around a point not too distant from the ecliptic plane and the center of gravity of the Galaxy (also called the galactic center). The maximum L_α intensity of,530R, was recorded in the direction of RA=$263\pm5^\circ$ and $\delta = -17\pm5^\circ$. From this maximum region, the L_α intensity decreased smoothly toward a wide minimum located in the opposite direction where it dropped to 215R (Thomas, 1971; Bertaux et. al., 1972). For the mean position of the L_α maximum (RA=263°, $\delta = -22^\circ$), the RA is fairly close to

the RA of the solar apex, the declination, however, differs from the solar apex declination by about 52^{o}.

Thomas (1971) argued that the Vela-4 photometers performed scans over a single great circle in the sky and therefore only a meridian of brightness rather than the precise location of brightness could be learned from the Vela-4 L_{α} measurements.

A review of the various models of the interplanetary hydrogen distribution utilizing the observational results outlined here is presented in the following section. The feasible values of the various parameters, such as interplanetary hydrogen density distribution, associated temperature and velocity of motion will be selected from this review. These parameters are required for the intensity and Doppler profile calculations of the interplanetary Balmer emission.

2.5 INTERPLANETARY HYDROGEN-REVIEW OF THEORETICAL MODELS

In the following review, the main emphasis is placed on the cosmic-dust hypothesis of Banks (1971), the thin shell model of Patterson et. al. (1963), the thick shell model of Hundhausen (1968), the anisotropic model of Blum and Fahr, and finally, the improvement on Blum and Fahr's anisotropic model for interplanetary hydrogen distribution by Thomas (1971).

2.5.1 BANKS' COSMIC DUST MODEL

Banks (1971) has hypothesized that perhaps the sun itself is the direct source of interplanetary atomic hydrogen. Some credence to this thought was provided by the findings of the Lunar Sample Preliminary Examination Team (1969). They noted that solar wind protons with energies of 1 keV, for example, could penetrate the lunar

material up to 300 Å. On penetrating the lunar soil, the solar wind nucleons transform into neutral atoms by acquiring electrons. The same phenomenon should take place on interplanetary dust. Numerous photometric observations of zodiacal light (Weinberg, 1967) have confirmed the presence of dust confined to $\pm 15^{\circ}$ of the ecliptic plane. At 1 AU, the dust grains are saturated with solar wind protons in about 8 years. Therefore, the dust in the inner solar system must have reached such a saturation limit a long time ago. After the saturation, further exposure of the dust grains to the incident solar wind results in the displacement of the trapped neutral gases.

The atomic hydrogen released on the surface de-ionization of the solar wind protons on the saturated dust grains is the main source of interplanetary hydrogen in Banks' (1971) model. Small amounts of atomic hydrogen still trapped in the dust grain tend to diffuse out when the grain acquires a high temperature in the vicinity of the Sun. Any remaining neutrals are released when the grain is eventually vaporized in the very close proximity of the Sun. The concentration of the atomic hydrogen so obtained depends upon the size distribution of the dust grain. Banks (1971) derived the values of this parameter from the experimental data of zodiacal light, collection rockets and satellites, meteors, and F-coronal emissions.

According to Banks' model, the released hydrogen atoms execute 'rectilinear' trajectories until they are lost by photoionization or charge exchange in the vicinity of the Sun. Resonance charge exchange ($H^{+}+H \rightleftharpoons H+H^{+}$) is responsible for converting nearly half of the released atoms into fast hydrogen atoms moving radially at typical solar wind speeds of 300-400 km sec^{-1}. Thus, Banks'

cosmic dust model gives two components of interplanetary hydrogen: (i) the 'cold' component, moving at relatively slower speeds; the estimated number density of the 'cold' component at 1 AU is 4×10^{-7} to 3×10^{-3} atoms $\cdot$ cm^{-3}; (ii) the 'hot' or radial component, moving at solar wind speeds of $\sim$ 400 km $\cdot$ sec^{-1}. Its concentration at 1 AU is in the range of 4×10^{-7} to 3×10^{-3} H atoms $\cdot$ cm^{-3}.

The column abundance of atomic hydrogen in Banks' model is obtained on integrating the 'sum' of the 'cold' and 'hot' components. The result is 4×10^{7} to 3×10^{11} H atoms $\cdot$ cm^{-2} column.

This wide range of values for the above parameters reflects the considerable uncertainties in the Banks' model.

2.5.2 OBJECTIONS TO THE BANKS' MODEL

There are two major difficulties with Banks' (1971) cosmic dust hypothesis, first with the trajectory of the atoms and second with the values of column abundance of atomic hydrogen. Banks claims that the hydrogen atoms released from the dust execute 'rectilinear' trajectories since the L_{α} radiation pressure is exactly balanced by the solar gravitational force. It is shown in Appendix B that even at solar maximum the ratio between these two forces is $\simeq$ 0.82 and probably a factor of 5 smaller at solar minimum. This implies that the orbits of the particles are determined always by a central law of force. The exact knowledge of the orbits is critical for predicting the Doppler signature of the interplanetary hydrogen emissions.

Banks has also attempted to interpret Reay and Ring's (1969) H_{β} observations as resulting from the fluorescence scattering of the solar L_{γ} on the cosmic dust hydrogen. To fit the observations, one needs at least a factor of 10 larger column abundance of atomic

hydrogen than the maximum allowable value obtained by Banks (1971). Furthermore, the hot component of atomic hydrogen is insignificant in producing any appreciable amounts of H_β emission. This is because the part of the solar L_γ profile responsible for exciting the ground state hydrogen, is nearly 1 Å removed from the L_γ line center (corresponding to a velocity of $\simeq$ 300 km. sec^{-1} of the radial component) where the L_γ flux has dropped appreciably (see Fig. 2 for the L_α case; L_γ situation is similar). Since in Banks' model, the 'hot' component abundance is half the total atomic hydrogen abundance, the column abundance needed to explain Reay and Ring's (1969) H_β intensities is nearly a factor of 20 larger than the maximum allowable by Banks' model. Banks' model is also not adequate to explain the features of the recent OGO V L_α measurements. It is therefore, necessary to examine various other models of interplanetary hydrogen distribution.

2.5.3 THE THIN BOUNDARY SHELL MODEL

Axford et. al. (1963) provided a theory which describes the distribution of ionized hydrogen throughout the solar system and the ultimate fate of the solar wind at large distances from the Sun. Patterson et. al. (1963) extended this work to calculate the distribution of interplanetary neutral hydrogen. According to this theory, a magnetic shock transition of the solar wind protons from macroscopic supersonic velocities to subsonic velocities occurs at a distance where the solar wind proton dynamic pressure is balanced by the interstellar magnetic field. The region of radius r_o bounded by the shock boundary is referred to as the 'heliosphere' (see illustration in Fig. 3 from Dessler, 1967). Beyond the shock boundary, the solar wind proton

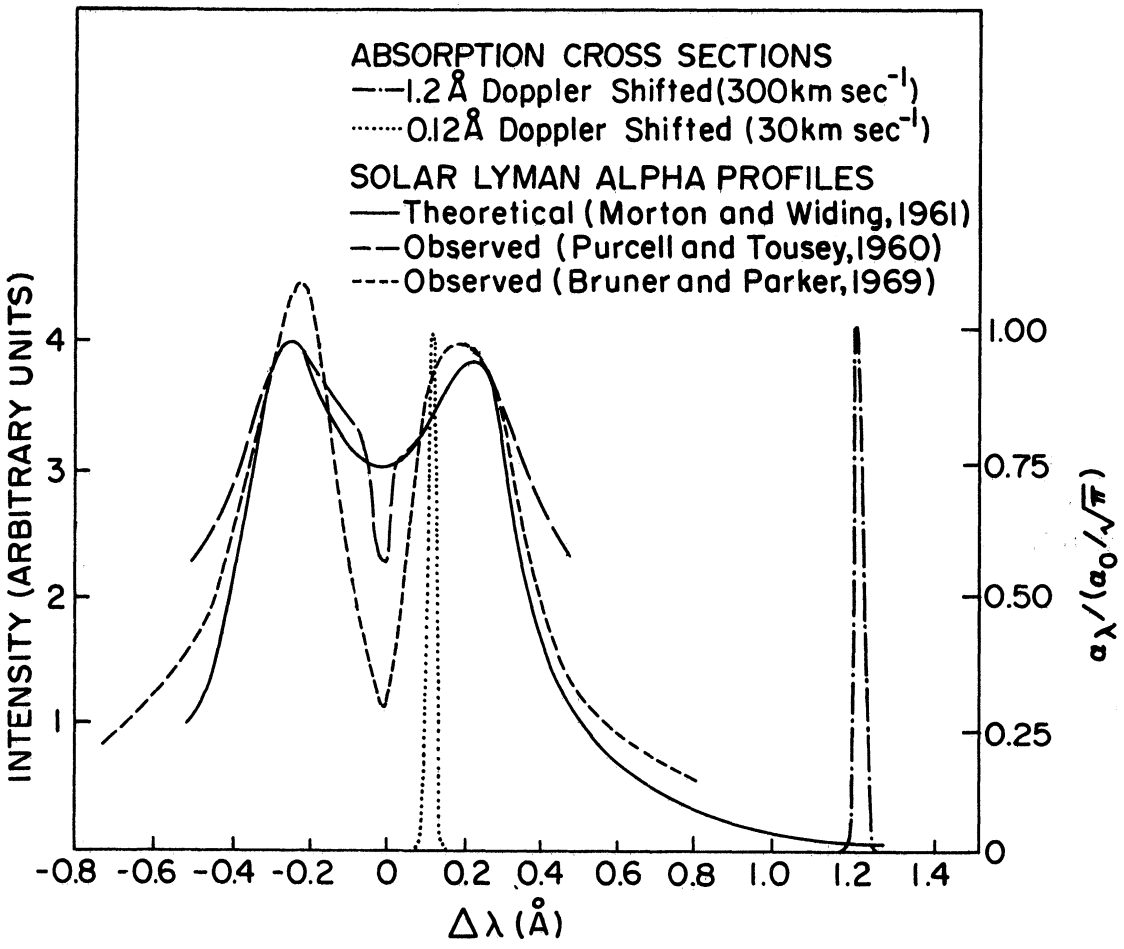

Fig. 2. Normalized absorption cross section (right ordinate) and Solar Lyman Alpha profiles (left ordinate) vs. $\Delta\lambda$. In this figure, $\alpha_\lambda = \frac{\alpha_o}{\sqrt{\pi}} \cdot \exp\left[-\left(\frac{\lambda-\lambda_o}{\Delta\lambda_D}\right)^2\right]$, where, $\Delta\lambda_D = \sqrt{\frac{2kT}{m_H}} \cdot \frac{\lambda_o}{c}$; and $T \simeq 100^oK$.

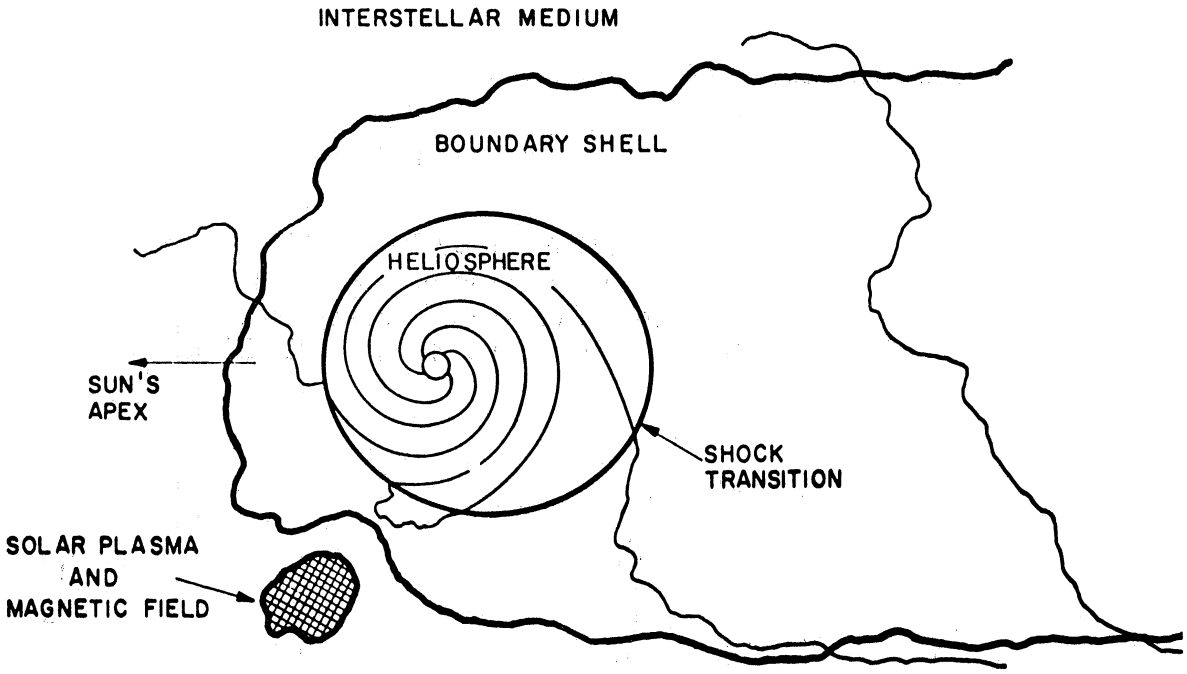

Fig. 3. Illustration of possible interaction configuration between the solar wind and the interstellar medium (Dessler, 1967).

speeds are randomized in direction. The protons in the compressed region beyond the shock (called the boundry shell) resonantly charge exchange with the neutral interstellar hydrogen ($H^+ + H \rightleftharpoons H + H^+$). This charge exchange process provides an isotropic flux of fast neutral hydrogen atoms some of which move through the shock boundary and in the direction of the Sun. On their passage to and in the vicinity of the Sun, the fast hydrogen atoms are lost by solar UV photoionization and charge exchange with the solar wind protons. Patterson et. al. (1963), also included a very minor amount of possible penetration of 'cold' interstellar hydrogen into the heliosphere. Therefore, the interplanetary hydrogen distribution model of Patterson et. al. (1963) consists of the following two distinct components: (i) the 'hot' component, resulting from the above mentioned charge exchange process. The neutral hydrogen atoms of the hot component possess typical solar wind velocities of 300-400 km sec^{-1} and their concentration at 1 AU calculated by Patterson et. al. (1963) is $\sim$ 0.02 cm^{-3}, (ii) the 'cold' or thermal component, which is due to the direct penetration of the interstellar cold hydrogen into the inner solar system. The interstellar gas supposedly has a randomly directed velocity of $\sim$ 10 km sec^{-1}. In the vicinity of the Sun, the loss process of the cold hydrogen is similar to that of fast hydrogen atoms. Patterson et. al. (1963) have calculated concentration of the cold component to be about 0.002 cm^{-3} at 1 AU. The absolute values of hydrogen number density were provided by normalizing the distribution functions with Morton and Purcell's (1962) 15% 'residual' L_α intensity (see Section 2.4). In the model of Patterson et. al. (1963) the shock front is supposedly located at 20 AU and the boundary shell is

assumed thin.

2.5.4 THE THICK BOUNDARY SHELL MODEL

The concentration of the cold hydrogen atoms in the outer parts of the solar system is so low (~ 0.1 H atoms cm^{-3}) that the removal of energy from the solar wind protons beyond the shock proceeds very slowly and therefore, the charge exchange may take place over an extended boundary shell. Hundhausen (1968) investigated this idea of thick boundary shell in detail and found that most of the charge exchange of solar wind protons with the interstellar hydrogen does not occur in a thin region immediately beyond the shock front, but in a long extended boundary shell. If the shock boundary is still assumed to be located at 20 AU (Patterson et. al., 1963), the mean free path for charge exchange of interstellar hydrogen with solar wind protons is quite large (the value, however, is a lot smaller than the value of 100 AU given by Hundhausen (1968); the details are given in Appendix B. 2). Hundhausen (1968) argued, on the basis of large mean free path for charge exchange, that the thin shell model of Patterson et. al. (1963) is invalid and a rather thick boundary region must be invoked. In Hundhausen's (1968) calculations, it was demonstrated that the shock boundary must be moved much closer to the Sun (where the mean free path for charge exchange is much smaller) in order to maintain the values of the hot and cold component densities derived by Patterson et. al. (1963). Hundhausen's (1968) calculations indicate a shock front at 5 AU and a considerably larger radius for the boundary shell. For the shock front to be at 5 AU, an interstellar magnetic field of 10^{-4} gauss (nearly a factor of 10 larger than the conventionally accepted

value of 10^{-5} gauss, Axford et. al., 1963) is required.

2.5.5 DEPARTURE FROM THE THIN AND THICK SHELL MODELS

There are two major difficulties with both the thin shell model of Patterson et. al. (1963) and the thick boundary shell model of Hundhausen (1968): (i) it was assumed that Morton and Purcell's (1962) 15% 'residual' L_α emission resulted from the scattering of solar L_α on the interplanetary 'hot' hydrogen. As explained earlier in Sec. 2.5.1, one cannot assume that the 'line center flux' of L_α is responsible for such excitation. Therefore, the hot hydrogen densities derived by Patterson et. al. (1963) and Hundhausen (1968) are incorrect, (ii) more importantly, motion of the solar system relative to the interstellar medium was ignored in both these models. Such a relative motion will tend to destroy the spherical symmetry in the heliosphere and the boundary region and consequently, the interplanetary hydrogen distribution must be modified. The solar system has a peculiar velocity of 20 km sec^{-1} relative to the interstellar medium, in the direction of RA = 270° and $\delta = +30^\circ$, called the solar apex (Allen, 1964). The frame of reference (called the local standard of rest) is assumed fixed to the average motion of nearby stars. The interstellar medium itself might possess a 10 km sec^{-1} component of velocity randomized in direction.

The following models of Blum and Fahr and Thomas take into account the solar system apex motion.

2.5.6 THE BLUM-FAHR ANISOTROPIC MODEL

Axford et al. (1963) gave a brief discussion of the asymmetry resulting from solar system relative motion. Dessler (1967) showed that the solar wind plasma stored in the interstellar

medium beyond the shock front does not attenuate the flow of interstellar neutral hydrogen into the inner solar system. For a shock front located at $\sim$ 50 AU (value obtained by Axford et. al. (1963) for an interstellar magnetic field of 10^{-5} gauss) the mean free path for charge exchange of the cold interstellar hydrogen with stored solar wind plasma is of the order of 210 AU (see calculations in Appendix B). This large value of mean free path assures almost free passage of the cold interstellar hydrogen into the heliosphere (Tinsley, 1971).

Blum and Fahr (1969, 1970a, 1970b), Fahr (1970, 1971a) and Blum (1972) have investigated in depth the asymmetric model of interplanetary hydrogen distribution. Their model will henceforth be referred to simply as the Blum-Fahr model. The Blum-Fahr model takes into account the 20 km sec^{-1} velocity of the solar system (relative to the local standard of rest), but neglects any random motion of the interstellar gas. It assumes that the boundary shell is thin to the passage of the cold interstellar hydrogen into the heliosphere and considers the effects of gravitational focusing in the vicinity of the Sun. According to this model, at a certain distance r from the Sun, the distribution of interplanetary hydrogen is composed of three components: (i) the 'cold' component, which is a direct result of the penetration of the cold interstellar hydrogen into the heliosphere, at a velocity of 20 km sec^{-1} relative to the Sun and from the direction of the solar apex. According to the Blum-Fahr model, the cold interstellar hydrogen enters the solar system along Keppler hyperbolae. The density of the cold component at 1 AU is calculated to be $\sim 0.3 n_o$, where n_o is the density of the interstellar hydrogen at infinity i.e., the density of the medium in which the heliosphere is immersed.

(ii) the 'hot' component, arising out of resonance charge exchange of the penetrating cold interstellar hydrogen on its way to and in the vicinity of the Sun. As a result of charge exchange, fast hydrogen atoms moving at typical solar wind speeds of 300-400 km sec^{-1} are obtained. Blum and Fahr (1970) estimate the density of the hot component to be nearly one to two orders of magnitude smaller than the cold component density at and about 1 AU, (iii) the 'hot interstellar' hydrogen, which is emitted isotropically from the boundary region in the general direction of the sun. This flux of the fast hydrogen atoms is the result of the charge exchange of the interstellar hydrogen with the turbulent solar wind plasma stored in the extended boundary region beyond the magnetic shock front and in the interstellar medium. Blum and Fahr (1970) note that the contribution and influence of this component on the density of interplanetary hydrogen is negligibly small.

The absolute value for the density of interstellar hydrogen at infinity, n_o in the Blum-Fahr model was provided by the L_α intensity measured by the photometers on board Vela 4 satellite. This calculation is outlined in Appendix B. A value of 0.06 H atoms. cm^{-3} was obtained for n_o. The same value of n_o should be obtained on the basis of the OGO V December 1969 L_α measurements even though Bertaux and Blamont (1970) argue that the value of n_o is as much as a factor of 10 smaller than given by the Blum-Fahr model (see Appendix B for details).

If the Blum-Fahr model is correct, an anisotropic distribution of the cold interplanetary hydrogen may be expected with a maximum density in the solar apex direction and a minimum in the

opposite direction. Based on the OGO V (December, 1969) and the Vela 4 (June, 1967) L_α observations one might expect the density of the interstellar hydrogen medium around the solar system to be nearly 0.06 H atoms·cm^{-3}. The cold interplanetary hydrogen is expected to be streaming at a velocity of nearly 20 km sec^{-1} from the direction of the maximum measured L_α intensity. Its distribution according to Fahr (1970) is shown in Fig. B-1 (Appendix B), and it has an exponential form: $n(r) = n_o \exp(-r_c/r)$; where r_c is the radius of the cavity and r is the distance from the Sun. The validity of the exponential form is discussed in Appendix B.

2.5.7 DEPARTURE FROM THE BLUM-FAHR MODEL, THE THOMAS MODEL

Modifications in the Blum-Fahr model of interplanetary hydrogen distribution were warranted by some puzzling features of the recently compiled complete sky maps of L_α (Thomas, 1971; Bertaux and Blamont, 1971; Bertaux et. al., 1972). These maps revealed the maximum interplanetary L_α intensity in the direction of RA = 263° and δ = - 22°, which is different from the solar apex direction predicted by Blum-Fahr model. Thomas (1971) concluded that the interstellar gas has its own peculiar speed and direction different from the solar system apex motion. A vectorial addition of these two motions, therefore, yields the velocity and the apparent direction of the interplanetary hydrogen gas (Thomas, 1971).

Thomas (1971) constructed a model of interplanetary hydrogen distribution which is basically similar in nature to the Blum-Fahr model except that it takes into consideration the following two major effects neglected by the Blum-Fahr model, namely: (i) the

effect of the solar L_α radiation pressure: the Blum-Fahr model predicts that the penetrating interstellar hydrogen approaches the Sun most closely in the direction of the solar apex. A gravitational focusing of the interplanetary hydrogen atoms in the vicinity of the Sun was assumed. As shown in Appendix B, the solar gravitational force is almost equally balanced by solar L_α radiation pressure at the solar maximum so that a pure gravitational focusing or deflection predicted by the Blum-Fahr model may be non-existent. Thus, no cusp like features in the downwind direction (i.e., opposite the direction of approach of the interstellar gas) may be present. Around the solar minimum, however, the solar gravitational focusing becomes quite significant. Thomas' (1971) 'cold' model takes into account the effect of the solar L_α radiation pressure, (ii) Thomas' 'hot' model considers the possible random velocity of the interstellar gas neglected by the Blum-Fahr model. Thus, according to the Thomas cold model, the interplanetary atoms are expected to stream past the Sun in nearly straight line trajectories; there is no solar gravitational focusing near the solar maximum. Since the random motion of the interstellar gas was disregarded, the cold model depends only on the density, temperature and the velocity of the streaming hydrogen. According to this model, all the hydrogen in the downwind direction is ionized; therefore, in order to account for nearly 200-240 R L_α intensity seen in this direction by OGO V (see Sec. 2.4) an isotropic galactic emission source is invoked. The cold model, therefore, assumes that superimposed on the interplanetary L_α is an isotropic galactic L_α emission of nearly 200-240 R.

The hot model, on the other hand, eliminates entirely the need of any isotropic galactic emission to explain the 200-240 R of L_α recorded in the downwind direction. The hot model takes into consideration a possible random component of velocity of the interstellar gas superimposed on the monodirectional streaming velocity. The gas temperature is assumed high ($\sim 10^4$ ^oK) to ensure filling in the downwind cavity with neutral hydrogen. The temperature, velocity and density of the hot component are adjusted to produce the observed L_α emission both in the direction of approach, as well as in the downwind direction since there is no isotropic galactic emission in this model.

The values of density, temperature and velocity derived by Thomas (1971) are presented in Table 1. A comparison of the values with the results of Bertaux and Blamont (1971) and Bertaux et. al. (1972) is also shown in Table 1. The Bertaux et. al. (1972) results differ somewhat from Thomas (1971) since Bertaux et. al. (1972) have assumed a Maxwellian velocity distribution both for the cold and hot components in contrast to Thomas' (1971) single velocity distribution. It is apparent from Table 1, that an unambiguous determination of density (n_o), temperature(T), and velocity (V_{IP}) is not possible. For example, an increase in the temperature and a decrease in the velocity yield almost the same value of the interplanetary hydrogen density at infinity. Fig. 4 adapted from Thomas (1971)shows the distribution of the interplanetary cold and hot hydrogen atoms as a function of the distance from the Sun.

As discussed in Sec. 2.2, an isotropic distribution of the diffuse galactic L_α is not unlikely; therefore, the Thomas (1971)

TABLE 1

Velocity, Temperature and Density of the Interplanetary Hydrogen Gas

Deduced Quantity	COLD Model			HOT Model		
	Thomas (1971)	Bertaux and Blamont(1971)	Bertaux et. al. (1972)	Thomas (1971)	Bertaux and Blamont(1972)	Bertaux et. al. (1972)
V_{IP}(km. sec^{-1})	9.1	11.6	7 ± 2.0	5.3	6.9	3 ± 1.0
T(^{o}K)	0	0	$(7 \pm 3) \times 10^{3}$	3.5×10^{3}	5.8×10^{3}	$(1.2 \pm 0.3) \times 10^{4}$
n_o(cm^{-3}) (H-density at infinity)	0.06	0.03	0.08	0.12	0.09	0.12

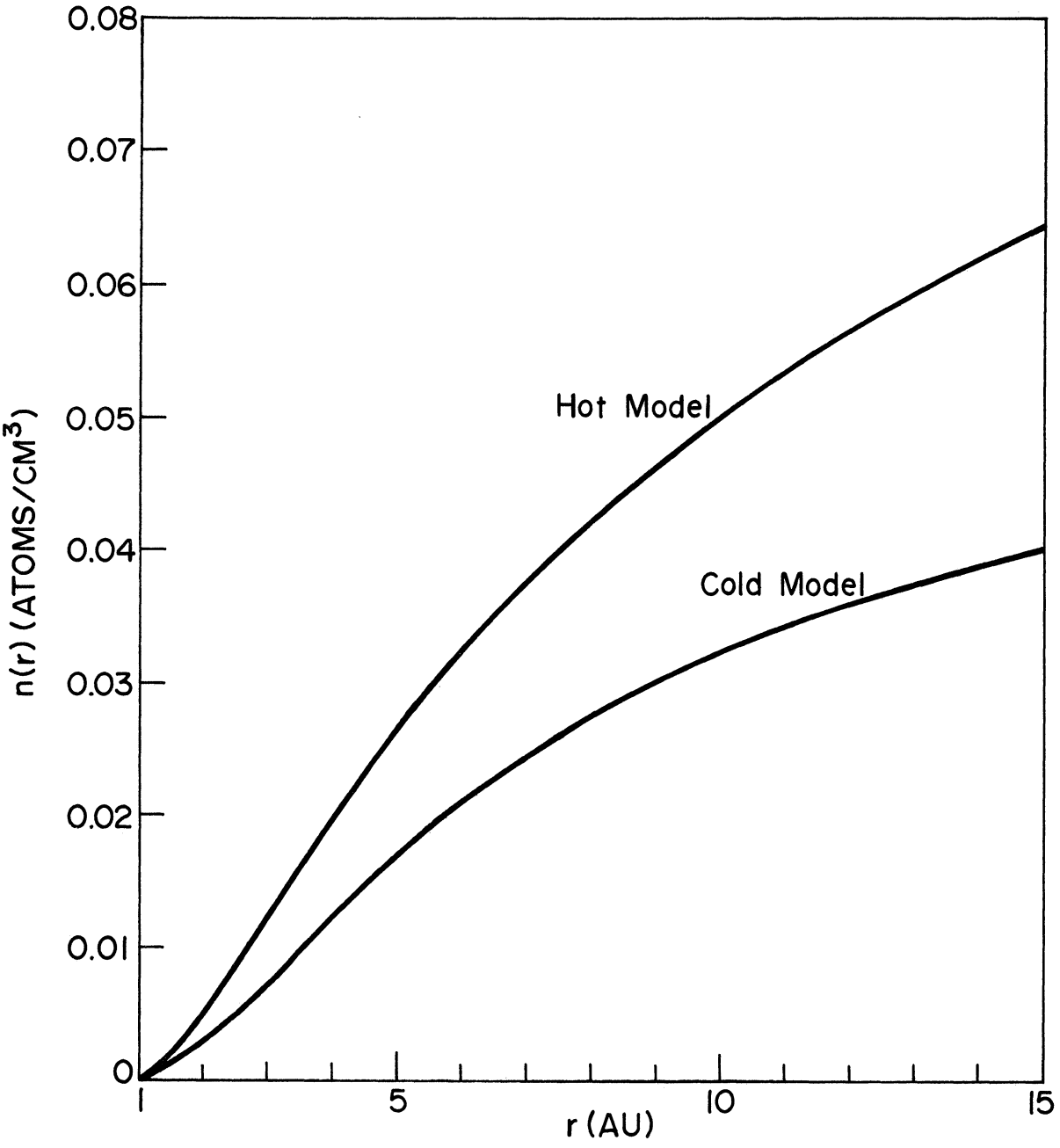

Fig. 4. Interplanetary 'cold' and 'hot' hydrogen density distribution as a function of the distance from the sun (Thomas, 1971).

'cold' model was adopted for the calculations of interplanetary H_α intensity and Doppler profiles given in the following two sections.

2.6 INTERPLANETARY HYDROGEN--EVALUATION OF BALMER LINE INTENSITIES

2.6.1 INTRODUCTION

A general formulation leading to the fluorescence emission rates of the interplanetary hydrogen emissions will be given first in this section. In particular, H_α and H_β intensities will be estimated using the interplanetary gas parameters arrived at in the previous section. The Doppler profiles of the interplanetary Balmer lines will be evaluated theoretically in Sec. 2.7.

2.6.2 FLUORESCENCE EMISSION OF THE INTERPLANETARY HYDROGEN LINES

The population of the various levels excited by the scattering of the solar UV on the ground state hydrogen atoms will be calculated. The technique is based on first calculating the population of a certain highest state due to the direct solar excitation and then determining the population of all subsequent lower states by a cascade method. The scheme is general and is applicable to interplanetary neutral hydrogen atoms irrespective of the origin of such atoms.

In Fig. 5, transitions contributing to the population of n=3 state of atomic hydrogen are shown. Transition from n=3 to n=2 gives rise to H_α emission. The n=3 state is populated directly by the excitation of atomic hydrogen in the ground state by the solar L_β. Subsequent members of the Lyman series (i.e., L_γ, L_δ, etc.) populate it indirectly (see Fig. 5). Similarly n=4 state is populated directly by the L_γ excitation of the ground state, with indirect

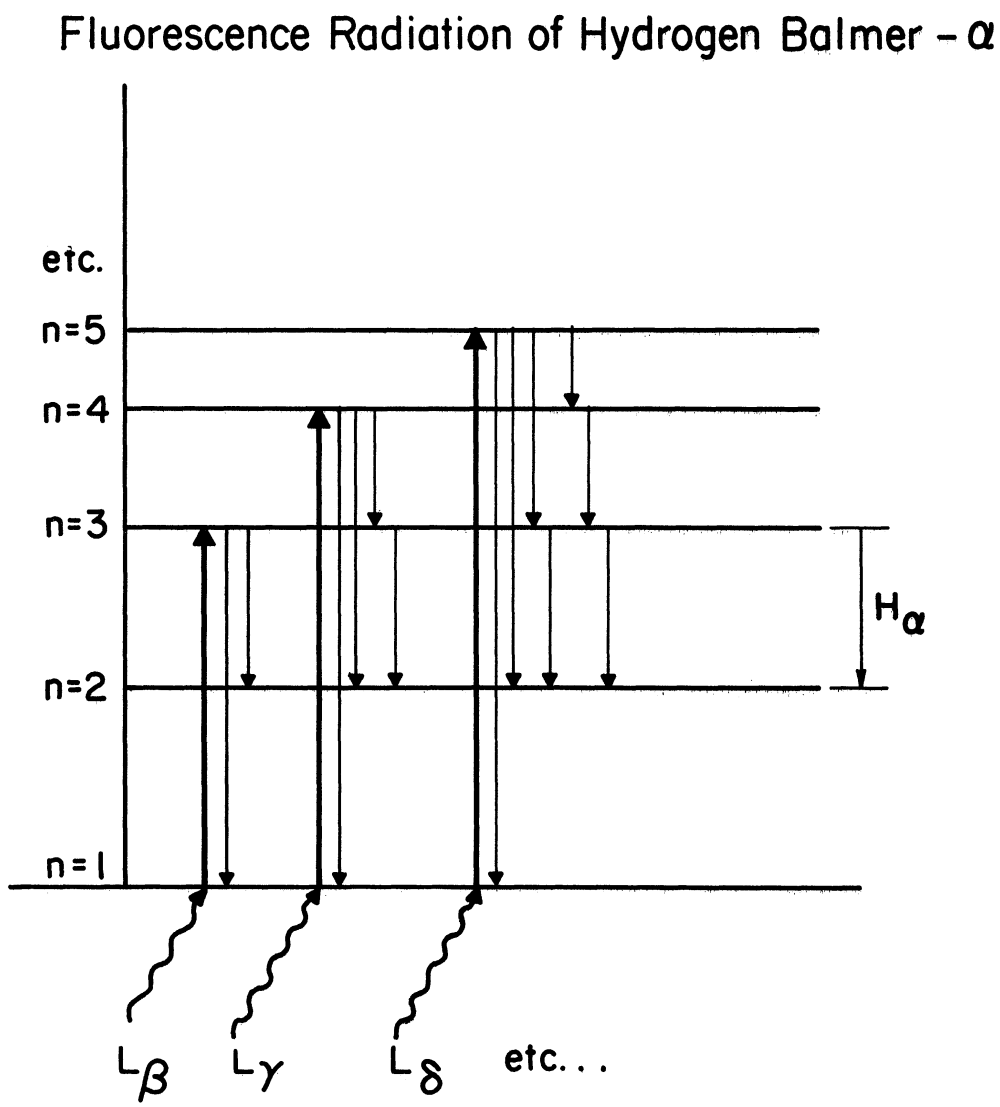

Fig. 5. Emission of an H_α photon by fluorescence scattering of the ground state hydrogen atom by solar UV.

contributions from L_δ , L_ϵ etc. The H_β line corresponds to the transition from n=4 to n=2 state.

The fluorescence scattering calculations are truncated at level n=8 because no significant contribution to the population of the lower levels is made from beyond this truncation level. The solar EUV fluxes given by Hall and Hinteregger (1970) are used in the present calculations (see Table 2).

The 'direct' production rate P_n (direct) of the n^{th} level excited directly by the scattering of solar UV (of frequency ν) on the ground state hydrogen atom is

$$P_n(\text{direct}) = (\pi \mathcal{F}_\nu) \cdot \alpha_\nu \cdot n(H|1) \qquad (2\text{-}1)$$

where $\pi \mathcal{F}_\nu$ = Solar UV flux of frequency ν in photons$\cdot$ cm^{-2} sec^{-1}

α_ν = Absorption cross section ($\alpha_\nu = \frac{\pi e^2}{mc} f_{ij}$; see Appendix B. 1 for the definitions of the various symbols)

$n(H|1)$ = Number density of the interplanetary hydrogen atoms in the ground state.

On equating the production rate to the loss rate of a given excited level, one obtains the following general expression for the population of the n^{th} excited state

$$N_n = \frac{P_n(\text{direct}) + \sum_{n''=n+1}^{\infty} A_{n''n} \cdot N_{n''}}{\sum_{n'=1}^{n-1} A_{nn'}} \qquad (2\text{-}2)$$

where $A_{nn'}$ = Probability of transition from state n to n'. Stimulated emissions and absorptions to higher levels were found negligible and were therefore not considered in deriving the above expression for N_n.

The higher limit (infinity) of the summation term in the numerator of Equation (2-2) represents the cut off state from beyond which no significant contributions to the population of lower states are made. This cut off, as explained earlier, in assumed to be n=8 for

TABLE 2

Solar EUV Fluxes for Atomic Hydrogen Lyman Series and the Associated Oscillator Strengths

Wavelength Å	Lyman Identification	Corresponding Transition from n=1 to	Flux at 1AU Photons cm^{-2} sec^{-1}	Oscillator Strength, f_{ij}
1215.7	L_α	2	3.0(11)*	4.162(-1)*
1025.7	L_β	3	3.5(9)	7.910(-2)
972.5	L_γ	4	0.8(9)	2.899(-2)
949.7	L_δ	5	0.39(9)	1.394(-2)
937.8	L_ϵ	6	0.22(9)	7.799(-3)
930.7	L_ξ	7	0.13(9)	4.814(-3)
926.2	L_η	8	0.13(9)	3.183(-3)

* a(n) = a x 10^n, so that

3.0(11) = 3.0 x 10^{11}, and 4.162(-1) = 4.162 x 10^{-1}, for example.

the present analysis. The appropriate Einstein transition probabilities, A_{jk} are listed in Table 3.

The results of computations for the population of hydrogen atoms in excited levels are presented in Table 4. It should be noted in Table 4 that practically no contribution to the population of level 2 arises from higher levels (relative contribution to level 2 from higher levels is $\sim 10^{-6}$). Therefore, L_α emission is basically a pure resonance phenomenon. The n=3 state gets nearly 3% contribution from the higher excited levels. Therefore, for the purpose of estimating the emission rates of the H_α line, one can ignore the small contribution from the levels higher than three. The importance of the higher levels in determining the populations of a certain state becomes fairly significant for levels beyond three. Nearly 10%of contributions to the population of levels 4, 5, 6, and 7 arise from the higher levels. In the preceding general formulation of the fluorescence scattering, 'average' values of the appropriate Einstein transition probabilities (Table 3) were used. However, in the case of the interplanetary H_α and H_β emissions, for example, only one of the seven allowed fine structure components is possible (see Appendix A), therefore, the use of average transition probabilities from principal quantum number n to n' is incorrect. For calculating the fluorescence emission rates of interplanetary Balmer lines, only transition probabilities particular to the 'appropriate fine structure transitions' (see Appendix A) can be used. Donahue (1964) and others referencing Donahue (1964) have made use of the correct transition probabilities in their L_β and H_α radiative transfer calculations, others have not. The values of the transition probabilities and oscillator strengths for the pertinent transitions are presented in Table 5.

TABLE 3

Atomic Hydrogen - Average Transition Probabilities

A_{jl} (sec^{-1})	j = 8	7	6	5	4	3	2
$A_{j,7}$	2.27(5)*						
$A_{j,6}$	1.56(5)	4.56(5)					
$A_{j,5}$	1.38(5)	3.25(5)	1.02(6)				
$A_{j,4}$	1.42(5)	3.04(5)	7.71(5)	2.69(6)			
$A_{j,3}$	1.65(5)	3.35(5)	7.78(5)	2.20(6)	8.98(6)		
$A_{j,2}$	2.21(5)	4.38(5)	9.73(5)	2.53(6)	8.41(6)	4.41(7)	
$A_{j,1}$	3.86(5)	7.56(5)	1.64(6)	4.12(6)	1.27(7)	5.57(7)	4.69(8)
$\sum_{\ell=1}^{j-1} A_{j\ell}$	1.43(6)	2.61(6)	5.19(6)	1.15(7)	3.01(7)	9.98(7)	4.69(8)

*a(n) = a x 10^n, so that

2.27(5) = 2.27 x 10^5, for example

TABLE 4

Results of Atomic Hydrogen Fluorescence Scattering Calculations

n	$T_1 = P_n(\text{direct})^*$	$T_2 = \sum_{n''=n+1}^{\infty} A_{n''\,n} N_{n''}$ *	$R = (T_2/T_1) \times 100$	N_n*
2	1.628×10^{-3}	0.000	0.0	3.464×10^{-12}
3	2.569×10^{-6}	0.074×10^{-6}	2.9	2.641×10^{-14}
4	1.937×10^{-7}	0.141×10^{-7}	7.2	6.888×10^{-15}
5	4.331×10^{-8}	0.384×10^{-8}	8.8	4.080×10^{-15}
6	1.333×10^{-8}	0.126×10^{-8}	9.5	2.810×10^{-15}
7	4.788×10^{-9}	0.495×10^{-9}	10.3	2.018×10^{-15}
8	3.135×10^{-9}	0.000	0.0	2.180×10^{-15}

*Note: T_1, T_2 and N_n are normalized by the ground state interplanetary hydrogen number density, n(H/1), at 1 AU.

TABLE 5

Atomic Hydrogen - Transition Probabilities and Oscillator for a Few Select Fine Structure Transitions

Transition	Transition Probability (sec^{-1})	Oscillator Strength
1s - 2p	6.265×10^{8}	0.4162
1s - 3p	1.672×10^{8}	7.910×10^{-2}
1s - 4p	6.818×10^{7}	2.899×10^{-2}
2s - 3p	2.245×10^{7}	0.4349
2s - 4p	9.668×10^{6}	0.1028
3s - 4p	3.065×10^{6}	0.4847

The population of the 3p excited state, N_{3p}, is then given by the following expression

$$N_{3p} = \frac{P_3(\text{direct})}{A_{3p\,-\,1s} + A_{3p-2s}} \qquad (2-3)$$

The direct production rate of a certain state has the same value as given in Table 4. The populations of the 2p, 3p and 4p states at 1 AU, normalized by n(H/1) at 1 AU are calculated to be

$$\begin{aligned} N_{2p} &\simeq 2.6 \times 10^{-12} \\ N_{3p} &\simeq 1.4 \times 10^{-14} \\ N_{4p} &\simeq 2.4 \times 10^{-15} \end{aligned} \qquad (2-4)$$

The corresponding volume emission rates ($N_j \cdot A_{jk}$) of L_α, H_α and H_β lines normalized by n(H/1) at 1 AU are:

$$\begin{aligned} \eta_{L_\alpha} &\simeq 1.6 \times 10^{-3} \text{ photons} \cdot \text{sec}^{-1} \\ \eta_{H_\alpha} &\simeq 3.0 \times 10^{-7} \text{ photons} \cdot \text{sec}^{-1} \\ \eta_{H_\beta} &\simeq 2.3 \times 10^{-8} \text{ photons} \cdot \text{sec}^{-1} \end{aligned} \qquad (2\text{-}5)$$

η_λ's given in Equation (2-5) for the appropriate fine structure transitions are generally smaller than the value one would obtain using 'average' transition probabilities. η_{H_α} of Equation (2-5), for example, is a factor of four smaller than η_{H_α} calculated on the basis of 'average' values of transition probabilities (i. e. taking A_{jk} from Table 3 and N_n from Table 4).

The integrated intensity $\mathcal{I}_\lambda(R)$ in Rayleighs is given by

$$\mathcal{I}_\lambda(R) = 10^{-6} \int_{R_e}^{\infty} \eta_\lambda(r)\, dr \qquad (2\text{-}6)$$

where, R_e= 1 AU

Therefore, the interplanetary H_α and H_β intensities are in the following ratio to the L_α intensity

$$\frac{\mathcal{I}_{H_\alpha}(R)}{\mathcal{I}_{L_\alpha}(R)} = \frac{\eta_{H_\alpha}}{\eta_{L_\alpha}} \simeq 1.9 \times 10^{-4} \qquad (2\text{-}7)$$

and $$\frac{J_{H_\beta}(R)}{J_{L_\alpha}(R)} = \frac{\eta_{H_\beta}}{\eta_{L_\alpha}} \simeq 1.4 \times 10^{-5} \qquad (2\text{-}8)$$

The above scaling factors are uncertain by about a factor of two because of the lack of precise knowledge of the intensity and shape of the solar EUV fluxes. The density of the interstellar hydrogen gas at infinity does not appear in the ratio.

2.6.3 EXPECTED INTERPLANETARY H_α AND H_β INTENSITIES

(1) The Cold Model Estimate:

According to the cold model of Thomas (1971), all of the 215 R of L_α in the downwind region may be due to the isotropic galactic source. The maximum L_α intensity of 530 R recorded by OGO V in the opposite direction should, therefore, consist of 315 R of interplanetary L_α superimposed on 215 R of isotropic galactic L_α. Therefore, with the scaling factors just computed for estimating H_α and H_β intensities from the measured L_α intensity, one obtains the following estimates on the interplanetary H_α and H_β intensities:

(i) a maximum 0.06 R of interplanetary H_α and 0.004 R of H_β from the direction of the OGO V L_α maximum (RA = 263±5°, δ = -17±5°); and

(ii) no interplanetary H_α and H_β emission in the opposite direction.

The abovementioned interplanetary H_α and H_β emissions are expected to be superimposed on an extremely feeble and diffuse isotropic emission of galactic origin.

(2) The Hot Model Estimate:

Thomas' (1971) hot model of interplanetary hydrogen distribution attributes the total 530 R of L_α measured in the direction of L_α maximum and 215 R of L_α in the opposite direction solely to the

fluorescence scattering of solar L_α on the interplanetary hydrogen. No isotropic galactic source to explain the downwind region L_α intensity is invoked in this model. With appropriate scaling factors from L_α intensity, one obtains the following estimates on the interplanetary H_α and H_β intensities according to the hot model: (i) a maximum of 0.1 R of interplanetary H_α and 0.007 R of H_β centered around the direction of the OGO V L_α maximum; (ii) the maximum varies smoothly to a minimum of 0.04 R of interplanetary H_α and 0.003 R of H_β in the opposite direction. The associated Doppler temperatures are expected to approach 10^4°K according to this model.

Therefore, even if the hot model were valid, no more than 0.1 R of H_α from the interplanetary atomic hydrogen source is expected. On the basis of the calculations just presented, it is also evident that Reay and Ring's (1969) observations of 0.1 to 0.2 R of H_β are not compatible with an interplanetary explanation. The source of their observed H_β emission is suspected to be more likely galactic or geocoronal.

2.7 INTERPLANETARY HYDROGEN--CALCULATIONS OF THE DOPPLER PROFILES OF BALMER EMISSION LINES

2.7.1 INTRODUCTION

A general formulation leading to the Doppler profiles of the interplanetary hydrogen Balmer emission lines will be presented in this section. The intensity of emission per unit wavelength ($d\mathcal{J}/d\lambda$ in Rayleighs per Angstrom) as a function of the wavelength shift will be evaluated for both the interplanetary H_α and H_β lines.

2.7.2 GENERAL FORMULATION

A simplified geometry of illumination of the interplanetary hydrogen is shown in Fig. 6. $\vec{R}_s$ and $\vec{r}$ are radii vectors of a point I in the interplanetary medium from the Sun and the Earth respectively, R_e is the mean distance between the Sun and the Earth (R_e = 1 AU), $\vec{V}_o$ is the velocity vector of the interplanetary hydrogen atoms; and V_r is the line of sight component of V_o ($V_r = V_o \cos\theta$). The angles ϕ and θ in Fig. 6 are the angles between $\vec{R}_e$ and $\vec{r}$ and between $\vec{R}_s$ and $\vec{r}$ respectively.

The change in intensity $d\mathcal{I}$ (in Rayleighs) within an interval of distance dr about I is given by

$$d\mathcal{I}(R_s) = \eta(R_s)\, dr \times 10^{-6} \qquad (2\text{-}9)$$

where, $\eta(R_s)$ is the volume emission rate at R_s in units of photons $\cdot$ $cm^{-3} \cdot sec^{-1}$.

Equation (2-9) can be transformed to the following form, giving $d\mathcal{I}/d\lambda$ in units of Rayleighs per Angstrom (see Appendix B. 4. 1 for the derivation of the following form of $d\mathcal{I}/d\lambda$)

$$\frac{d\mathcal{I}}{d\lambda} = \left(\eta(R_s) \cdot R_s^3\right) \cdot \left(\frac{c}{\lambda_o V_o} \cdot \frac{1}{R_e^2} \times 10^{-6}\right) \cdot \frac{1}{\sin^2\phi} \times \left(1.5 \times 10^{13}\right) \qquad (2\text{-}10)$$

Where R_s and R_e are expressed in AU, λ_o in $\mathring{A}$, c and V_o in $cm \cdot sec^{-1}$ and $\eta(R_s)$ in photons$\cdot cm^{-3} \cdot sec^{-1}$. The mulitplication factor 1. 5 x 10^{13}(cm) on the right hand side of Expression (2-10) is equal to 1 AU.

2.7.3 GRAPHICAL REPRESENTATION OF $d\mathcal{I}/d\lambda$

Expression (2-10) for $d\mathcal{I}/d\lambda$ can be simplified by expressing $\eta(R_s)$ in terms of the interplanetary hydrogen density and some other constants.

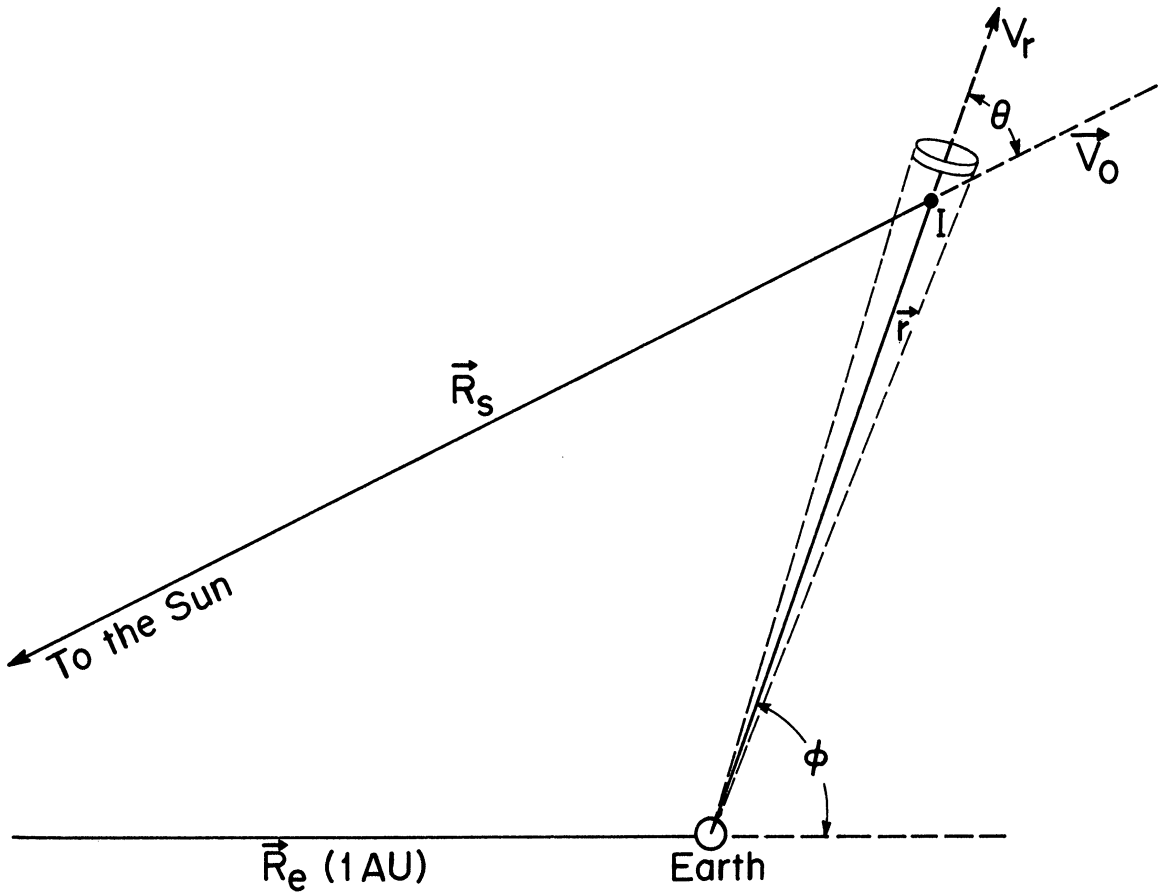

Fig. 6. Interplanetary hydrogen illumination geometry.

From Sec. 2.6.2

$$\eta_\lambda(1AU) = a_\lambda(1AU) \cdot n(H/1) \qquad (2\text{-}11)$$

where

$\eta_\lambda(1AU)$ = Volume emission rate of the interplanetary hydrogen emission line of wavelength λ, at 1 AU

$a_\lambda(1AU)$ = Volume emission rate at 1 AU normalized by n(H/1), its value for H_α and H_β is (Equation (2-5))

$a_{H_\alpha}(1AU) \simeq 3.0 \times 10^{-7}$ photons · sec^{-1}

$a_{H_\beta}(1AU) \simeq 2.3 \times 10^{-8}$ photons · sec^{-1}

(2-12)

a_λ depends upon the solar UV flux, therefore

$$a_\lambda(R_s) = a_\lambda(1AU) \cdot \frac{1}{R_s^2} \qquad (2\text{-}13)$$

The following general distribution for the interplanetary hydrogen density is assumed

$$n(R_s) = n_o \exp(-r_c/R_s) \qquad (2\text{-}14)$$

where n_o is the density of the interstellar hydrogen at infinity and r_c is the characteristic distance from the Sun where the interplanetary hydrogen density falls to $1/e^{th}$ its value at infinity (Fahr, 1970; Thomas, 1971). With the help of Expressions (2-11), (2-13) and (2-14), one obtains

$$\eta_\lambda(R_s) = \frac{\eta_\lambda(1AU)}{R_s^2} \exp(r_c) \cdot \exp(-r_c/R_s) \qquad (2\text{-}15)$$

R_s can be expressed in terms of a non-dimensional parameter x in the following manner (see Equation (B.4-4) in Appendix B.4.1 for details)

$$R_s = \frac{\sin\phi}{\sqrt{1-x^2}} \tag{2-16}$$

where, $x = \dfrac{\lambda-\lambda_o}{(\lambda_o V_o/c)}$ (2-17)

On substituting Expressions (2-15) and (2-16) in Expression (2-10) for $d\mathcal{J}/d\lambda$, one obtains

$$\frac{1}{k'}\frac{d\mathcal{J}}{d\lambda} = \frac{1}{\sin\phi}\,\frac{1}{\sqrt{1-x^2}}\cdot \exp\left(-\frac{r_c\sqrt{1-x^2}}{\sin\phi}\right) \tag{2-18}$$

where

$$k' = \left[\exp(r_c)\cdot\eta_\lambda(1AU)\right]\cdot\left[\frac{c}{\lambda_o V_o}\times 10^{-6}\right] 1.5\times 10^{13} \tag{2-19}$$

Expression (2-18) for $\frac{1}{k'}\cdot\frac{d\mathcal{J}}{d\lambda}$ is general and applicable to any interplanetary hydrogen emission line. In order to find $d\mathcal{J}/d\lambda$ for a given hydrogen line of wavelength λ_o, k' peculiar to that emission line must be calculated. For the interplanetary H_α line (λ_o=6562.8 Å), for example, k'=1.25; assuming the Thomas'(1971) cold model values of the interplanetary gas parameters (n_o=0.06 cm^{-3}, r_c=6.4 AU, and $V_o \simeq 10$ km sec^{-1}).

The maximum wavelength shift $(\lambda - \lambda_o)_{max}$ at λ_o = 6562.8 Å and using $V_o \simeq 10$ km. sec^{-1} is

$$(\lambda-\lambda_o)_{max} = \frac{\lambda_o V_o}{c} = 0.22\ \text{Å} \tag{2-20}$$

The bounds of the wavelength shift in terms of the dimensionless shift parameter x are as follows:

(i) $1 > x > \cos \phi$, for $\phi \leq \pi/2$ (2-21)

(the lower bound on x will henceforth be referred to as the 'cos ϕ - cut off')

(ii) $1 > x > 0$, for $\phi \geq \pi/2$ (2-22)

(see Appendix B.4.2 for a discussion of the bounds on x).

The general behavior of $\frac{1}{k'} \cdot \frac{d\mathcal{J}}{d\lambda}$ for any interplanetary hydrogen emission line as a function of the non-dimensional parameter x (lower scale) for $\phi = 30^{\circ}$, 45°, 60° and 75° is shown in Fig. 7. The upper scale (wavelength shift in Angstrom) is peculiar to the H_{α} emission line. For the case when $\phi \leq \pi/2$; $1 > x > \cos \phi$ (Equation (2-21)), only the segments of the curves to the right of the 'cos ϕ - cut offs'(shown by the arrows in Fig. 7.) are applicable. Note that the curves are drawn for $x < 1$ ($\frac{1}{k'} \frac{d\mathcal{J}}{d\lambda}$ has a singularily at x = 1, see Expression (2-18); L_{β} photons are absorbed as $R_s \rightarrow \infty$). The behavior of $\frac{1}{k'} \frac{d\mathcal{J}}{d\lambda}$ as a function of ϕ for x = 0.9, 0.8, 0.6, and 0.4 is shown in Fig. 8. For the case when $\phi \leq \pi/2$, the segments of the curves to the left of the 'cos ϕ - cut offs'(shown by the arrows in Fig. 8) are applicable.

The interplanetary hydrogen emission Doppler profiles presented in Figs. 7 and 8 are valid for the 'cold' model. For a 10^4 ^{o}K 'hot' hydrogen component, the Doppler half width at the H_{α} wavelength is nearly 0.46 Å and is shifted right out of the maximum allowable H_{α} wavelength shift of 0.11 Å calculated with V_{IP}=5.3 km sec^{-1} (see the Thomas hot model in Table 1). Therefore, the hot model interplanetary hydrogen emission Doppler profiles are broad and their general nature can be derived by convolving the cold model Doppler profiles to a gaussian.

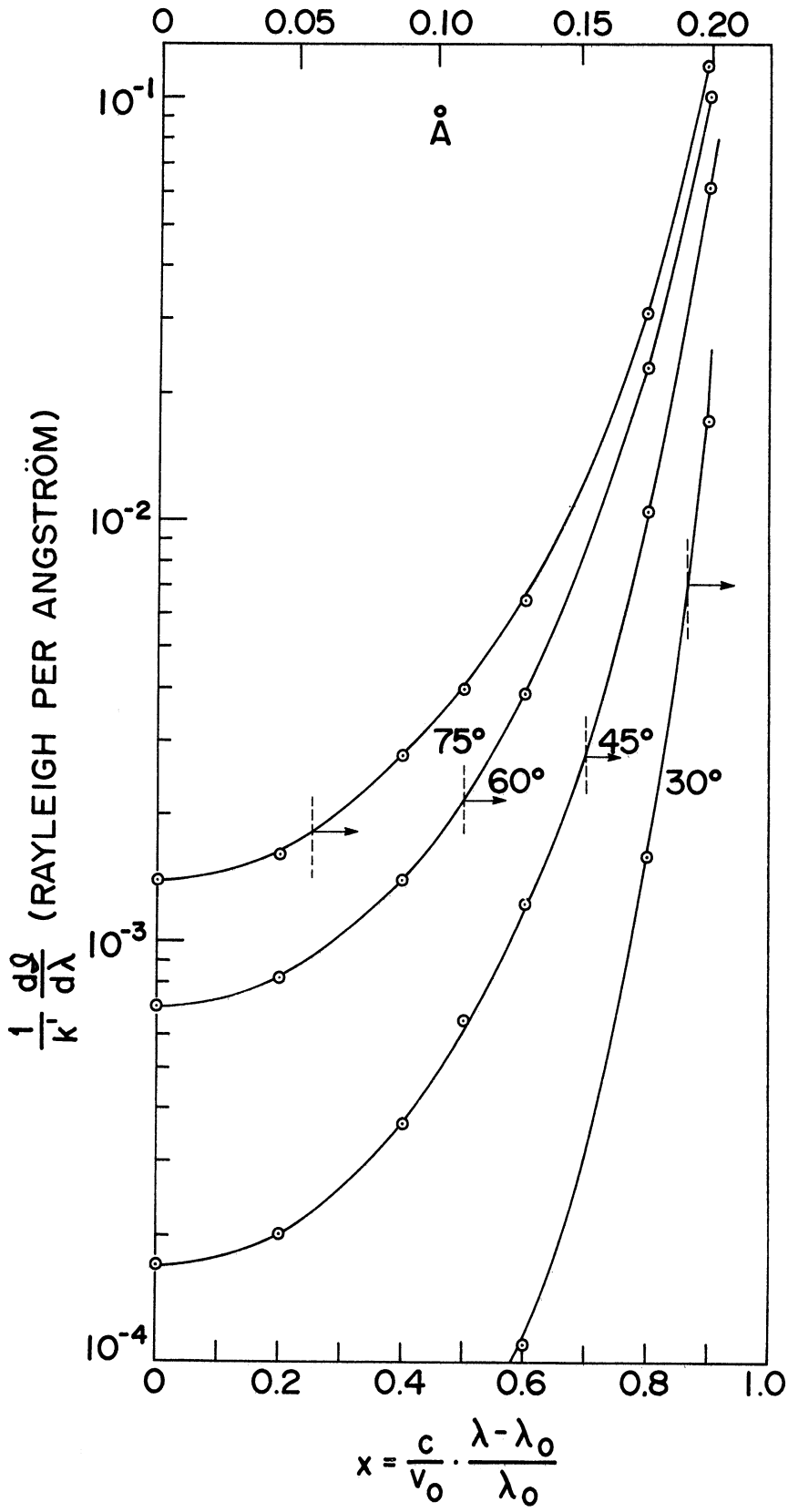

Fig. 7. Interplanetary Balmer emission rate (R. $Å^{-1}$) vs. dimensionless parameter x (lower scale), and vs. wavelength shift at λH_α (upper scale) for several ϕ. The arrows represent the cos - ϕ cutoffs.

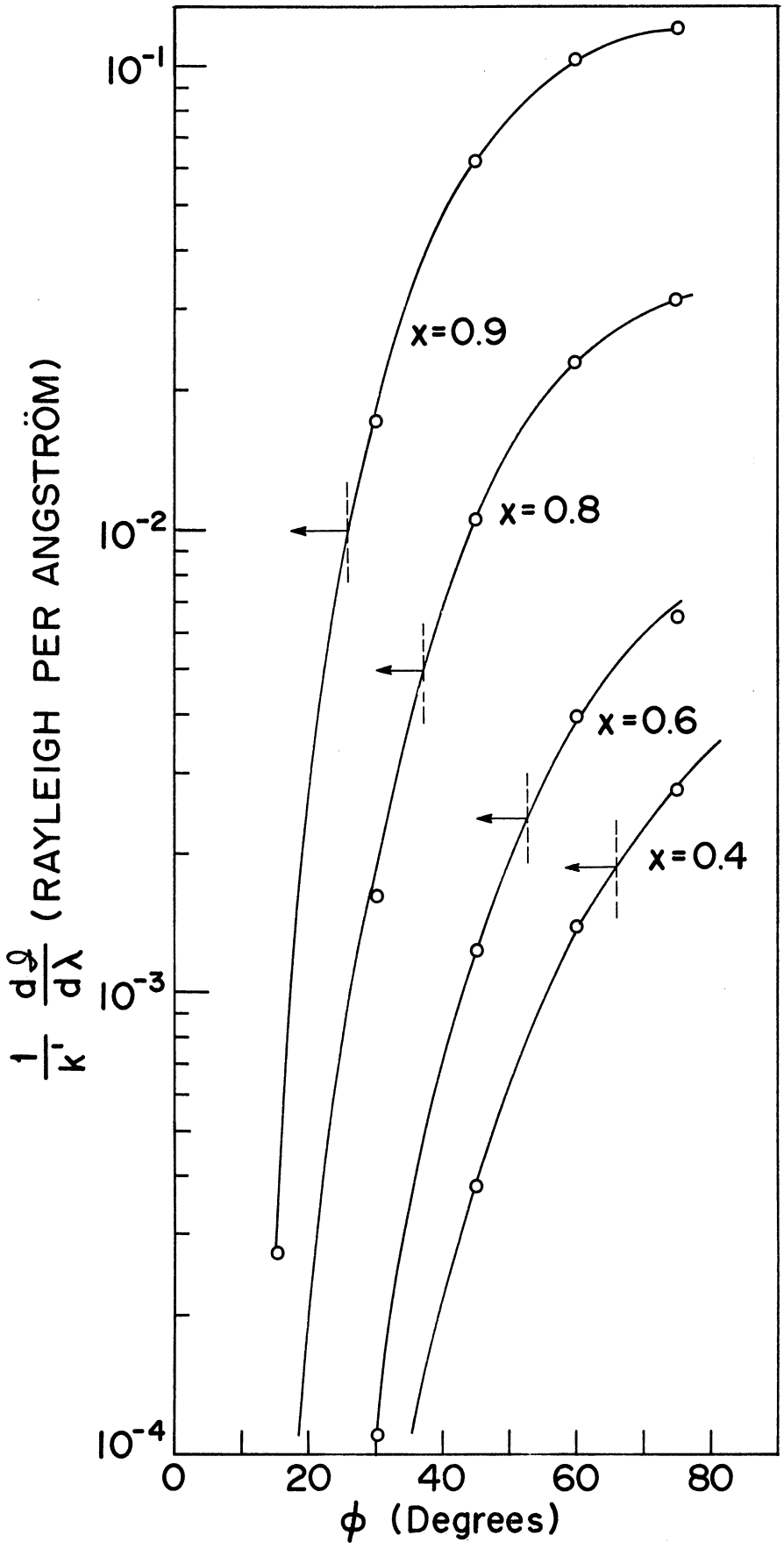

Fig. 8. Interplanetary Balmer emission rate ($R.\,\mathring{A}^{-1}$) vs. ϕ for several x. The arrows represent the cos-ϕ cutoffs.

It should be mentioned here that the Doppler profiles shown in Figs. 7 and 8 represent only the general behavior rather than exact values. This is due to considerable uncertainties in the estimate of the parameters n_o, r_c, V_{IP} and T associated with the interplanetary hydrogen gas (see Table 1).

An analytical expression for the integrated intensity is derived in Appendix B. 4. 3.

The high resolution needed to measure the Doppler profiles of the geocoronal and the interplanetary H_α emisson lines renders the instrument highly insensitive (see Appendix F for the efficiency of the instrument used) , therefore it appears doubtful that it would be possible to measure the Doppler profiles of the weak interplanetary H_α line calculated in this section.

CHAPTER III

GEOCORONAL HYDROGEN BALMER EMISSIONS - REVIEW

3.1 INTRODUCTION

A review of the relevant geocoronal H_α and H_β observations, a brief description of the terrestrial hydrogen distribution, and the pertinent results of the theory of radiation transfer in the geocorona are presented in this chapter.

3.2 CRITICAL REVIEW OF OBSERVATIONS

In 1957, at the Zvenigorod Station of the Institute of Atmospheric Physics, Moscow, a feeble non-auroral H_α radiation was recorded in the night sky spectrum (Krassovsky and Galperin, 1958; Prokudina, 1959; and Shklovsky, 1959). This spectral feature was relatively narrow, its width lay within the instrument width of 2 Å and it was Doppler stationary. Shklovsky (1959) interpreted this emission as being due to the fluòrescence scattering of the solar Lyman Beta (L_β) on the interplanetary neutral hydrogen. He did not totally discard the possibility of the scattering of the solar L_β on the atomic hydrogen of the geocorona, which according to Shklovsky (1959) could be several earth radii in extent. Ground-based observations on the nocturnal H_α radiation were continued during IGY and IQSY in the Soviet Union at Zvenigorod, Abastumani (Fishkova and Markova, 1960; Fishkova, 1962) and Alma Ata (Gaynullina and Karyagina, 1960; Karyagina and Mohzaeva, 1969). Krassovsky (1971) has summarized the data gathered on the H_α radiation between 1957 and 1965 at the above mentioned observatories. All observations up to 1964 were made at zenith angles of 60 and 67°N, zenith angle for 1965 observations was 60°W. The measuring instrument had a maximum resolution of 1 Å and a field of view of 12°. H_α

intensity, averaged over the course of night varied between 2 and 25 R during this period. The Soviet group has interpreted the observed H_α emission to be of the geocoronal origin. It is not obvious whether all of the H_α intensity they have recorded can be interpreted as the geocoronal emission, since extraterrestrial H_α contributions (namely galactic, stellar and interplanetary H_α) to the emission measured with instruments having a rather large field of view and a broad instrument function, are likely.

On numerous occasions in 1962 and 1964, Daehler et al. (1968) while attempting to measure Balmer Beta (H_β) absorption profile in the zodiacal light (at Mt. Chacaltaya Observatory in the Bolivian Andes), using a Fabry-Perot spectrometer of nearly 1.5 $\mathring{A}$ limiting resolution found the absorption feature obscured by an H_β emission of 'uncertain' origin. Further attempts to separate this emission feature were made by Hindle, Reay and Ring (1968) and Reay and Ring (1969) at Testa Grigia Observatory (Italian Alps) in 1967. Measurements were conducted using a Fabry-Perot interferometer with a maximum resolution of 0.4 $\mathring{A}$ and a field of view of 0.5°. The width of the observed H_β spectral feature did not exceed the instrument width and showed a slight Doppler shift. H_β intensities between 0.1 and 0.2R were recorded. They also noted that H_β intensity did drop in the anti-solar direction but was still 'surprisingly high'. They concluded that the origin of this emission was less likely to be geocoronal because of no direct solar excitation in the anti-solar direction. This explanation must, however, be examined somewhat more carefully. Radiation transport of solar L_γ to the anti-solar direction occurs by multiple scattering off the geocoronal hydrogen, therefore, even

though direct solar excitation may not exist in this direction, the detection of the H_β radiation in the anti-solar direction is not all that surprising. However, since Reay and Ring's (1969) observed H_β emission was also Doppler shifted, they concluded that the possible source was more likely to be interplanetary. It has been shown in Sec. 2.6.3 that Reay and Ring's (1969) observed H_β emission rates are not consistent with the theoretical predictions based on the estimates of interplanetary hydrogen density.

Measurements of H_α intensity have also been made by Ingham(1962, 1968) first at Mt. Chacaltaya Observatory and later at Observatoire de Haute Provence. A Czerny Turner type spectrometer having a rectangular field of view of 8^o x 6^o and an instrument width of approximately 3 Å was employed. Observations were made either in zenith or looking in the direction of the North celestial pole. Though H_α emission feature is much narrower than the continuous background (i.e. integrated starlight and zodiacal light both of which have solar type absorption spectrum, and, of course airglow continuum), its 'direct' measurement was prevented because of wide instrument function and an extremely large field of view. Background effects had to be estimated and subtracted from the apparent emission rate at H_α to get actual H_α intensity. Ingham's (1968) interpretation of his data for summer to winter variations in H_α emission rate was invalid since a comparison of H_α intensities was attempted under different sets of azimuth observations (relative to sun's azimuth) and solar depression angles. Photometric measurements of nightsky H_α have also been carried out in Norway (Kvifte, 1959) and in Australia (Armstrong, 1967).

Since 1965, Tinsley has carried out, by far, the most extensive nightsky H_α observation program (Tinsley 1967, 1968, 1969, 1970; Tinsley and Meier 1971, Weller, Meier and Tinsley 1971). Most of his data were collected near Langmuir Laboratory in New Mexico by means of a grille spectrometer (Tinsley, 1966) having a 5.5^o square field of view, and a resolution of nearly 2.5 Å. Tinsley has made several scans to cover H_α intensity variation over the entire range of zenith, azimuth (relative to the sun's azimuth) and solar depression angles. He has also corrected and compiled his data along with that of several others in USSR, Norway, France and Bolivia in order to interpret short term (i. e. diurnal and over a period of days), annual and solar cycle variations of the geocoronal H_α intensity in terms of the viewing directions, solar L_β flux, atomic hydrogen distribution and its column abundance. The corrected data have also been compared with theoretical radiative transfer calculations for geocoronal hydrogen emissions (Tinsley and Meier, 1971).

Tinsley's findings indicate that the diurnal variation of the geocoronal H_α emission is of such a nature that under identical illumination geometry (i. e. essentially the same set of azimuth angle relative to the sun's azimuth, the zenith angle, and the solar depression angles) the morning H_α intensities are larger than evening ones by up to 20%. Furthermore southerly emission rates are greater than northerly ones in the above situation. The diurnal behavior of the observed geocoronal H_α emission can be partially explained by taking into account the possible diurnal variations in atomic hydrogen concentrations and column abundances. The escape loss of hydrogen gas from the terrestrial atmosphere is highly temperature-dependent.

Therefore, at night when the exospheric temperature declines, one might expect a larger hydrogen concentration in the region below the exobase than in the daytime. Patterson (1966) has calculated that hydrogen density maximum occurs between 4 and 6 a. m. local time i. e. nearly two hours after temperature minimum. A diurnal change in atomic hydrogen concentration of nearly a factor of 2 is estimated after including effects of lateral mass flow (McAfee, 1967) and a time dependent density distribution (Patterson, 1970).

Tinsley and others have further noticed sporadic fluctuations in H_α emission rates from night to night; up to 50% change over a period of a fortnight has been observed. A plausible explanation is sporadic changes in the solar L_β line center flux and in exospheric temperature and a subsequent change in geocoronal hydrogen content. Geocoronal H_α also shows a maximum emission rate in the fall and a minimum in the spring. It is difficult to imagine that solar L_β flux behaves in this manner, therefore one is more inclined to invoke such periodicity in the geocoronal hydrogen abundance. One can also expect a solar cycle variation in the H_α emission rates. A ten-fold increase in the geocoronal hydrogen abundance from solar maximum to solar minimum may be expected and the July 21, 1959 and August 22, 1962 measurements of solar Lyman α (L_α) profile by Tousey et. al. (1964) reveal a factor of 3 decrease in the L_α line center flux. Based on this, L_β line center flux may be expected to drop by a factor of 5 from solar maximum to solar minimum. A factor of 2 increase in the H_α emission rate may, therefore,be expected from the solar maximum to the solar minimum (Tinsley, 1968). The geocoronal H_α emission rate is, however, not linearly related to the atomic hydrogen

number density, therefore the abovementioned factor of 2 increase in the H_α intensity from the solar maximum to the solar minimum is only approximately valid. Moreover, quite significant uncertainties in the exact estimate of the H_α emission rate variation over short and long terms arise from the lack of adequate experimental data on the behavior of the solar L_β flux and the atomic hydrogen distribution in the thermosphere and the exosphere.

3.3 REVIEW OF THE TERRESTRIAL HYDROGEN DISTRIBUTION AND THE RESULTS OF THE THEORY OF RADIATIVE TRANSFER IN THE GEOCORONA

3.3.1 INTRODUCTION

It would be helpful to briefly examine the atomic hydrogen distribution in the earth's upper atmosphere first in order to get a better insight into the results obtained from the radiative transfer theory of the geocoronal hydrogen emissions.

3.3.2 ATOMIC HYDROGEN DISTRIBUTION

Atomic hydrogen distribution in the earth's atmosphere can be reasonably divided into regions below 100 km., 100 to 500 km.; and finally beyond 500 km.

(i) The concentration profile in the region below 100 km. is mainly controlled by photochemical processes and by turbulent mixing.

(ii) In the 100-500 km region the distribution of hydrogen atoms is controlled by molecular diffusion. The diffusive equilibrium concentration profiles are obtained on the basis of hydrodynamical equations of motion. The altitude profile of atomic hydrogen in this region is greatly influenced by an upward diffusion of nearly 10^8 H atoms. cm^{-2}. sec^{-1} (Mange 1961).

(iii) At 350 km , the mean free path of atomic hydrogen is of the order of 60 km. and at 500 km, it is about 1000 km. An arbitrary interface (or critical level) called 'exobase' is therefore usually defined at about 500 km to separate the collision-free region above it from the collision dominated atmosphere beneath it. Jeans (1925) and Chamberlain (1963), have attempted to define the characteristics of this transition region between 350 and 500 km. Chamberlain has defined the critical level 'exobase' as the level from which a fraction 1/e of the particles with velocity higher than escape velocity will escape the planetary atmosphere without undergoing any further collisions. Thus hydrogen atoms with sufficiently large kinetic energy have a good probability of leaving the terrestrial atmosphere and eventually escaping into the interplanetary space. Therefore, the velocity distribution of the hydrogen atoms beyond the exobase is no longer Maxwellian. The hydrodynamical concept of the atmosphere is no longer valid and the atomic hydrogen distribution differs from the diffusive equilibrium value. Depending on their initial velocity distribution, the particles above the exobase execute ballistic, satellite or hyperbolic orbits (Chamberlain, 1963). The particles in the ballistic orbits leave from the exobase in elliptic orbits only to reenter it at a conjugate point. The satellite orbits are also elliptical, but unlike the ballistic orbits, they do not intersect the exobase. For the hydrogen geocorona, the 'satellite critical level' lies at nearly 2.5 earth radii (Chamberlain, 1963), below which, permitted by their initial kinetic energy the particles are in complete isotropic distribution and above which such satellite orbits are rare. Particles with sufficiently high kinetic energy and orginiating from the exobase

take up hyperbolic orbits and escape from the planetary corona into the interplanetary space. Furthermore, rare collisions of escaping particles in hyperbolic orbits with the atomic oxygen within the exosphere have the effect of shifting these particles from one hyperbolic orbit to another with a lower perigee. Some of the hyperbolic orbits, therefore, penetrate the exobase and this phenomenon may be taken as equivalent to an effective reduction in the escape rate. The reduction of about 10% below Jean's escape rate results (Fahr, 1971 b). The returning particles further influence the velocity distribution of the escaping particles.

Meier and Mange (1970) have combined the Kockarts-Nicolet (1962) model of atomic hydrogen distribution below 500 km. with the Chamberlain (1963) model for higher altitudes. Fig. 9 taken from Meier and Mange (1970) shows the hydrogen density distribution out to 10^5 km altitude, the models are normalized to 3×10^7 H atoms cm^{-3} at 100 km (three times the Kockarts-Nicolet (1962) value).

3.3.3 SALIENT FEATURES AND RESULTS OF THE THEORY OF GEOCORONAL HYDROGEN EMISSIONS

Johnson and Fish (1960) suggested that the geocoronal hydrogen emissions at night probably result from the multiple scattering of solar UV on the atomic hydrogen of the geocorona. Brandt (1962a, 1962b) suggested that the night sky Lyman Alpha (L_α) arises from the 'direct scattering' of solar L_α on the atomic hydrogen of the 'geocoma', the region of the terrestrial atmosphere 10 earth radii and beyond which is populated by escaping hydrogen atoms. For the observed geocoronal L_α emission rates about the time of

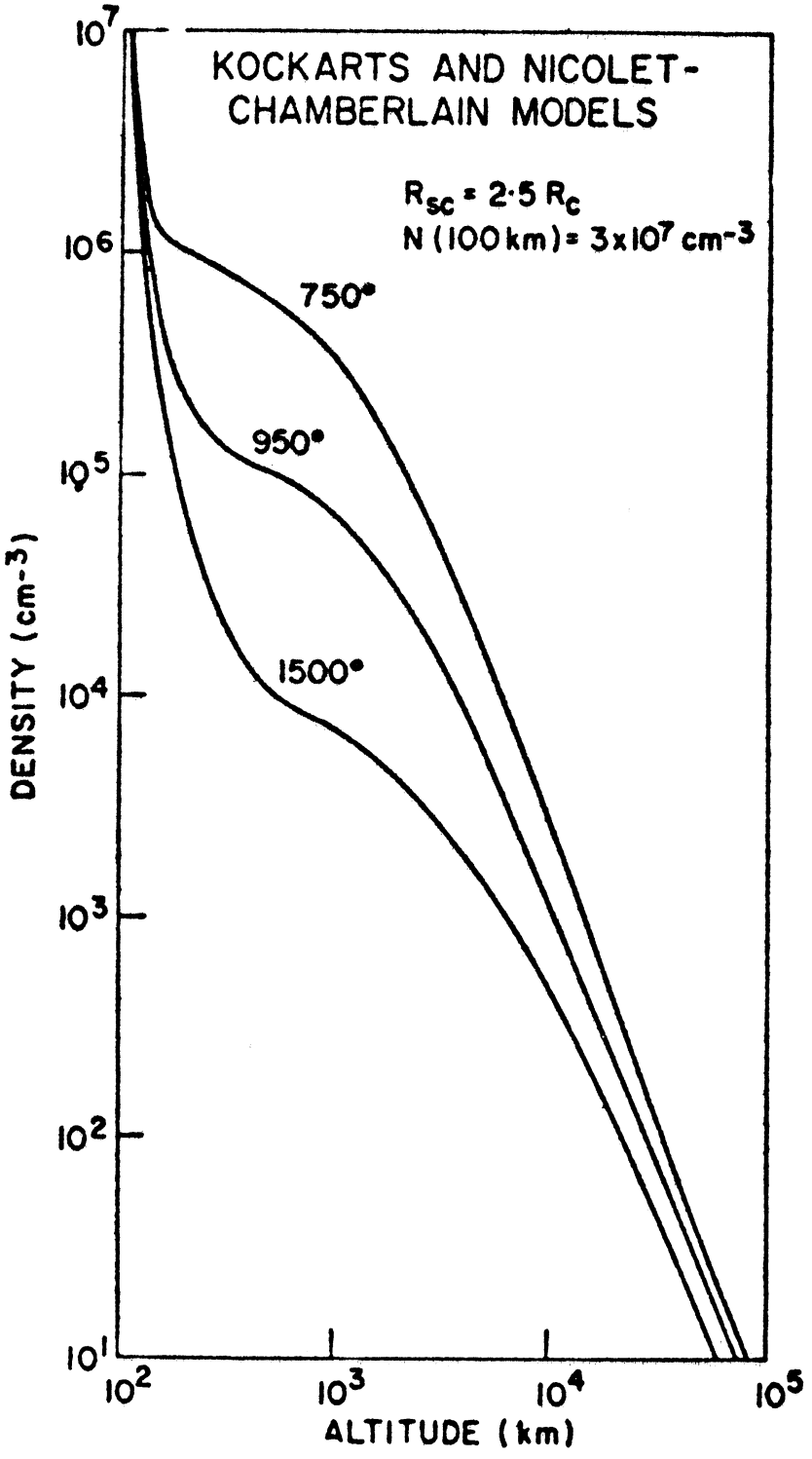

Fig. 9. Hydrogen density as a function of altitude for several exospheric temperatures. The models are normalized to $3 \times 10^7\ cm^{-3}$ at 100 km and have critical satellite altitude of 2.5x exobase height (Meier and Mange, 1970).

Brandt's predictions (Chubb et.al., 1961), approximately 10^{12} atoms·cm.$^{-2}$ column are required beyond 10 earth radii. Donahue and Thomas (1963b) discovered an error in Brandt's calculations of the atomic hydrogen escape flux and found the abovementioned column abundance of atomic hydrogen in the geocoma to be improbable. Following Johnson and Fish's (1960) suggestion, Donahue (1962), Donahue and Thomas (1963a) and Thomas (1963) investigated the problem of radiative transfer in the geocorona by considering multiple scattering of the solar L_α by the geocoronal hydrogen, and they found the results of the calculations to be fairly consistent with the observations. Donahue (1964, 1966) extended the L_α calculations to include the geocoronal H_α emission.

The geocoronal L_β and H_α problems are fundamentally similar in nature to the L_α problem. The H_α emission results from the fluorescence radiation of atomic hydrogen in the n=3 state (Fig. 5). Most of the contribution to the population of the n=3 state arises from the direct excitation of the ground state atomic hydrogen (see Table 4 for a general idea), the contribution from the higher orbitals is negligible. The hydrogen atoms in the n=3 state fluoresce to n=2 state giving an H_α photon and to n=1 state giving a L_β photon. The probability of emitting L_β photon over H_α photon is 89 to 11. Therefore, in principle, the geocoronal H_α emission rate profile can be obtained from the L_β profile on introducing appropriate scaling factors. The geocoronal L_β calculations are not quite as sensitive to the choice of the lower boundary as the L_α calculations. The absorption of L_β by O_2 is very pronounced below 150 km. While in the case of L_α, because of an atmospheric window at the L_α wavelength, its absorption

by O_2 is not very significant down to the mesopause region.

Thomas' (1963) extensive analysis of geocoronal L_α assumes spherically symmetric hydrogen distribution, absorption of L_α by O_2 only (influence of other atmospheric species is indirect in the sense that they simply alter the hydrogen distribution), Doppler width of the spectral feature independent of altitude and a cut off for the extent of the geocorona at 2.5 earth radii. Donahue (1964), in explaining the geocoronal H_α emission made the same basic assumptions. Meier (1969) improved on Donahue's calculations by taking a more realistic hydrogen distribution, extending the geocorona to 3 earth radii and considering the non-conservative scattering probability. In order to explain Tinsley's (1967, 1968) H_α measurements, Tinsley and Meier (1971) improved upon Meier's (1969) work by extending the calculations to 12 earth radii and applying more appropriate corrections to the observed geocoronal H_α observations.

In the radiative transfer problem of the geocorona, the population of the hydrogen atoms in an excited state is composed of two terms, one due to the direct solar excitation and the other arising from multiple scattering of the solar UV. However, in the anti-solar direction, due to the absence of direct solar excitation, only multiple scattering contributes to the observed geocoronal hydrogen emissions, therefore excitation rate is minimum in this direction.

For the purpose of the present investigation, one of the significant results of the geocoronal radiative transfer calculations of earlier authors is that the geocoronal excitation rate is maximum high in the exosphere despite the fact that the maximum in the atomic hydrogen concentration occurs quite low in the thermosphere (Meier,

1969). Fig. 10 taken from Meier (1969) illustrates the H_α source function as a function of optical depth (lower scale) and altitude (upper scale) for a solar depression angle of 45^o. It should be noted in this figure that of the H_α intensity above 100 km , nearly 90% comes from above 215 km and 96% from above 110 km. The emission rate peaks quite high in the exosphere. Therefore the temperature retrieved from the Doppler profile measurements of the geocoronal H_α line should indeed indicate tht exospheric temperature. Also, the geocorona is optically thin to the H_α radiation, therefore the observed H_α emission rate is the true emission rate.

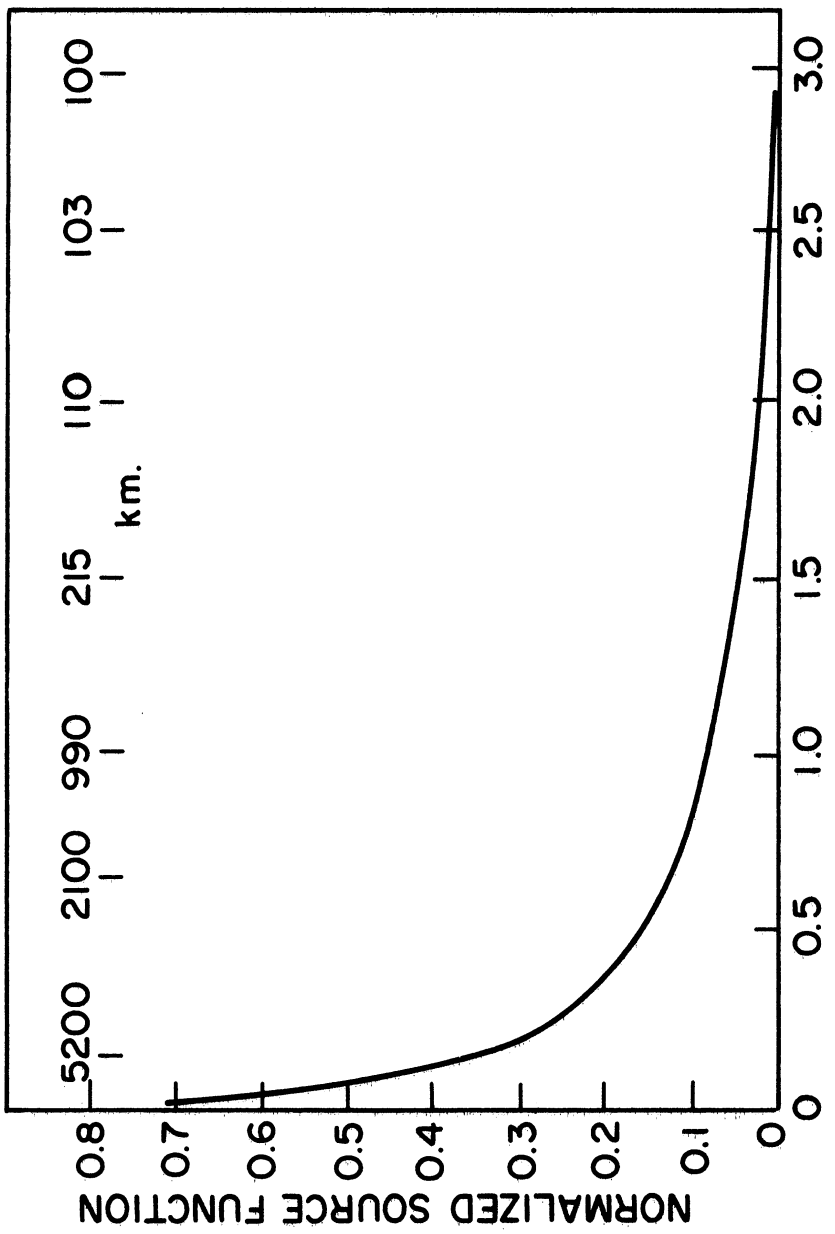

Fig.10. Source function vs. optical depth (lower scale) and altitude (upper scale) for a solar depression angle of 45^{o} (Meier, 1969).

CHAPTER IV

INSTRUMENTATION

4.1 INTRODUTION

A Fabry-Perot interferometer was used to investigate the geocoronal and possible extraterrestrial hydrogen Balmer emissions. A Fabry-Perot interferometer combines the feature of good light gathering power together with a capability of high resolution, and, for a short range of wavelength scan, it is more convenient to use than most other optical devices (Chabbal 1953, Jacquinot 1954, 1960).

First, a summary of the relevant information gathered from the previous chapters will be presented in this chapter. Such a summary, together with the knowledge of the theory of the instrument (given in Sec.4.3) should be helpful in the selection of the values for the various instrument parameters. A discussion of the instrument parameters used in this work will be given in Sec. 4.5.

4.2 SUMMARY OF THE RELEVANT INFORMATION

(i) The zodiacal light and gegenschein, if present, are suspected to show as a broad continuum background on which the emission lines are superimposed. Zodiacal light is pronounced only for small solar depression angles, usually $\lesssim 15^{o}$; it can thus be avoided by restricting the observations to solar depression angles $\gtrsim 15^{o}$.

(ii) An isotropic distribution of diffuse galactic H_{α} over the entire sky is likely and it is also suspected to be like a broad continuum background. The regions of the Galaxy which are rich in H_{α} are

presumably confined to within ± 15° of galactic latitude. If any galactic H_α emission features are present, they are expected to be Doppler shifted from the geocoronal H_α line. Moreover, galactic H_α should be a double line profile as opposed to a single line geocoronal H_α profile since the galactic H_α results from a recombination process.

(iii) The interplanetary H_α line is expected to be extremely weak, with a maximum possible intensity of 0.1R. It should also be Doppler shifted from the geocoronal H_α line and the Doppler temperature associated with it is suspected to be considerably different from the geocoronal temperature. The H_β line intensity is at least a factor of 10 smaller than the H_α intensity.

(iv) Any electron excited source of the H_α line is at least an order of magnitude smaller than the fluorescence emission rate of the interplanetary H_α.

(v) A very weak, narrow and Doppler stationary geocoronal H_α is expected. Its emission rate is highly dependent upon the geometry of illumination; the maximum intensity is expected for small solar depression angles. Large diurnal and seasonal variations in its emission rate are possible. Its excitation rate is greatest high in the exosphere (Meier, 1969), therefore the associated Doppler temperatures are expected to be typically in the 1000-2000°K range. Also, since the geocorona is optically thin to the H_α radiation, the observed H_α intensity is the true intensity.

4.3 THE FABRY-PEROT INTERFEROMETER

4.3.1 THEORY

The theory and operation of a Fabry-Perot interferometer have been extensively discussed in the literature (Fabry and Perot

1899; Jacquinot 1954, 1960; Born and Wolf, 1965). A brief account of the theory pertinent to the present investigation program is given below.

Basically a Fabry-Perot interferometer consists of two circular plates made out of glass, fused silica or quartz. In principle, the plates are perfectly flat, plane and parallel. The inside surfaces of these plates are coated with multiple layers of some dielectric for high reflectivity and low absorption at the wavelength under investigation. A certain desired spacing is maintained between the plates with the help of a high precision spacer ring. A fixed spacing Fabry-Perot interferometer is sometimes referred to as a Fabry-Perot etalon. A ray of light incident at an angle i to the etalon axis (i = 0^{o} for 'axial' spectrometer) undergoes absorption, transmission and multiple reflection between the plates (see Fig. 11). Thus the incident ray is divided into an infinite number of rays reflected and transmitted parallel to one another. Superposition of two adjacent transmitted rays results in constructive or destructive interference when they recombine at infinity. Therefore, one observes an interference ring pattern in the focal plane of an objective lens which is used to converge the transmitted rays.

The optical path difference between two successive rays emerging from a Fabry-Perot etalon is given by the following expression

$$\Delta \ell = 2 \mu t \cos i \qquad (4\text{-}1)$$

where

μ = Refractive index of the medium between the plates

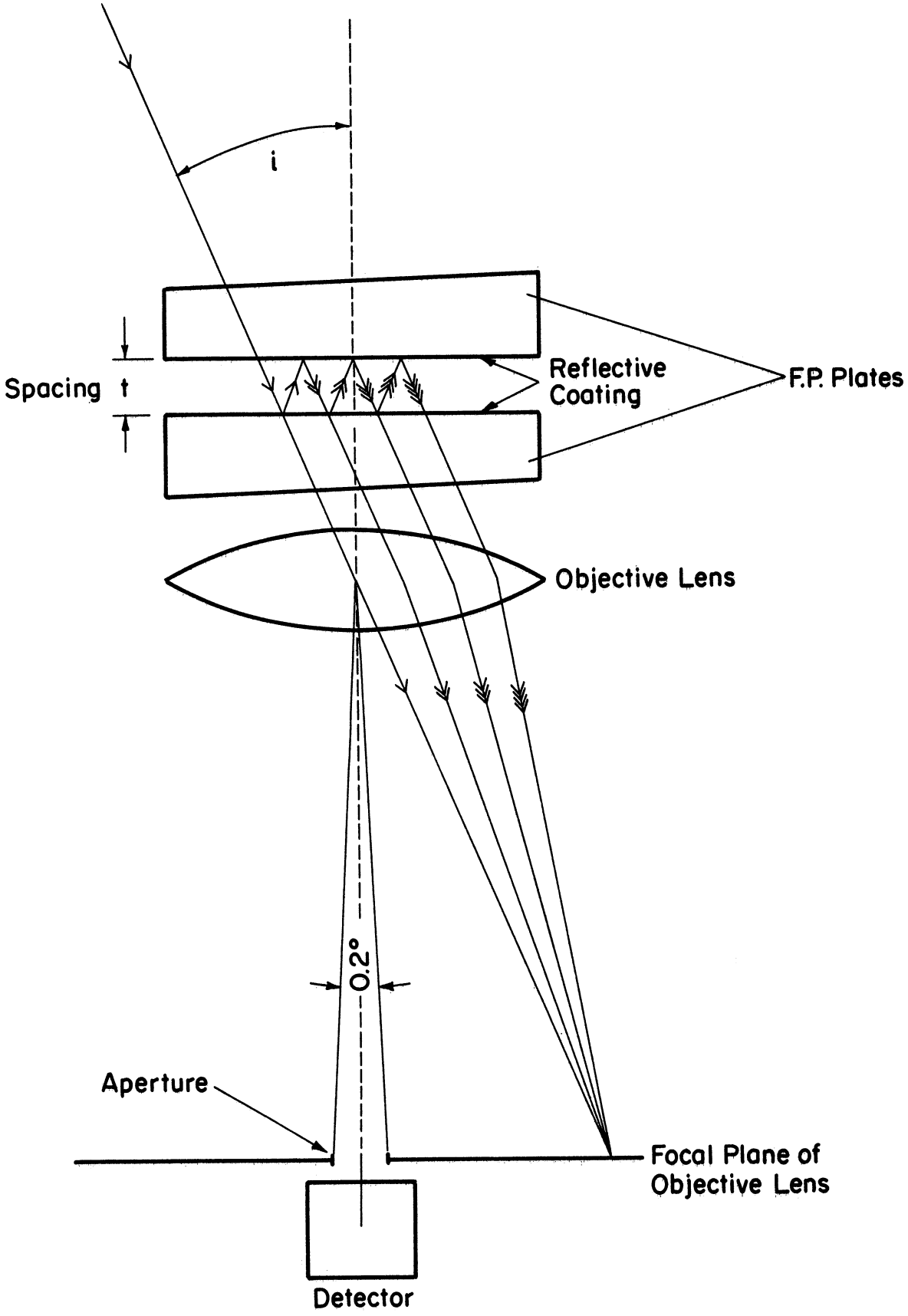

Fig. 11. Schematic of a Fabry-Perot interferometer.

t = Spacing between the plates

The product μt is usually referred to as the optical thickness of the Fabry-Perot interferometer.

If λ is the wavelength of the incident radiation, and if one defines a parameter m as follows

$m = \Delta\ell/\lambda$

i.e.

$$m = 2\mu t \quad \lambda^{-1} \text{ Cos } i \qquad (4\text{-}2)$$

then

m = Integer, for constructive interference of the transmitted rays.

and

m = $\frac{1}{2}$ x Integer, for destructive interference of the transmitted rays.

The separation between two successive orders of interference, called the free-spectral range $\Delta\lambda_{FSR}$, is given by

$$\Delta\lambda_{FSR} = \frac{\lambda^2}{2t} \text{ (in units of } \mathring{A}) \qquad (4\text{-}3)$$

and free-spectral range $\Delta\sigma_{FSR}$ in cm^{-1} is

$$\Delta\sigma_{FSR} = \frac{1}{2t} \text{ (in units of } cm^{-1}) \qquad (4\text{-}4)$$

In both Expressions (4-3) and (4-4), assumption was made that $\mu \simeq 1$ and $i \simeq 0^{o}$.

The wavelength for constructive interference can be scanned across by varying i, μ or t. One of the most accurate and convenient methods of accomplishing a scan across one or more free-spectral ranges is by varying the pressure of the scanning gas which effectively changes the μ of the medium between the plates.

4.3.2 INSTRUMENT FUNCTION

Theoretically, if the Fabry-Perot plates are perfectly plane and parallel with no imperfections, the size of the aperture is negligible and the reflectivity R of the plates unity, then under constructive interference, the instrument-function will simply be a series of Dirac δ-function spikes (Born, 1965)

$$W(\sigma) = \sum_{o}^{\infty} \delta(\sigma - \sigma_o) \qquad (4\text{-}5)$$

i.e. ideally a Dirac δ- function signal incident upon the Fabry-Perot plates will simply emerge as a Dirac δ- function and if the incident signal had a certain width associated with it, it would remain unchanged on passing through such an ideal optical system.

In reality, of course none of the above mentioned ideal situations is completely satisfied. The effect of $R < 1$, surface imperfections (microdefects and/or sagging of the plates) and finite size of the aperture is to introduce a certain amount of 'instrument' broadening in the radiation incident on top of the etalon. The finite width instrument function $W(\sigma)$ is then the result of convolution of Airy function, $A(\sigma)$; gaussian microdefect function, $D_g(\sigma)$; spherical plate defect function, $D_f(\sigma)$; and the Aperture function, $F(\sigma)$; i.e.

$$W(\sigma) = A(\sigma) * D_g(\sigma) * D_f(\sigma) * F(\sigma) \qquad (4\text{-}6)$$

and, if $G(\sigma)$ is the spectral density of the source function, the observed signal $Y(\sigma)$ is given by the following expression

$$Y(\sigma) = \int_{o}^{\infty} G(\sigma_o) \quad W(\sigma - \sigma_o)\, d\sigma_o \qquad (4\text{-}7)$$

For an excellent review of the various abovementioned instrument functions, associated widths and finesses the reader is referred to Hernandez (1966) and Roble (1969). The finesse of the fringes is defined as the ratio between the free-spectral range and the instrument half width ('half width' is defined as the full width at half the peak intensity).

4.4 DOPPLER HALF WIDTHS OF THE H_α AND H_β LINES

The Doppler half width $\Delta D_{1/2}$ of a line profile is the full width at half the maximum amplitude (FWHM); and it is given by the following expression for an atomic hydrogen line.

$$\Delta D_{1/2} = 2(\ell n 2)^{1/2} \cdot \sqrt{\frac{2kT}{m_H}} \cdot \frac{\lambda_o}{c} \qquad (4\text{-}8)$$

or

$$\Delta D_{1/2} = 7.135 \times 10^{-7} \quad \lambda_o \sqrt{\frac{T}{M_H}} \quad \text{Å} \qquad (4\text{-}9)$$

where

k = Boltzman constant (1.38×10^{-16} erg/^oK)
c = Velocity of light
λ_o = H_α wavelength (6562.8 Å)
m_H = Mass of the hydrogen atom in gm. (1.672×10^{-24} gm.)
$\ell n 2$ = Natural logarithm of 2.0
T = Temperature of emitting region in ^oK
M_H = Atomic Mass number of the emitting species
(= 1 for H, = 16 for O)

The Doppler half widths of the H_α and H_β lines for a range of temperatures are presented in Table 6.

TABLE 6

Doppler Half Widths of the H_α and H_β Lines

$T(^oK)$	$\Delta D_{1/2}(\mathring{A})$	
	H_α (6562 · 8 $\mathring{A}$)	H_β (4861 · 3 $\mathring{A}$)
100	.046	.034
1000	.148	.110
2000	.210	.155
5000	.332	.246
10000	.460	.340

4.5 SELECTION AND JUSTIFICATION OF THE VALUES OF THE VARIOUS INSTRUMENT PARAMETERS

4.5.1 SELECTION OF THE HYDROGEN BALMER WAVELENGTH FOR THIS STUDY

The Fabry-Perot interferometer of the Michigan Airglow Observatory (MAO), originally constructed for the SAR-arc study (Roble, 1969) has a full field of view of 0.2^{o}, resolving power of 350,000, free spectral range of 0.5 cm^{-1} (1 cm spacing), an overall finesse of approximately 12 and the reflectivity of the etalon = .87 at 6300 $\mathring{A}$. However, at hydrogen Balmer Beta wavelength (H_β=4861.3$\mathring{A}$), the reflectivity of the Fabry-Perot plates is a meagre 10% (see Fig. 12; and Appendix C for the techniques of measuring the reflectivity). With 10% reflectivity and assuming that all other finesses have about the same values as at 6300 $\mathring{A}$, an overall finesse of nearly 1 is expected at H_β wavelength. A finesse of 1 implies that the instrument width is equal to the free spectral range! Therefore, one does not expect to see any interference fringe pattern due to the tremendous interorder overlap. This fact was further confirmed when no geocoronal H_β emission was observed in some trial runs made in May, 1971. Therefore, even though the H_β line lies in the part of the nightglow spectrum which is relatively free from the hydroxyl lines, it could not be studied using the MAO interferometer.

Recoating the etalon for a better reflectivity at the H_β wavelength is not only a time consuming process, it also renders it impractical for use in most other parts of the visible spectrum. Therefore, the emphasis was shifted to studying the nightsky H_α line. The H_α emission is considerably more intense than the H_β emission

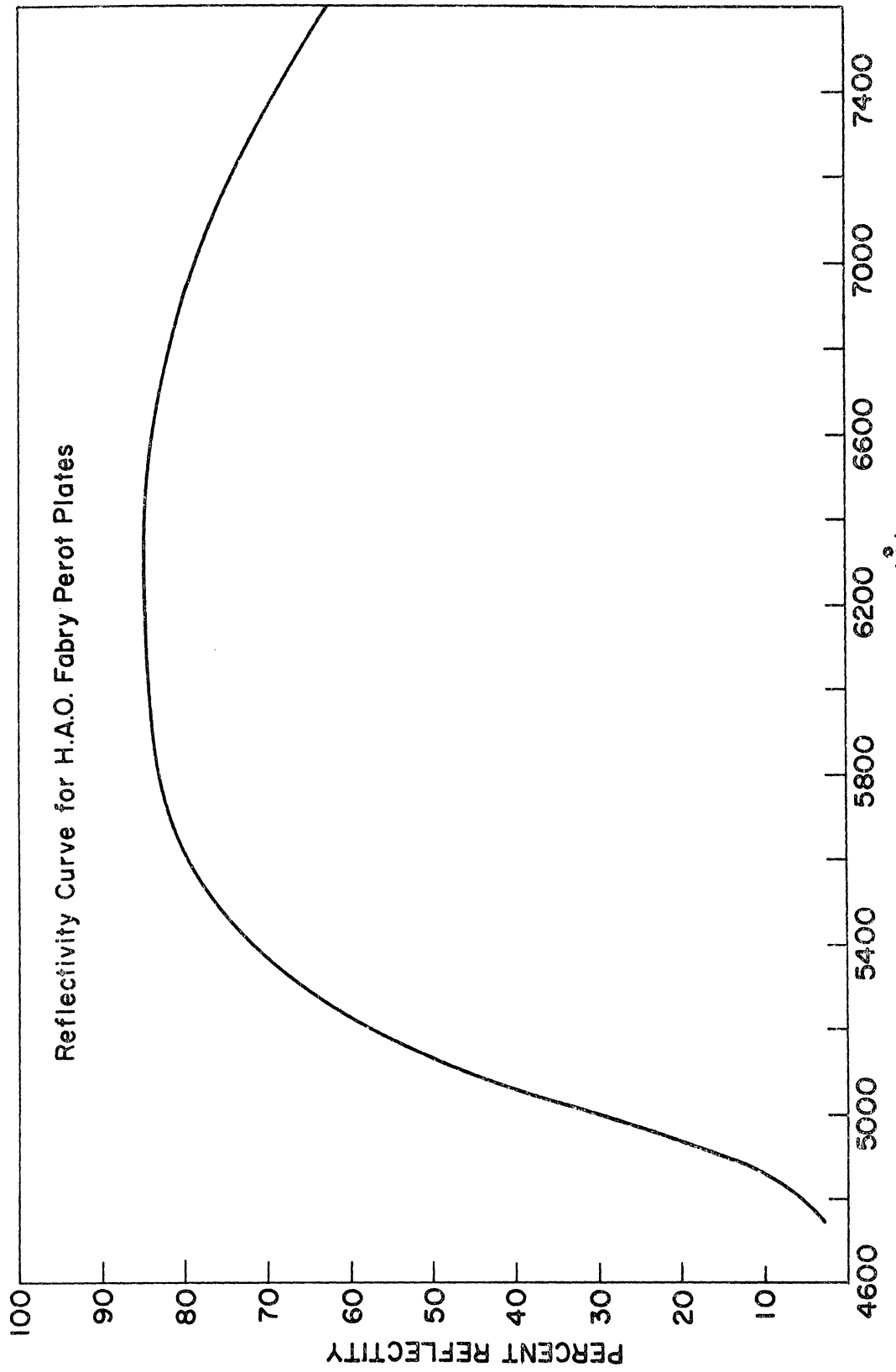

Fig. 12. Reflectivity curve for the Huntsville Airglow Observatory (HAO) Fabry-Perot plates. The Michigan (MAO) plates have a similar curve.

and its excitation mechanism being the same as for H_β, a study of the H_α line provides the same information of geophysical interest as the H_β line. Since the H_α line is flanked by several hydroxyl lines of the OH(6-1) band on either side of its line center, its measurement is more difficult than that of the H_β line. For the study of the night-sky H_α line, a number of modifications in the existing Fabry-Perot interferometers of MAO and Huntsville Airglow Observatory, Marshall Space Flight Center (HAO) were made.

4.5.2 SPACING BETWEEN THE PLATES

The geocoronal temperature is suspected to be in the vicinity of 1000-2000°K. The corresponding range for H_α Doppler half widths (FWHM) is 0.15 to 0.21 Å. The reflectivity of the plates at H_α was measured to be 83%. (see Fig. 12) which is very close to the value at 6300 Å and is quite acceptable. A 1 cm spacing between the plates gives a free-spectral range of ~0.21 Å at H_α wavelength. Since the suspected width of the geocoronal H_α is close to the value of the free-spectral range, an inter-order overlap is quite likely. The free-spectral range at H_α wavelength was expanded four times by using a 0.25 cm spacing between the plates. Three small 'spacer discs' were held in place between the plates with the help of an aluminum ring (see Appendix D). An overall instrument finesse of 10 and a 0.25 cm spacing results in an instrument width of nearly 0.08Å. Thus the instrument width is narrow enough even for measuring a 100°K H_α line. During the actual nightsky observations, an overall finesse up to 14 was achieved.

4.5.3 SCANNING ACROSS THE LINE PROFILE

Of the various means of scanning across the emission

profile mentioned in Sec. 4.3.; the pressure scanning is most accurate and convenient for the present work. The refractive index, μ of an ideal gas at laboratory temperature varies linearly as its pressure (Mack et. al., 1963), i.e.

$$\mu = 1 + \epsilon_o p \qquad (4\text{-}10)$$

where

$$\epsilon_o = (\mu_o - 1) \qquad (4\text{-}11)$$

μ_o = refractive index of the gas at the Standard Temperature and Pressure (STP)

p = pressure of the gas in pounds per square inch

From Equation (4-10), one obtains

$$d\mu = \epsilon_o dp \;, \quad \text{i.e.} \quad d\mu \propto dp \qquad (4\text{-}12)$$

Also $$dp \propto d\lambda \qquad (4\text{-}13)$$

Therefore, from Equations (4-12) and (4-13), one finds that

$$d\mu \propto dp \propto d\lambda \qquad (4\text{-}14)$$

Thus, the wavelength of interest may be continuously scanned by varying the pressure of the scanning gas.

At the H_α wavelength, the free spectral range for a 0.25 cm. spacing is approximately 7.5 PSI in terms of the pressure of dry nitrogen gas (N_2). Since the MAO pressure gauge is good only for 0-5 PSI range, it does not cover the entire free spectral range. An attempt was made to use Sulfur Hexafluoride gas (SF_6) for scanning. SF_6 has a refractive index nearly 3 times that of N_2, therefore, for the same change in pressure, SF_6 is capable of scanning nearly three times as far in wavelength as N_2, i.e.

$$\frac{(d\lambda/dp)_{SF_6}}{(d\lambda/dp)_{N_2}} \simeq 3 \qquad (4\text{-}15)$$

A comparison of Figs. 13 and 20 illustrates the advantage of SF_6 over N_2 for scanning. It should be noticed in these figures that the free-spectral range at the He-Ne laser wavelength (6328 Å) in terms of the SF_6 pressure is about one third the value in terms of the N_2-pressure.

Experience with the SF_6 gas proved, however, that the gas is very viscous and the purging time is of the order of a day, therefore SF_6 was not found practical for scanning. Instead, a 0-10 PSI pressure gauge was installed both in the Michigan and the Huntsville facilities, so that N_2 could be used for scanning.

4.5.4 THE H_α FILTER

The most crucial of the hydroxyl lines of OH (6-1) band in the vicinity of the H_α wavelength (λ_o = 6562.8 Å) are at (λ_o+6.2)Å (λ_o + 10.7) Å and (λ_o - 9.1) Å (Chamberlain 1961, Krassovsky and Shefov 1962). Therefore a narrow pass band filter of $\lesssim$ 3Å full width at half its maximum transmission (FWHM), centered at 6570 Å for zero angle of incidence, and, with its transmission falling very steeply away from the line center was ordered. The peak transmission for zero incidence is centered somewhat above the H_α wavelength since the peak transmission wavelength normally drifts toward the blue on ageing of the filter. Only one of a series of H_α filters received from the manufactures had the specifications anywhere near the desired specifications (see Fig. 14). This filter was used in the present work. The effect of the filter is to suppress all etalon transmission peaks except those near the H_α wavelength (see Fig. 15).

The complete specifications of the Fabry-Perot interferometer eventually used for the present H_α study are presented in Table 7.

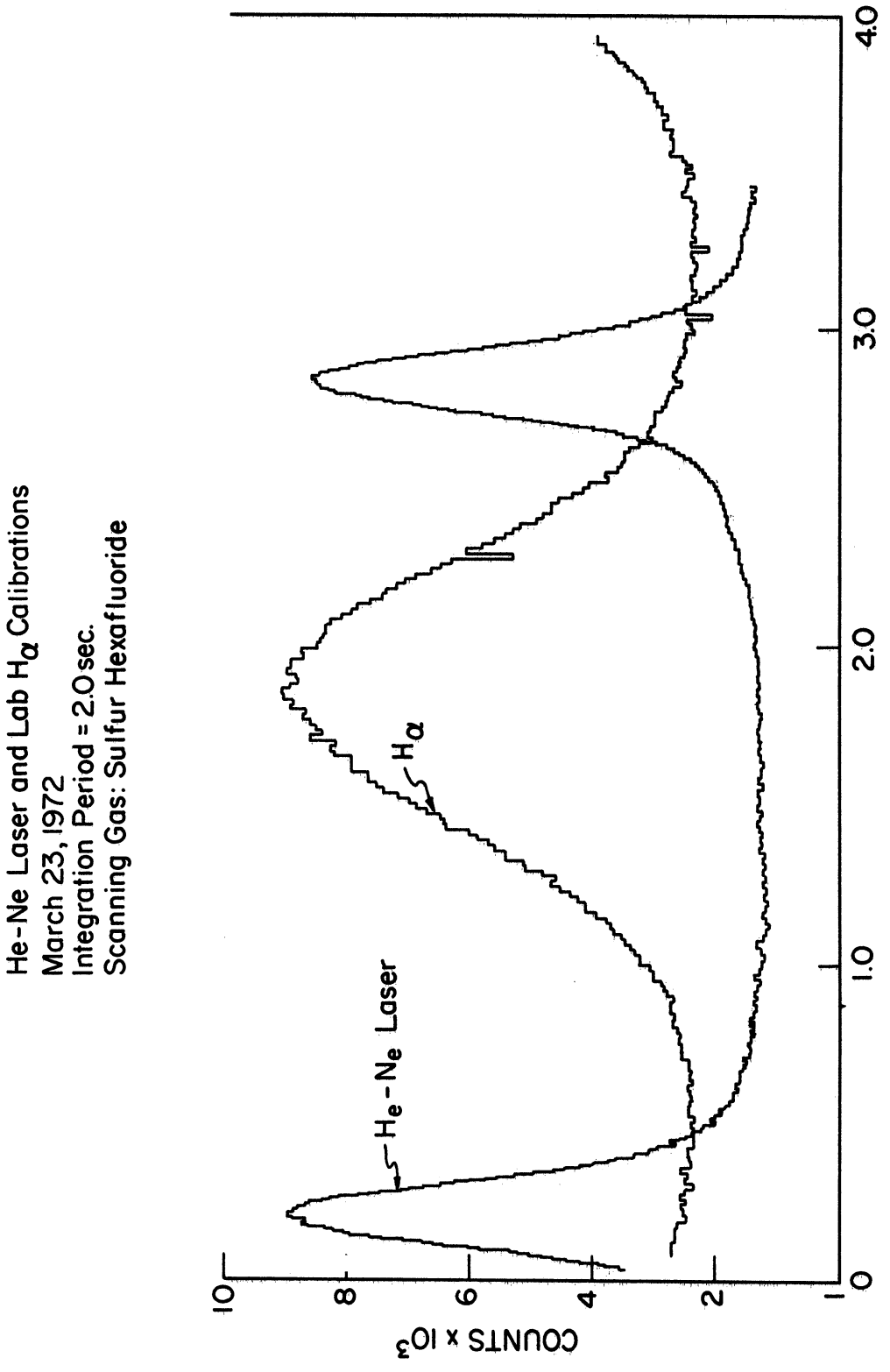

Fig. 13. Laboratory calibrations using SF_6 for scanning.

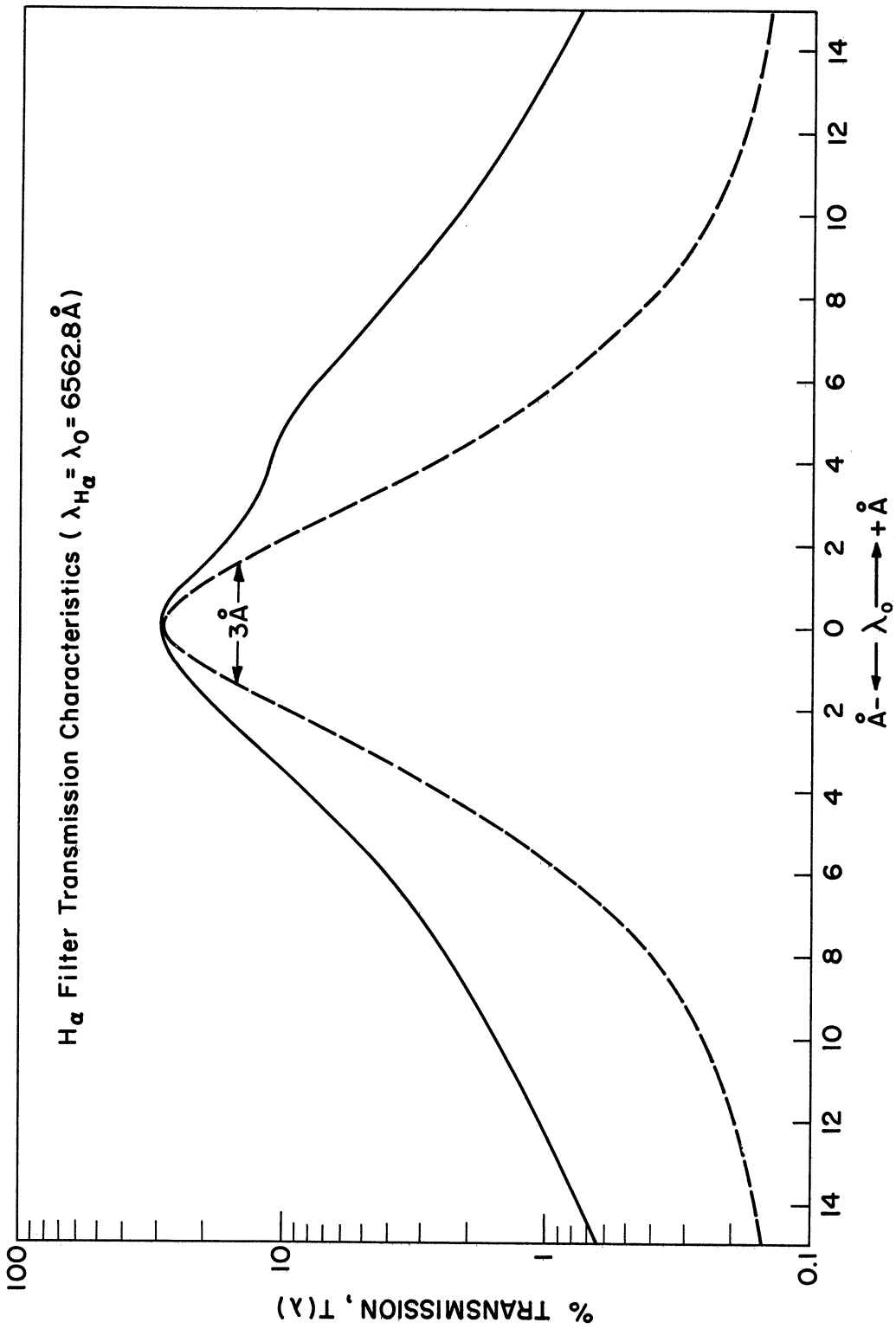

Fig. 14. Transmission characteristics of the H_α filter used in the present investigation (solid line curve). The dashed curve represents the ideal specifications.

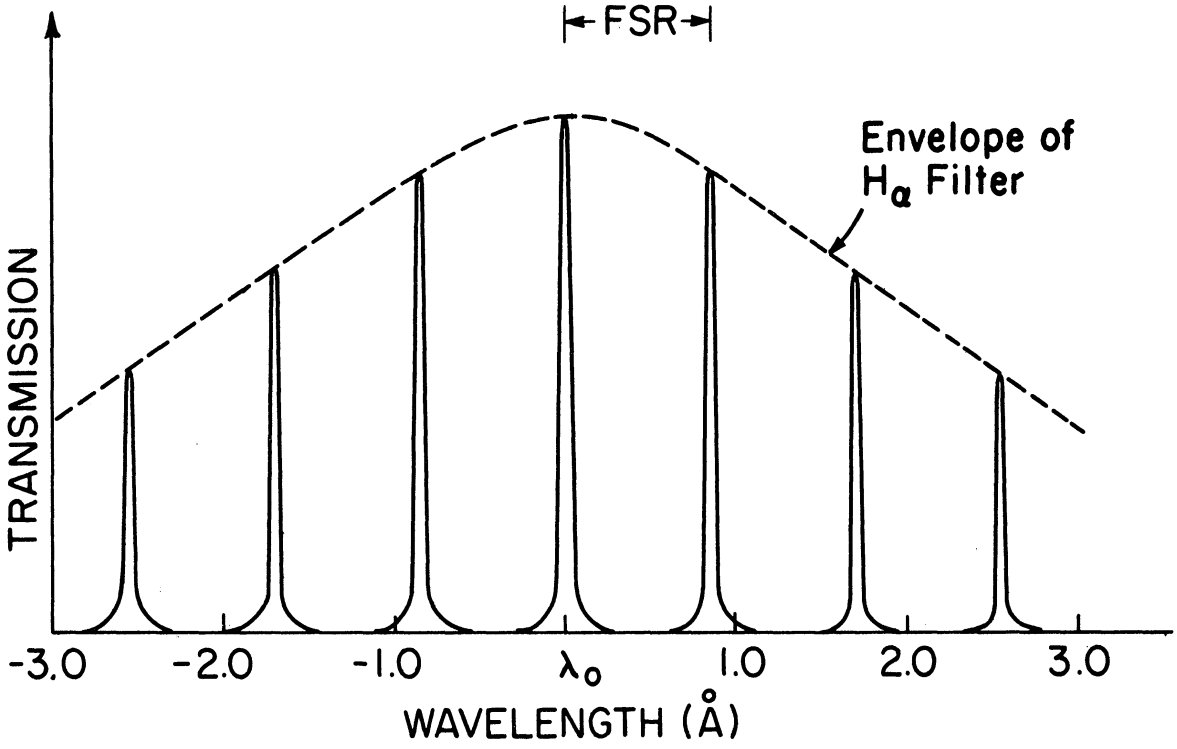

Fig. 15. Sketch illustrating the part played by the interference filter in the Fabry-Perot interferometer. Etalon transmission peaks far from λ_o are suppressed by the filter.

TABLE 7

Specifications of the MAO and HAO Fabry-Perot Interferometers

1. Etalon plates	
full diameter	15.0 cm
effective diameter	13.3 cm
flatness	$\lambda/180$
roughness defect, N_{D_g}	38.4
reflective coatings	5 alternate layers of ZnS and cryolite
reflectivity	0.83 at 6562.8 Å
reflective finesse, N_R	16.83
spherical defect finesse, N_{D_f}	29.0
saggitta	1.13×10^{-6} cm
spacing, t	0.25 cm
2. Objective lens	121.9 cm
diameter	15.24 cm
3. Aperture	
diameter	0.436 cm
finesse	81.7
4. Instrument field of view	0.2^{o}
5. Interference filter	
diameter	5.08 cm
half-width (FWHM)	5.4 Å
peak transmission	29%
peak wavelength	6570 Å
6. Photomultiplier (ITT-FW-130)	
quantum efficiency at 6562.8 Å	4.5%
photocathode surface	S-20
effective aperture	0.254 cm
dark count (cooled to -15^{o}C)	1-2 counts sec^{-1}
(uncooled)	80-90 counts sec^{-1}
7. Resolving power	102,865
8. Operating order	7618 at 6562.8 Å
9. Free spectral range	0.86 Å ($2.0\ cm^{-1}$)
10. Scanning gas	High pure dry N_2 and SF_6
11. Pressure change for 1 order	7.52 PSI (N_2) at 6562.8 Å
12. Overall instrument finesse	13.5

CHAPTER V

OBSERVATIONS, DATA AND THEIR ANALYSIS

5.1 INTRODUCTION

Night sky H_α measurements were carried out on several occasions between December 1971 and October 1972. The details of the observation scheme and the raw data for these observation periods are presented in the following sections. Prior to the nightsky H_α observations, the instrument was optically adjusted and its performance evaluated by performing several different calibrations. The details of the optical alignment, adjustment and the calibrations are presented in Appendix D.

5.2 FALL 1971 H_α OBSERVATIONS

Measurements were made at the Huntsville Airglow Observatory (HAO, latitude = 34.62°N and longitude = 86.64°W-geographic) during a two week period in December 1971 on all clear nights when the moon was below the horizon.

Calculations were carried out to evaluate the azimuth of the sun at ten minute intervals for the nights of observations. Zenith angle for the observations was between 70-75° except one night when the mirrors were positioned to look in the zenith all night long. Azimuth angle of the observations relative to the sun's azimuth varied between 0° and 30° (except, of course for the zenith observations); azimuth of the mirrors was therefore adjusted every 10 min. to at least approximately satisfy the relative azimuth invariance. Observations made at low galactic latitudes ($\leq 15°$) were not considered while analyzing the data for the geocoronal H_α emission. The scans made in

the galactic latitudes larger than $\pm 15^{\circ}$ were also checked for any nongeocoronal H_α emission by performing several almucantar runs at the zenith angle of the H_α observations and looking for regions of enhanced emission, if present.

Laser and hydrogen lamp calibrations were performed just before the beginning of the nightsky H_α observations. Fig. 16 shows a typical hydrogen lamp H_α calibration for December18-19, 1971. Measurements were begun nearly $1\frac{1}{2}$ hours after sunset and terminated about $1\frac{1}{2}$ hours before sunrise. The integration period required for a measure of the peak of emission to be raised Λ standard deviations above a normal background level N_b is given by

$$t = \frac{\Lambda}{\delta^2/N_b}$$

where δ is the signal due to the emission at its maximum. (δ^2/N_b) was optimized by restricting the observations to clear, moonless nights (or when the moon was below the horizon), and performing a rapid scan over the fringe profile to avoid varying sky conditions causing variations in the atmospheric transparency. Rapid scan over the fringe profile was also essential due to the fact that the geocoronal H_α intensity is highly dependent upon the geometry of illumination. The integration periods for the December, 1971 observations were 10 and 15 sec. and the scan over the fringe took about 1 hour. The dark current of the photomultiplier tube was also minimized by cooling it to an optimum temperature of -15 to -20°C.

The geocoronal H_α emission signal was so small that it was usually impossible to distinguish it from the normal background. Consequently a large number of fringes were added to improve the signal to noise ratio. Fig. 17 shows a typical early morning H_α scan.

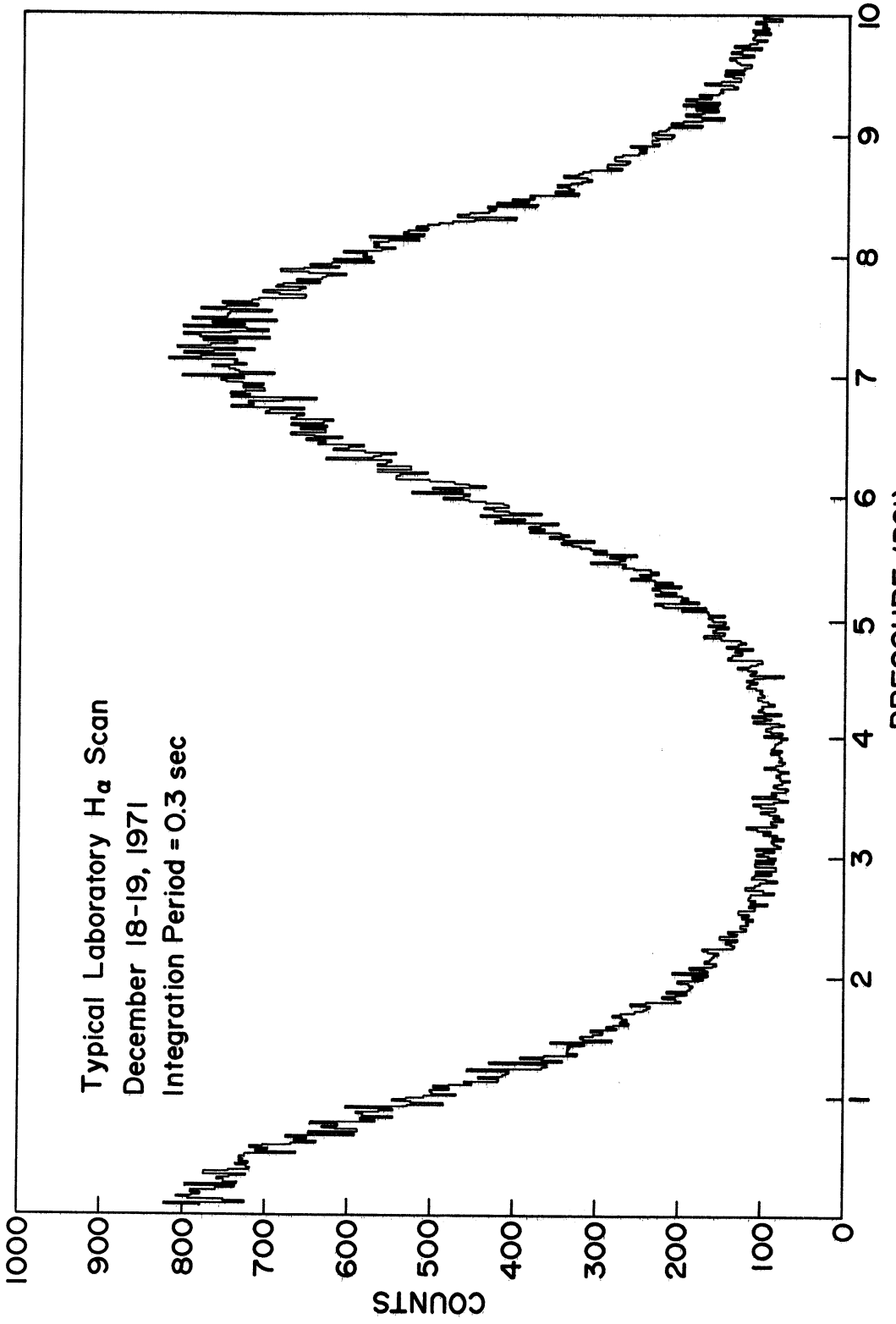

Fig. 16. Typical laboratory hydrogen lamp H_α fringe of December 18-19, 1971.

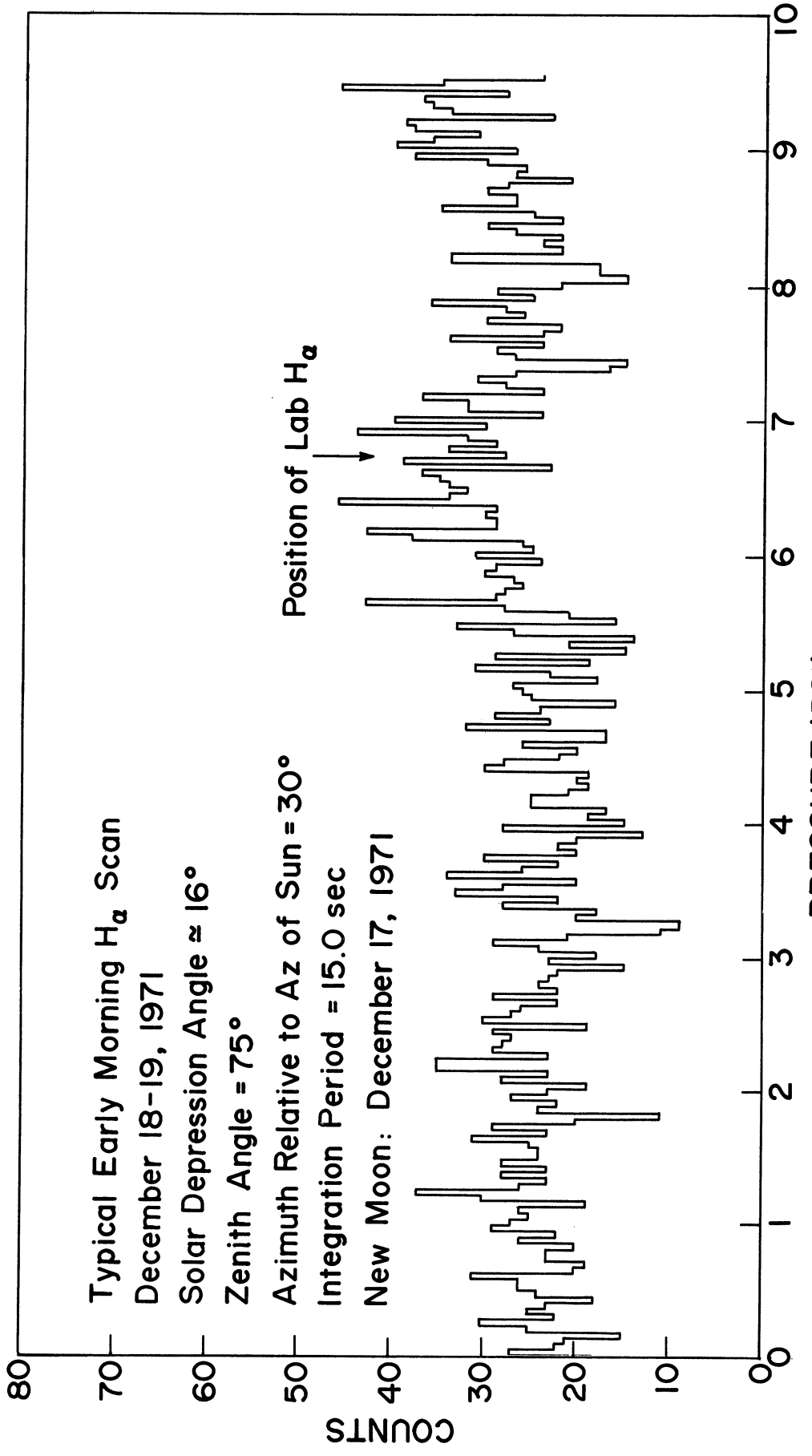

Fig. 17. Typical December 18-19, 1971 early morning H_α scan with inegration period = 15 sec. In this figure, Lab H_α is the expected position of the geocoronal H_α deduced from the laboratory hydrogen lamp H_α.

The geocoronal H_α interference fringe is barely noticeable in the scan, the evening and midnight H_α fringes are even less conspicuous because of much weaker intensities. The result of adding a sequence of two and three December 18, 1971 H_α fringes is shown in Fig. 18. A rise in the background toward the end of the scan in Fig. 18 is due to the fact that one of the fringes used in the addition was measured near sunrise. Finally, Fig. 19 shows a typical galactic H_α scan obtained looking at the Vel-Pup region. Two broad and Doppler shifted galactic H_α lines are noticeable. Amongst a number of H_α scans made with mirrors looking at different parts of the Galaxy, only the ones in the Vel-Pup region showed any discernable galactic emission features.

The December, 1971 data points had to be manually read off the X-Y plots of the scans using a Gerber scaler because the magnetic tape recorder did not function properly during this period. Therefore, only the data of the observation nights during which the most favorable sky and moon conditions prevailed (December 17 and 18, 1971) were retrieved and analyzed.

5.3 SPRING 1972 OBSERVATIONS

The observations were made at the Huntsville Airglow Observatory (HAO) from May 6 through May 17, 1972 on all clear nights when the moon was below the horizon. The experience with the Fall 1971 observations suggested a number of modifications in the observation scheme, amongst them were:

(i) Reduction in the integration period to 1 sample every 5 sec. as opposed to 10 and 15 sec. in December 1971 observations.

(ii) Introduction of a new magnetic tape recorder for the data.

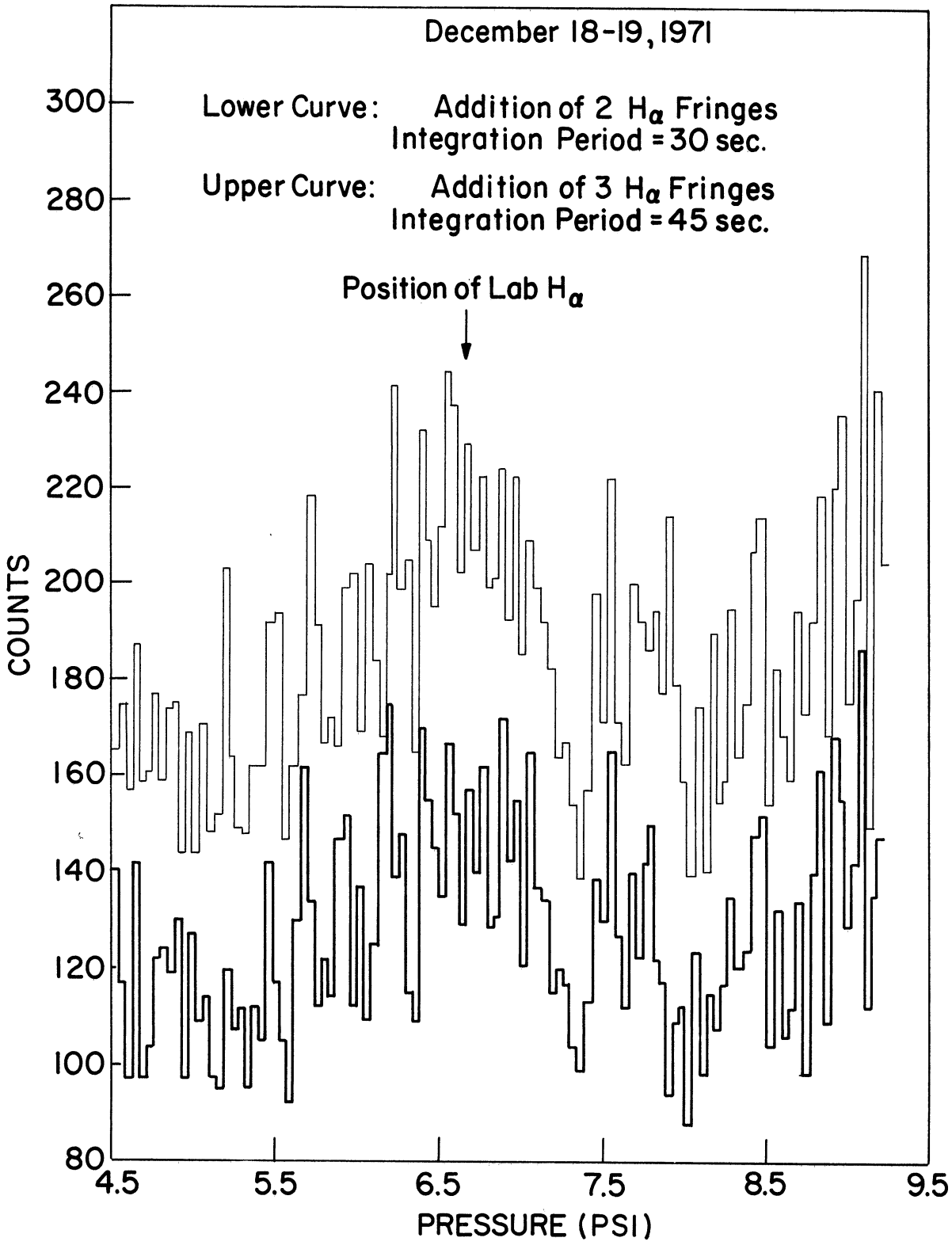

Fig. 18. Additional by hand of a sequence of two and three H_α scans of December 18-19, 1971. In this figure, Lab H_α represents the expected position of the geocoronal H_α deduced from the laboratory hydrogen lamp calibration.

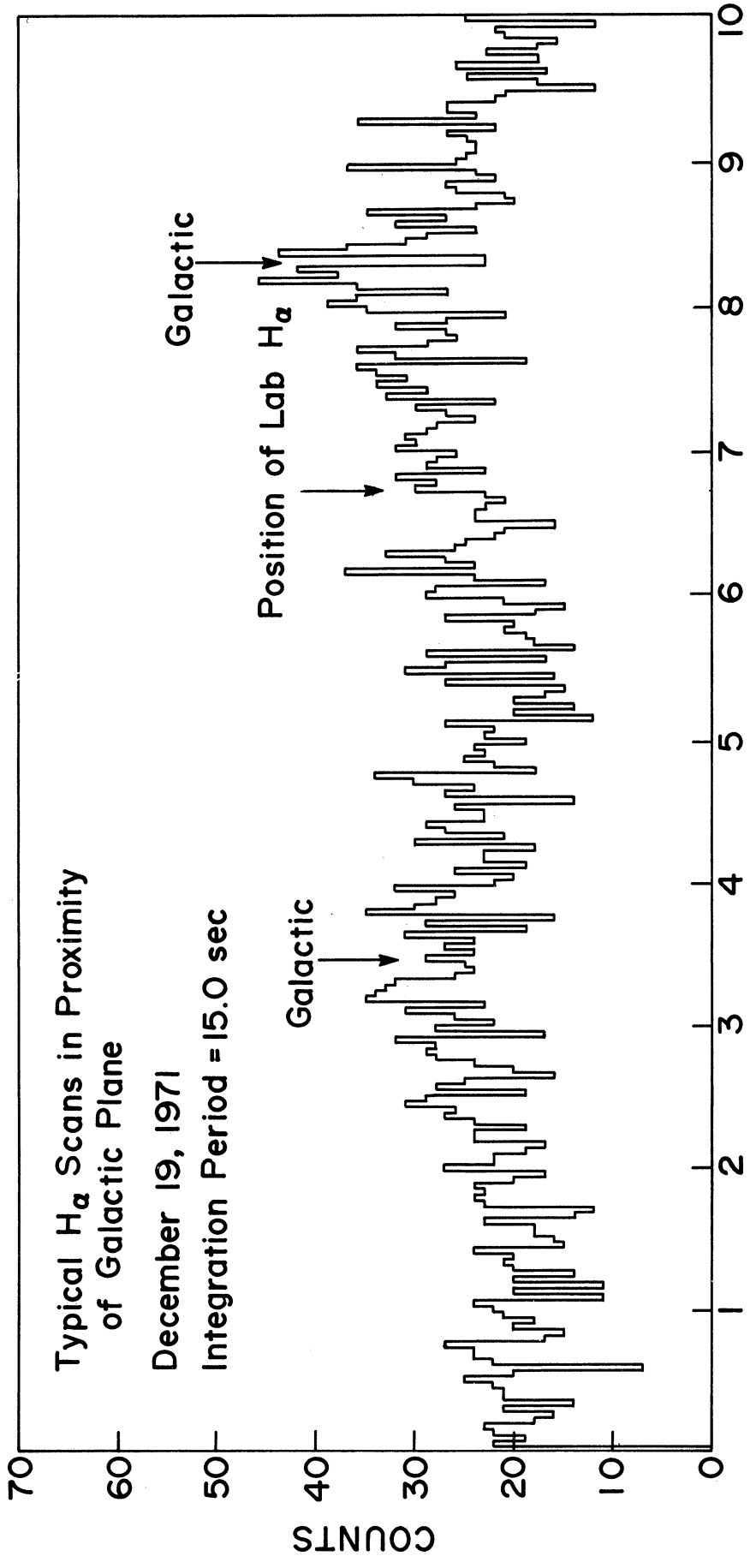

Fig. 19. Typical H_α scan in the Vel-Pup region. In this figure, Lab. H_α is the expected position of the geocoronal H_α deduced from the laboratory hydrogen lamp H_α .

(iii) Instead of looking in a fixed zenith angle while maintaining a constant azimuth relative to the sun as in December 1971, it was found more advantageous to select a few 'ideal' points on the celestial sphere and track them all night long. The ideal points are the ones which are believed to be practically devoid of any nongeocoronal H_α emission. Only points in galactic latitudes higher than 20^o were first considered. Finally, only those points which did not show an enhanced emission in their vicinity (perhaps due to galactic and stellar emissions) were selected for tracking. This was checked by making almucantar runs for the zenith angle of these points at any given time. Two to three 'ideal' points were tracked for a few hours each on the nights of observations. Observations were restricted to zenith angles $<80^o$ because of poor atmospheric transparency near the horizon and some obstacles in the field of view. Therefore, it was not possible to track a single 'ideal' point for more than a few hours on the night of the observation. The tracking mirrors in the present observatory do not have an equatorial mount, consequently a general coordinate transformation from the equatorial coordinates (right ascension and declination) to the horizontal coordinates (azimuth and zenith) was carried out as a function of the geographic latitude and longitude of the observatory, and the time and day of the year (see Appendix E for details). This transformation was then used to compute azimuth and zenith angles for the selected points every ten minutes of the observing period. This scheme of looking in the direction of one fixed right ascension and declination also ensures a constant angular displacement of the observation site from the direction of flow of the interplanetary H_α. Therefore, if there

is any detectable amount of interplanetary H_α it should be expected to be Doppler shifted from the laboratory reference by a constant amount. He-Ne Laser and hydrogen lamp calibrations were performed prior to, during and after each night's observation. Figs. 20 and 21 show a typical May 10, 1972 He-Ne laser and laboratory hydrogen lamp calibration.

The most favorable moon and sky conditions prevailed during the nights of May 10, 11, 13, and 15 and observations were carried out on all these nights. No attempt was made to perform any H_α scans in the plane of the Galaxy. Several almucantar scans were performed to ensure that the directions selected for May 1972 observations did not reveal any enhanced galactic emissions. The main purpose of the May 1972 observations was to measure the Doppler temperatures from the geocoronal H_α line and to look for any possible interplanetary H_α. Almost all of the data collected over the nights of May 10-11, 1972 and May 15-16, 1972; and partial data (due to clouds) on the nights of May 11-12, 1972 and May 13-14, 1972, were good enough for the final analysis.

The integration period for the May 1972 observations was much smaller than for the December 1971 ones. Therefore, it is practically impossible to notice the geocoronal H_α fringe in a typical May 1972 early morning scan shown in Fig. 22.

5.4 FALL 1972 H_α OBSERVATIONS

The observation scheme for this period was similar to the one used in the May 1972 observations. Several attempts were made during September and October, 1972 to carry out nightsky H_α observations from the Michigan Airglow Observatory at Ann Arbor (MAO,

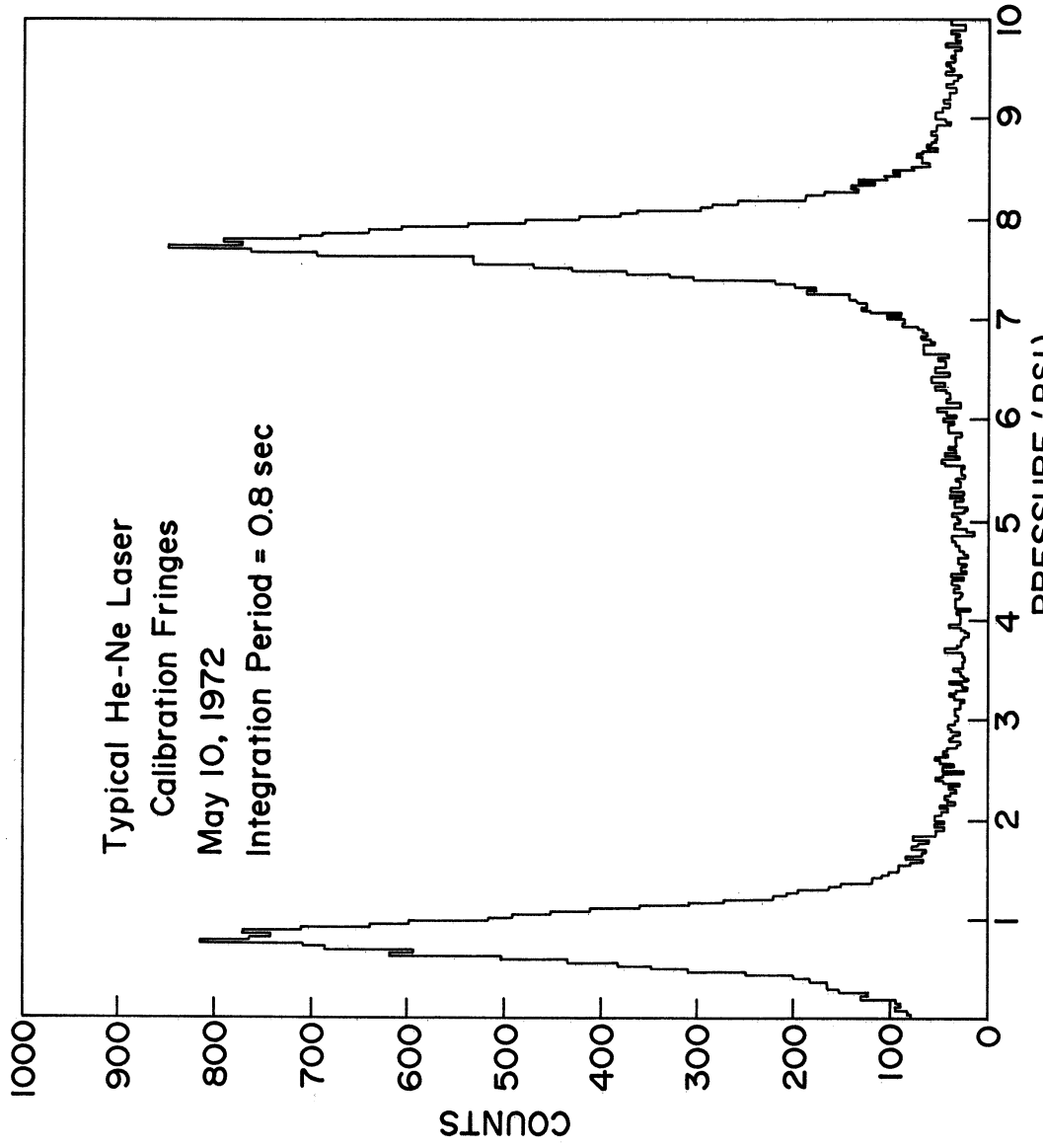

Fig. 20. Typical He-Ne Laser fringes of May 19, 1972. The scanning gas is high pure Nitrogen.

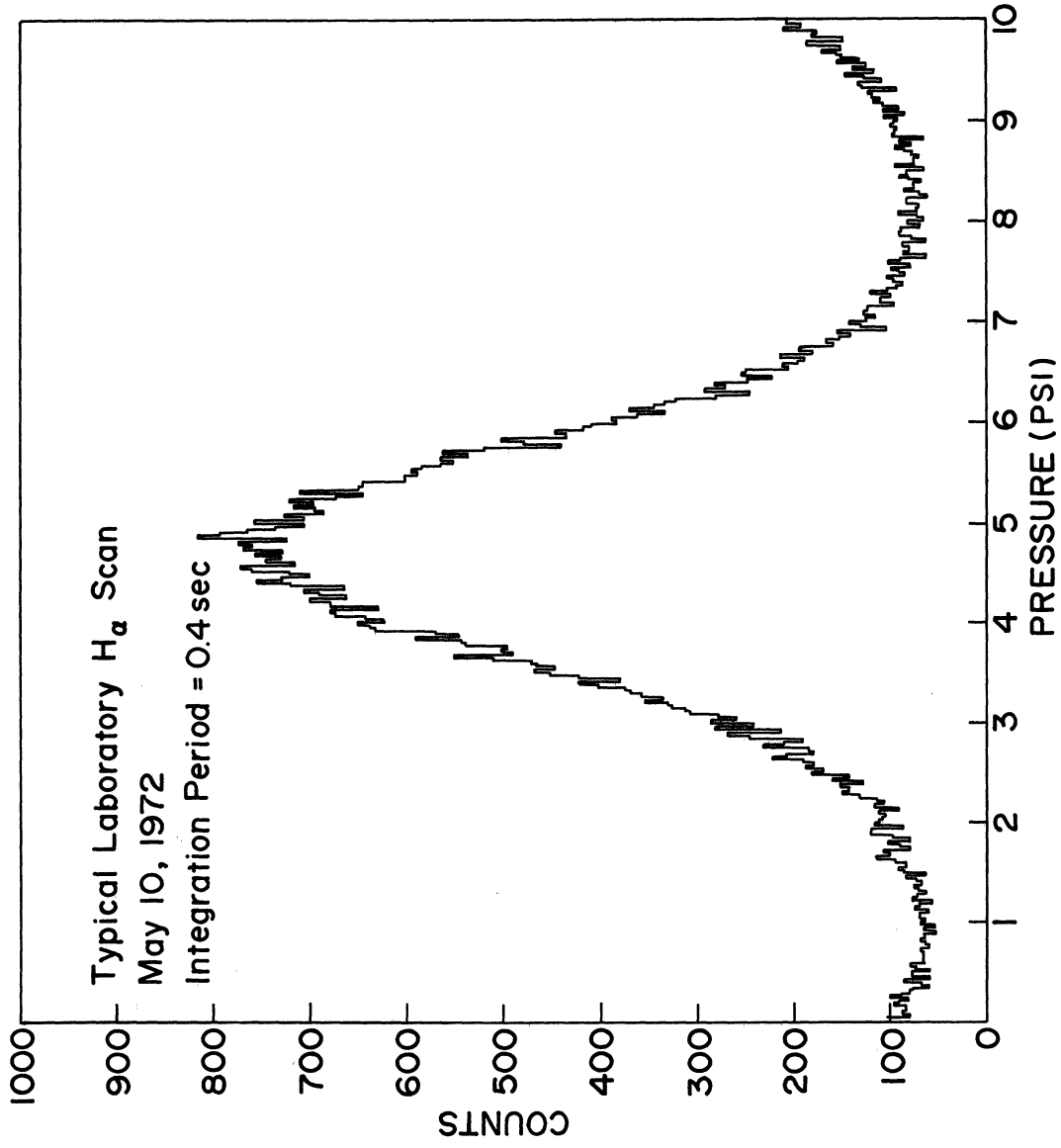

Fig. 21. Typical laboratory hydrogen lamp H_α fringe of May 10, 1972.

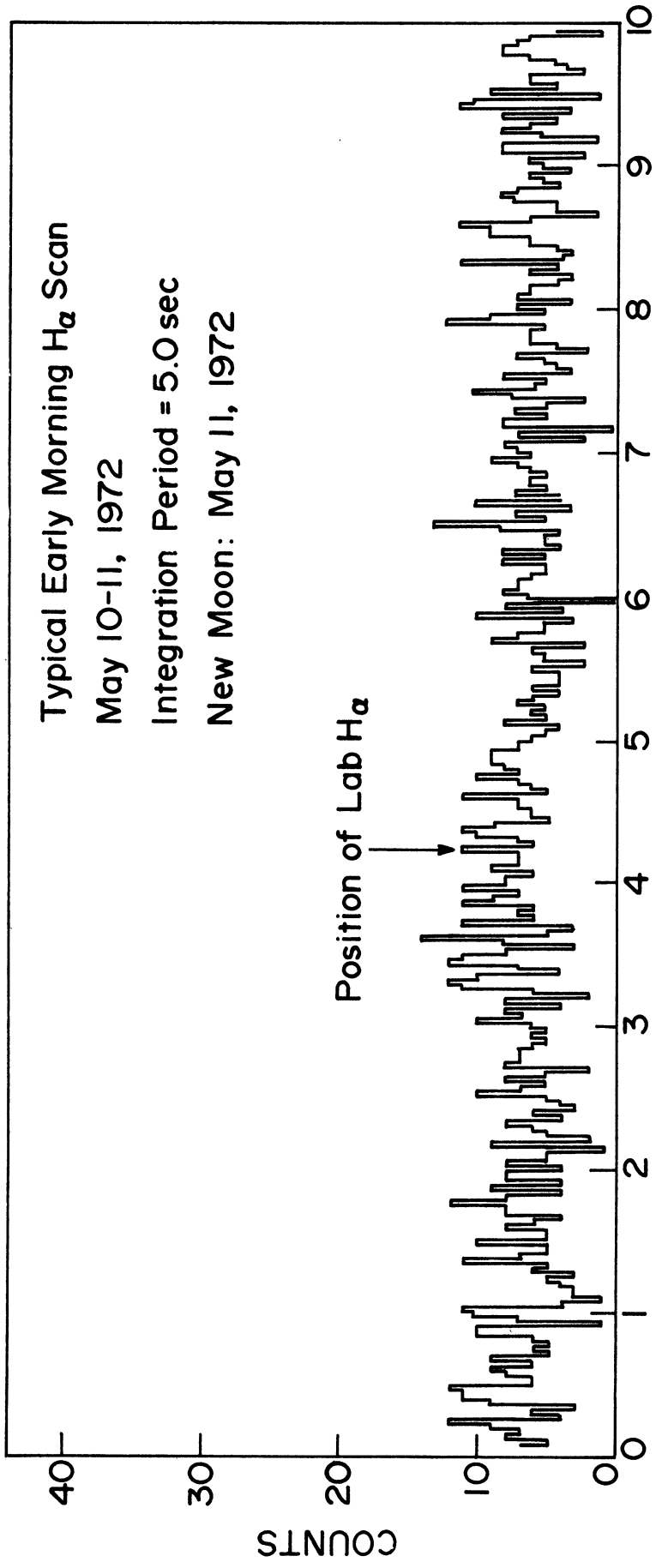

Fig. 22. Typical May 10-11, 1972 early morning Hα scan with integration period = 5 sec. In this figure, Lab Hα is the expected position of the geocoronal Hα deduced from the laboratory hydrogen lamp Hα.

latitude = 42.2°N, longitude = 83.7°W - geographic). Only the data gathered on the night of October 12-13, 1972 were meaningful due to extremely poor sky conditions and a malfunction in the data recording unit on all other nights.

5.5 DATA REDUCTION

5.5.1 NOISE-FILTERING

The Fabry-Perot interferometer used in this study has a low efficiency since high resolution could be achieved only at the expense of luminosity. Moreover, the geocoronal H_α signal is also extremely weak. For weak emissions, the random noise resulting from fluctuations in the photomultiplier tube becomes a significant part of the signal because the noise varies as the square root of the signal. Several researchers in the past (Chabbal, 1953; Turgeon and Shepherd, 1962; Hernandez, 1966; Larson and Andrew, 1967; and Shepherd, 1967) have devised schemes to retrieve Doppler temperature from the measured Fabry-Perot interference fringe data. However, these techniques require (or work best with) noise-free data; and are also unsuitable for handling large amounts of data (Hays and Roble, 1971). In this study, the maximum measured geocoronal H_α intensity ($\simeq$ 10R) amounts to a photomultiplier count rate of $\simeq$ 0.5 count$\cdot$ sec^{-1}, whereas the dark current of the cooled photomultiplier tube is about 1 to 2 counts $\cdot$ sec^{-1}; thus the situation of noise-free fringes does not exist.

Recently, Hays and Roble (1971) have worked out a fairly general data reduction technique which successfully retrieves the Doppler information of the source of emission from a noisy fringe. The technique is based on the Fourier analysis of the data and takes

advantage of the nature of periodicity peculiar to the noise and to the signal. The noise due to statistical fluctuations in the photomultiplier tube is spread over a large frequency range and can be reduced significantly by taking a finite and small number of Fourier coefficients of the data over a free spectral range, thus leaving only the fundamental frequencies which contribute to the emission signal. One can use only the Fourier cosine (or sine) transform provided the transform is taken from fringe peak to fringe peak. In the present investigation, however, it was seldom possible to gather data from fringe peak to fringe peak due to limitations on the pressure gauge. The requirement of fringe peak to fringe peak calculation is removed by taking both the cosine and the sine transforms (which can begin anywhere in the free-spectral range) and finding their resultant. The reader is referred to Hays and Roble (1971) for the details of the Fourier analysis of the data.

5.5.2 DOPPLER TEMPERATURE

In this study, the H_α fringe profiles reconstructed from the Fourier coefficients of the data were found to contain a number of undesired 'lines' in the wings of the fringe profiles. It is believed that these 'lines' in the wings represent a number of hydroxyl lines of the OH(6-1) band which might have transmitted through the wings of the H_α filter (see Sec. 4.5.4 for the critical OH(6-1) lines and the filter specifications). None of the three critical hydroxyl lines (Sec. 4.5.4) is removed from the H_α line center by an integral multiple of a free-spectral range, therefore their appearance is strictly in the wings of the fringe profile. The question whether anyone of these lines in the wings could be interplanetary H_α is discussed in the

following chapter and it is concluded that this is most probably not the case. A technique of 'half width and steep-slope matching' was used for retrieving the geocoronal Doppler temperature from the reduced fringe. The reduced fringe was further analyzed in the manner to be described next.

The sketches in Fig. 23 illustrate one free-spectral range of a 'clean' H_α fringe profile (dashed curve), and, one with hydroxyl superposition (solid line curve) which is similar to the observed fringe. In the actual observed fringe profile, however, there are fortunately regions in the wings where the OH signals are apparently non-existent or small. In that case the 'lowest level' in the entire free-spectral range should be a fairly good representation of the continuum background level. Due to inadequate facilities, a separate measurement of the background level could not be made in these observations. Therefore, the lowest level in the entire free-spectral range was assumed to be the closest measure to the actual continuum background level. Normalized profiles of the three critical hydroxyl lines of the OH(6-1) band (Sec. 4.5.4)were generated theoretically for the 200-300^{o}K temperature range. The theoretical OH profiles were then removed from the reduced fringe after adjusting their amplitudes and the positions somewhat. Such an adjustment was necessitated by the fact that the exact wavelengths (to at least the third decimal place) and intensities of these hydroxyl lines are not known accurately. The exercise of removing the hydroxyl lines served a two-fold purpose, (i) to determine the portion of the fringe best suited for retrieval of the Doppler temperature, and (ii) to check if any detectable amount of interplanetary H_α was present.

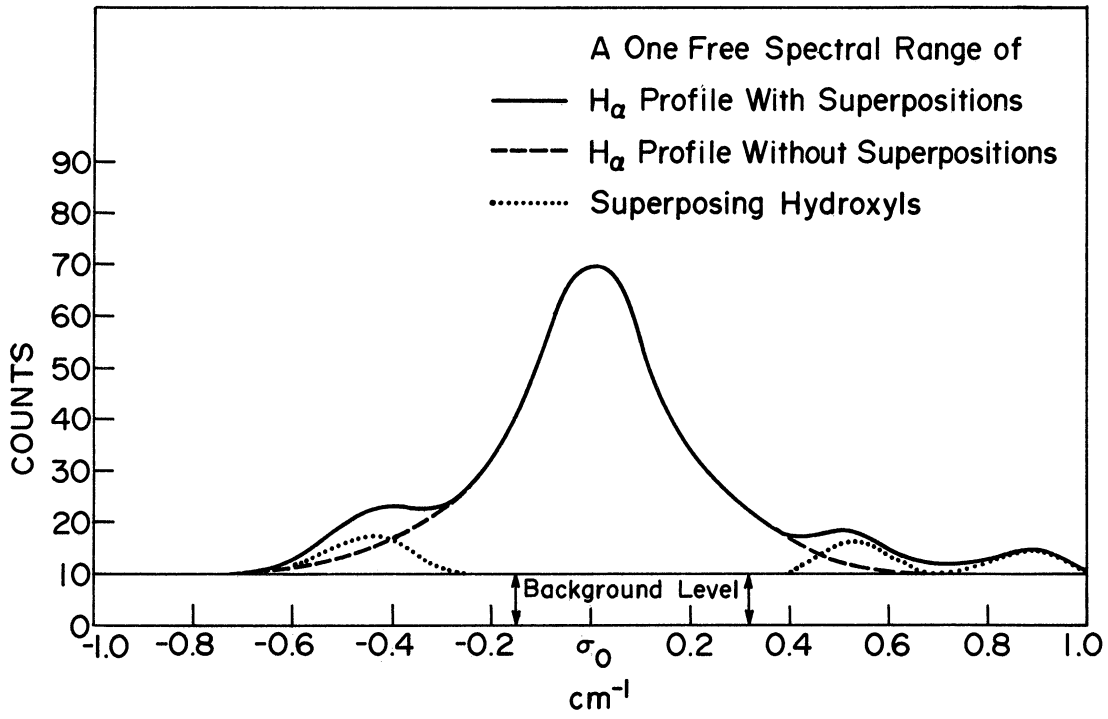

Fig. 23. Sketch illustrating the effect of the superposition of three hydroxyl fringes on a 'clean' H_α fringe.

It is apparent from a number of fringe profiles presented in the next chapter, that the 'steep-slope' to the right of the geocoronal H_α peak (the principal maximum) is practically free of any superpositions. Therefore, this 'steep-slope' was used in the final determination of the geocoronal temperature in the following manner.

A rough estimate of the temperature was made by measuring the full width of the profile at half its maximum height above the 'lowest level', and comparing it against the half widths of the H_α profiles theoretically simulated for a range of temperatures and the instrument parameters particular to the night of the observation (see Fig. 24 for one such simulation). Having thus estimated roughly the Doppler temperature, the final determination of the bounds between which the geocoronal temperature lies was made by matching the 'steep-slope' of the observed fringe to that of a number of theoretically simulated H_α profiles. The Doppler temperatures corresponding to the theoretical profiles which fall most closely on either side of the 'steep-slope' of the observed fringe determine the bounds on the range in which the retrieved geocoronal temperature lies.

The instrument finesses used in the theoretical simulation of the H_α and the OH line profiles for a particular night of observation were derived from the He-Ne laser calibrations performed, usually, prior to, during and at the end of that night.

5.5.3 INTENSITY

The intensity of the H_α emission was estimated analytically by calculating the count rate at the peak of emission (above the 'lowest level') and relating it to the intensity of the source in Rayleighs (see Appendix F for details). This technique was adopted

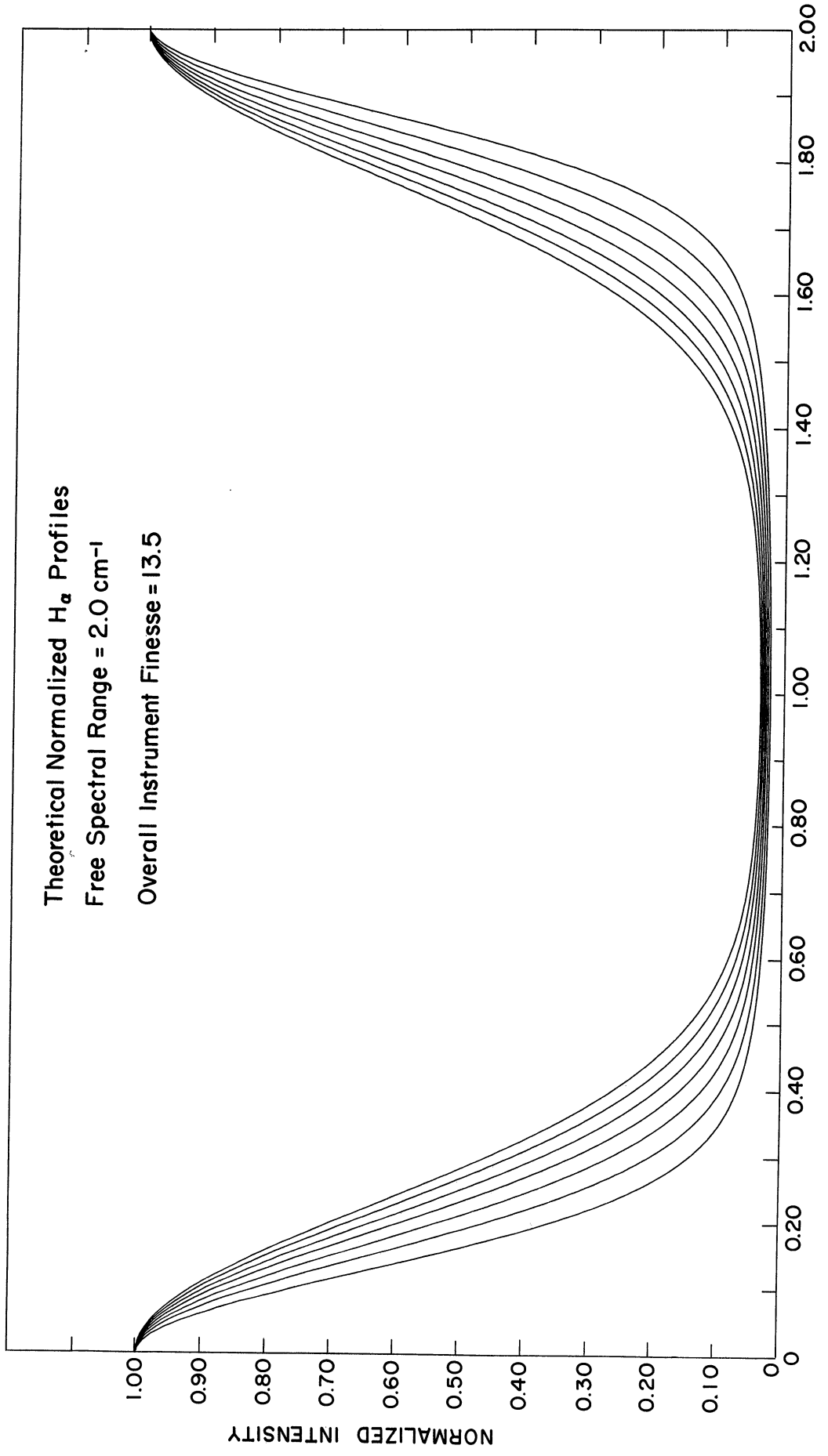

Fig. 24. Theoretically simulated H_α profiles with Doppler Temperatures ranging from 500 to 2000°K in steps of 250°K.

since at the time of observations, a calibrated low brightness source was not available. However, the low brightness source was calibrated later and the theoretical figure for estimating the intensity was verified.

5.5.4 DOPPLER SHIFTS

In order to determine the Doppler shift of the emission, one must know the laboratory position of the line and a relationship between the pressure of the scanning gas and the wavelength. The laboratory position of the geocoronal H_α line was determined using a hydrogen lamp source (see Appendix A for details). The pressure-wavelength relationship was obtained by determining the free-spectral range at a given wavelength both in terms of angstrom and the pressure of the scanning gas. The free-spectral range in $\mathring{A}$ is given by the following relation.

$$\Delta\lambda_{FSR} = \lambda_o^2/2t$$

where λ_o = wavelength of emission in $\mathring{A}$

t = spacing between the Fabry-Perot plates in $\mathring{A}$

At the H_α wavelength (6562.8 $\mathring{A}$), the free-spectral range in terms of $\mathring{A}$ was calculated to be 0.8614 $\mathring{A}$, and its measured value was 7.528 PSI (N_2). Thus, it was found that

$$1 \text{ PSI } (N_2) = 0.1144 \mathring{A}$$

This figure was verified by calculating and then checking the relationship at the He-Ne laser wavelength as well.

Any macroscopic velocity, v of the emitting atoms is then related to the Doppler shift, $\Delta\lambda$, by the following relation

$$v = -\frac{c}{\lambda_o}\Delta\lambda$$

where, c is the velocity of light

Due to the limitations on both the micrometer needle valve which regulates the flow of the scanning gas, and the sensitivity of the pressure tranducer; the reliability of the pressure measuring system was within $\sim$0.0375 PSI (N_2) which corresponds to about 0.0043Å or a velocity of $\sim$ 200 meters$\cdot$sec^{-1} at the H_α wavelength.

5.5.5 CONSIDERATIONS ON THE NUMBER OF DATA POINTS (INTEGRATION PERIOD) AND THE ADDITION OF THE FRINGES

The effectiveness of the noise filtering technique discussed in Sec. 5.5.1 also depends upon the total number of samples (data points) in a free-spectral range. For a minimum error between the profile reconstructed from the Fourier coefficients and the theoretically generated profile of the fringe, the number of data points over a free spectral range must exceed 100 (Hays & Roble, 1971). In this study, usually 175 to 200 samples were taken over a free-spectral range. Due to a very weak geocoronal H_α signal, it was necessary to add a large number of fringes to improve the signal to noise ratio. The addition of the fringes was accomplished through their Fourier coefficients. A direct addition of the data was prevented because of two reasons, namely

(i) it was not possible to always begin the scan exactly at the same pressure, and

(ii) the number of samples over a free-spectral range usually varied by one to two from fringe to fringe; such variation resulted from the lack of an absolutely linear rate of flow of the scanning gas.

The Doppler temperature and intensity retrieved from the addition

of fringes represents an average over the duration of the fringes-added.

The results of observations and discussions are presented in the following chapter.

CHAPTER VI

RESULTS OF OBSERVATIONS AND DISCUSSIONS

6.1 INTRODUCTION

The results of the observations made in December 1971, May 1972 and October 1972 are presented in this chapter. Whenever feasible; the results are compared with other measurements and theoretical predictions. The question whether the measured geocoronal hydrogen temperatures do indeed represent the exospheric value is discussed by considering the energy exchange in elastic collisions between the hydrogen and oxygen atoms below the exobase. Finally, some semiquantitative information retrieved from a few isolated galactic H_α scans made in December 1971 is given.

6.2 RESULTS OF THE GEOCORONAL H_α MEASUREMENTS

The analyzed data for a number of observation nights are presented in a series of figures (Fig. 25 through Fig. 39). The reduced data for a given night are shown in a sequence of three figures- the first figure of each sequence shows the fringe reconstructed from its Fourier coefficients (solid line curve), the removed hydroxyl lines (dotted curves) and the 'clean' H_α fringe (dashed curve) obtained on subtracting the hydroxyl lines from the reconstructed fringe; the overlay of a number of theoretically simulated H_α profiles on the 'clean' H_α fringe of the previous figure is shown in the second figure; and finally an enlarged view of the 'steep slope' to the right of the fringe peak in the second figure is shown in the third figure of the sequence. The features of the December 17-18, 1971 and December 18-19, 1971 data, which were collected under identical illumination geometry, were found to be quite similar so that the curves presented

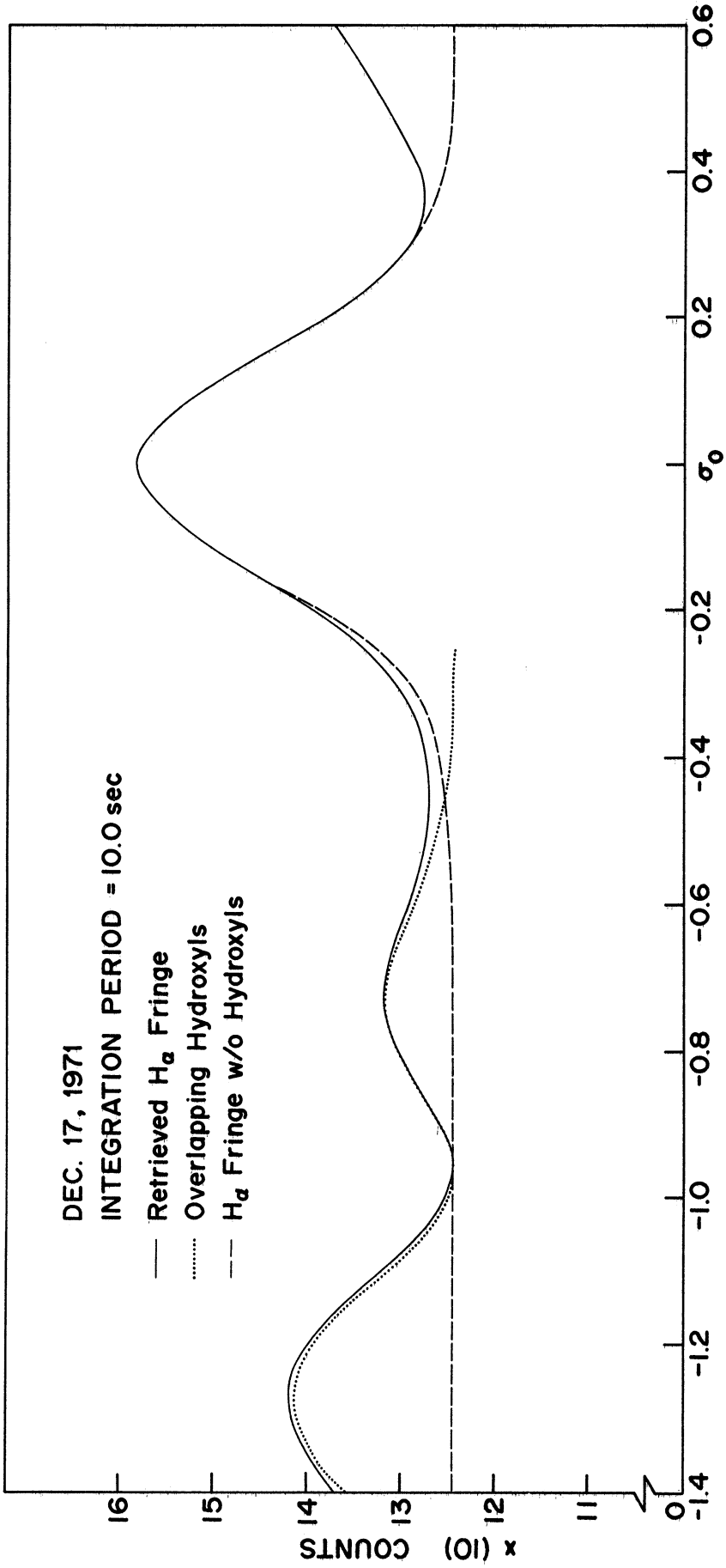

Fig. 25. A free spectral range (2.0 cm^{-1}) of an Hα fringe retrieved from the Fourier coefficients of December 17-18, 1971 addition. The solid line curve is the sum of the dashed and the dotted curves.

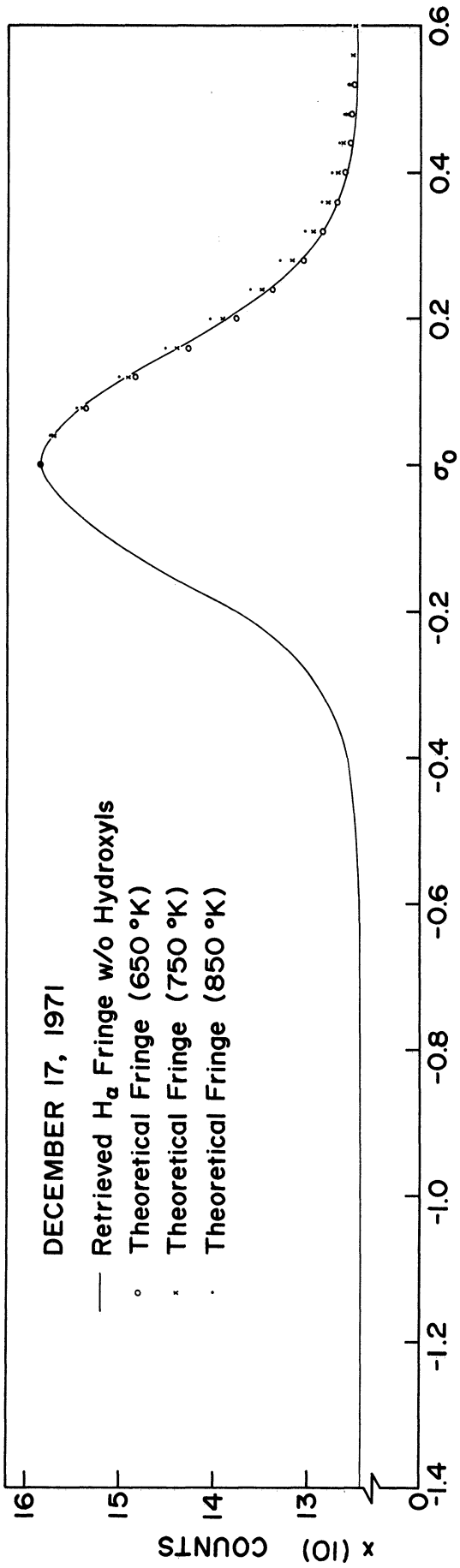

Fig. 26. Theoretically simulated H_α fringe profiles for a range of temperatures overlaid on the 'clean' H_α fringe of Fig. 25.

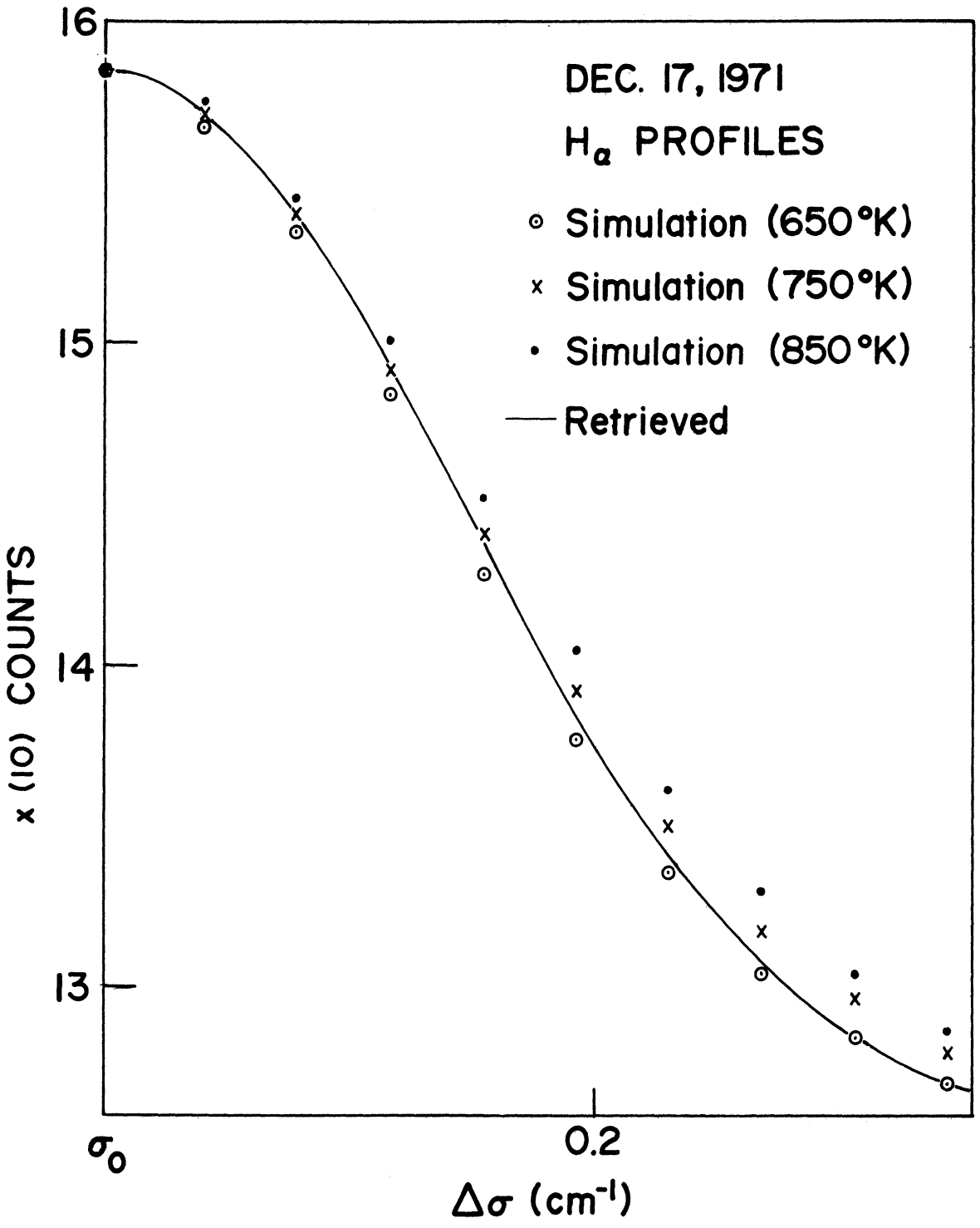

Fig. 27. An enlarged view of a segment of the fringe shown in Fig. 26. The standard deviation of the retrieved temperature is $\sim 195^{\circ}$K.

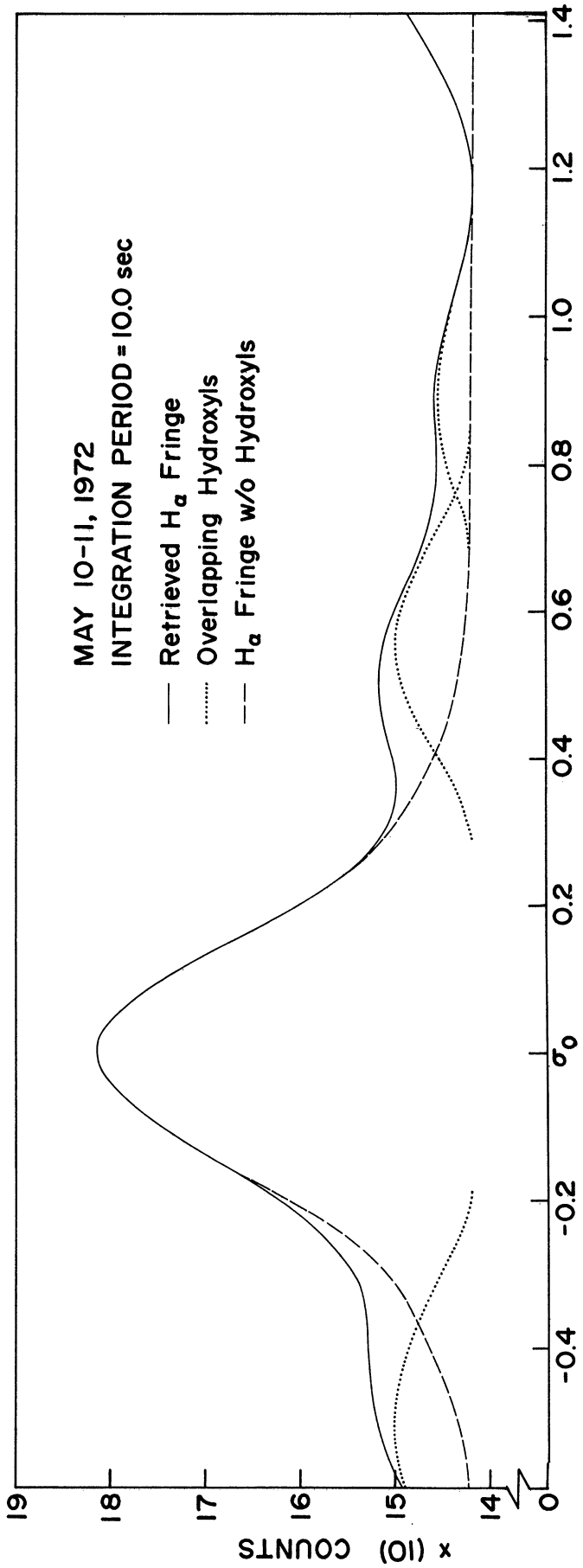

Fig. 28. A free spectral range (2.0 cm^{-1}) of an H_α fringe retrieved from the Fourier coefficients of May 10-11, 1972 addition. The solid line curve is the sum of the dashed and the dotted curves.

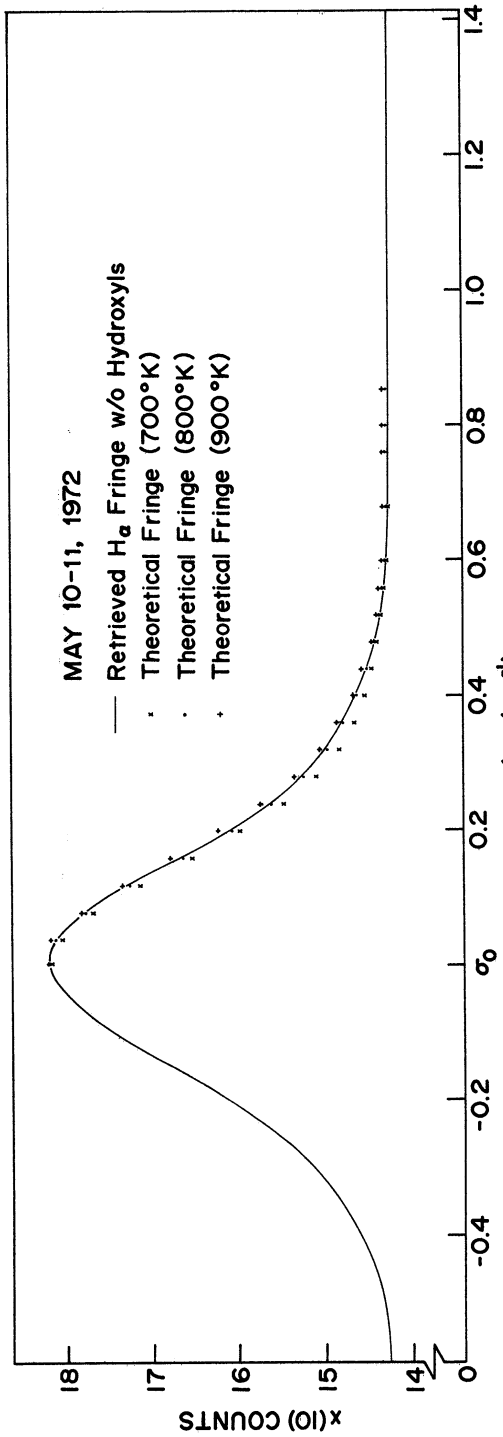

Fig. 29. Theoretically simulated H_α fringe profiles for a range of temperatures overlaid on the 'clean' H_α fringe of Fig. 28.

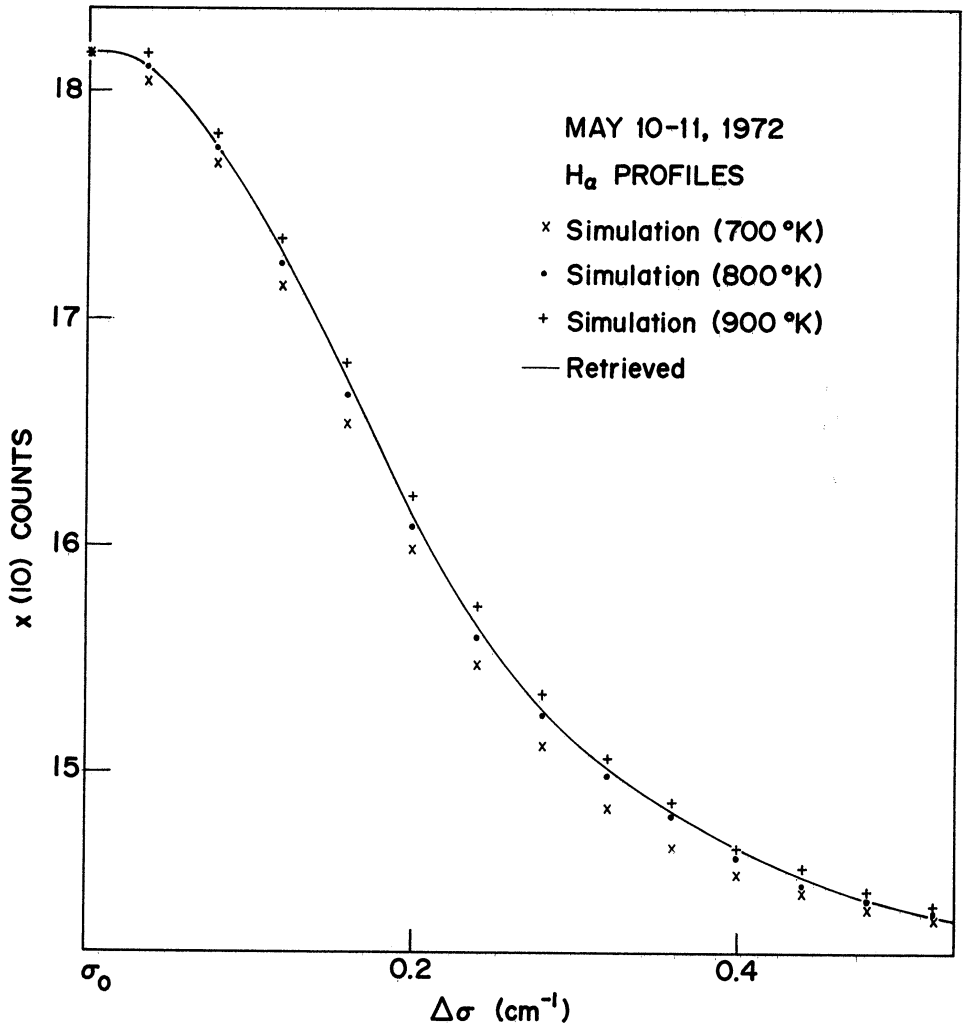

Fig. 30. An enlarged view of a segment of the fringe shown in Fig. 29. The standard deviation of the retrieved temperature is $\sim 210\,^{\circ}K$.

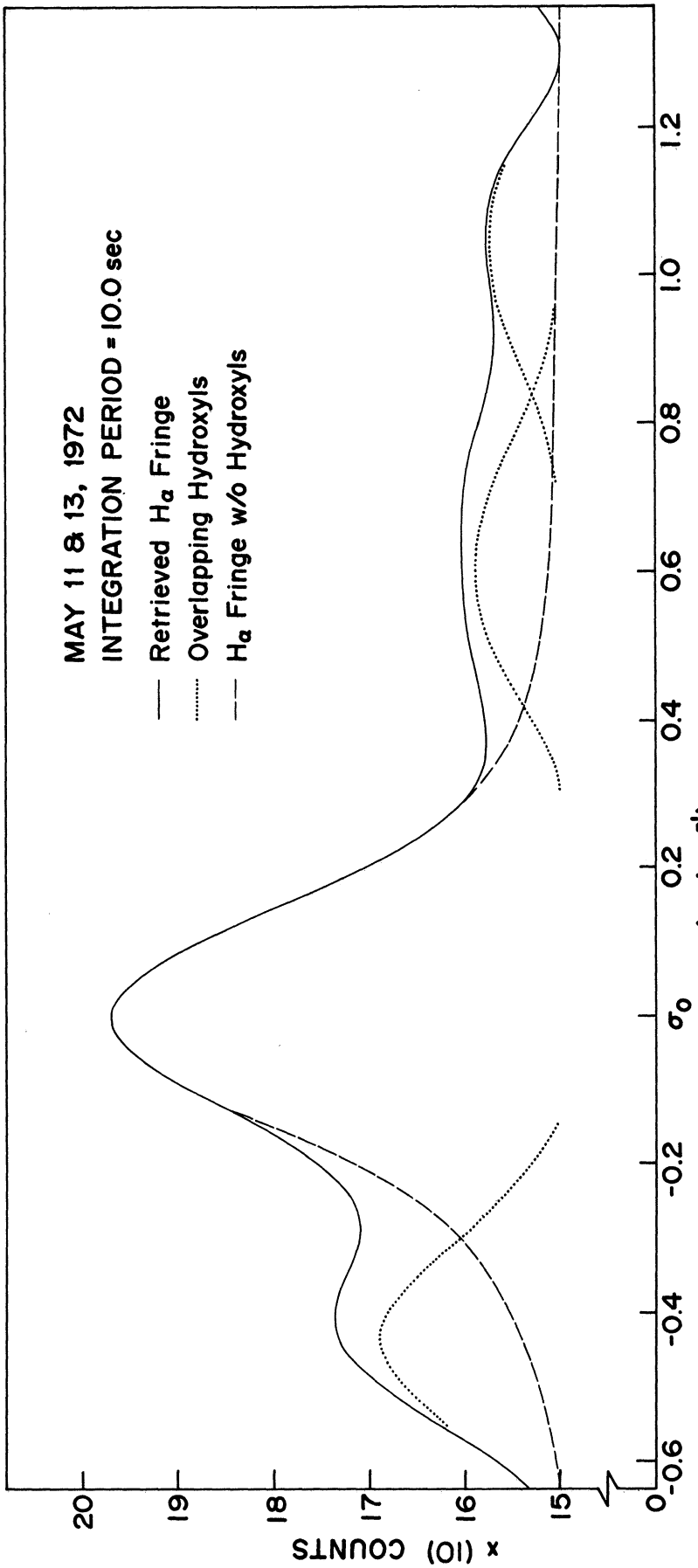

Fig. 31. A free spectral range (2.0 cm^{-1}) of an H_α fringe retrieved from the Fourier coefficients of May 11+13, 1972 addition. The solid line curve is the sum of the dashed and the dotted curves.

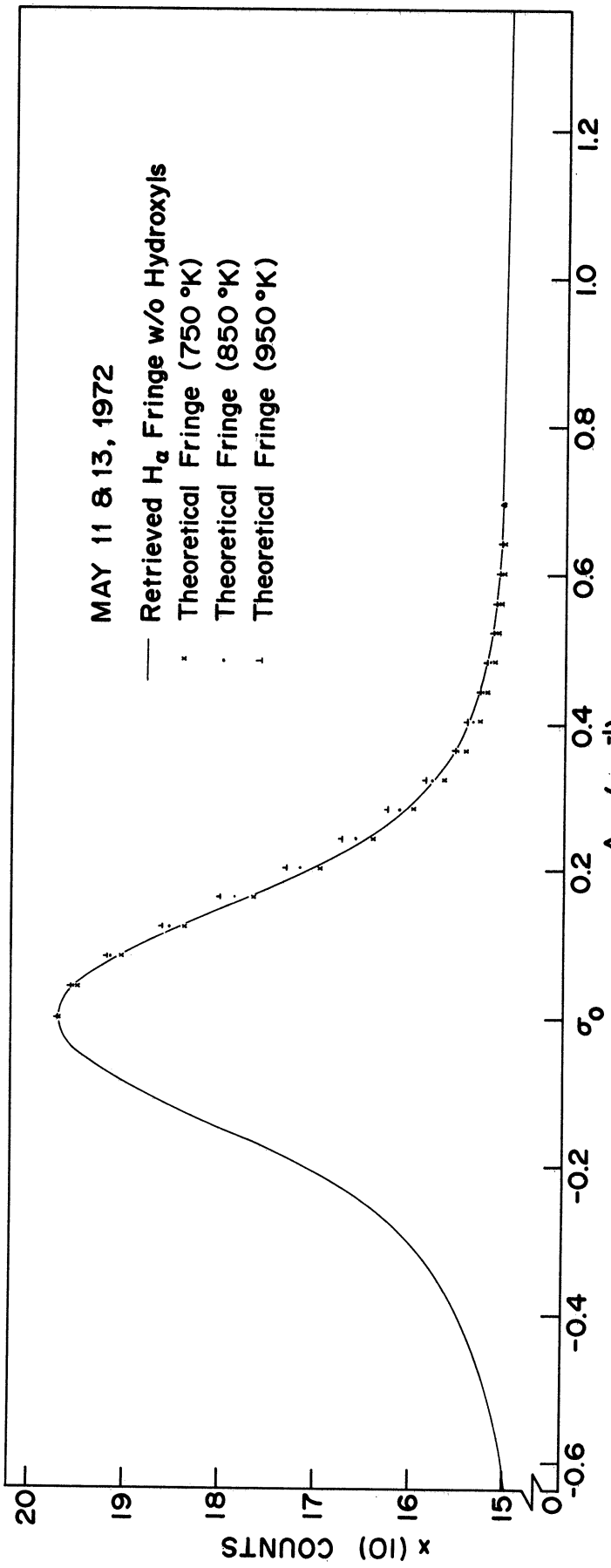

Fig. 32. Theoretically simulated H_α fringe profiles for a range of temperatures overlaid on the 'clean' H_α fringe of Fig. 31.

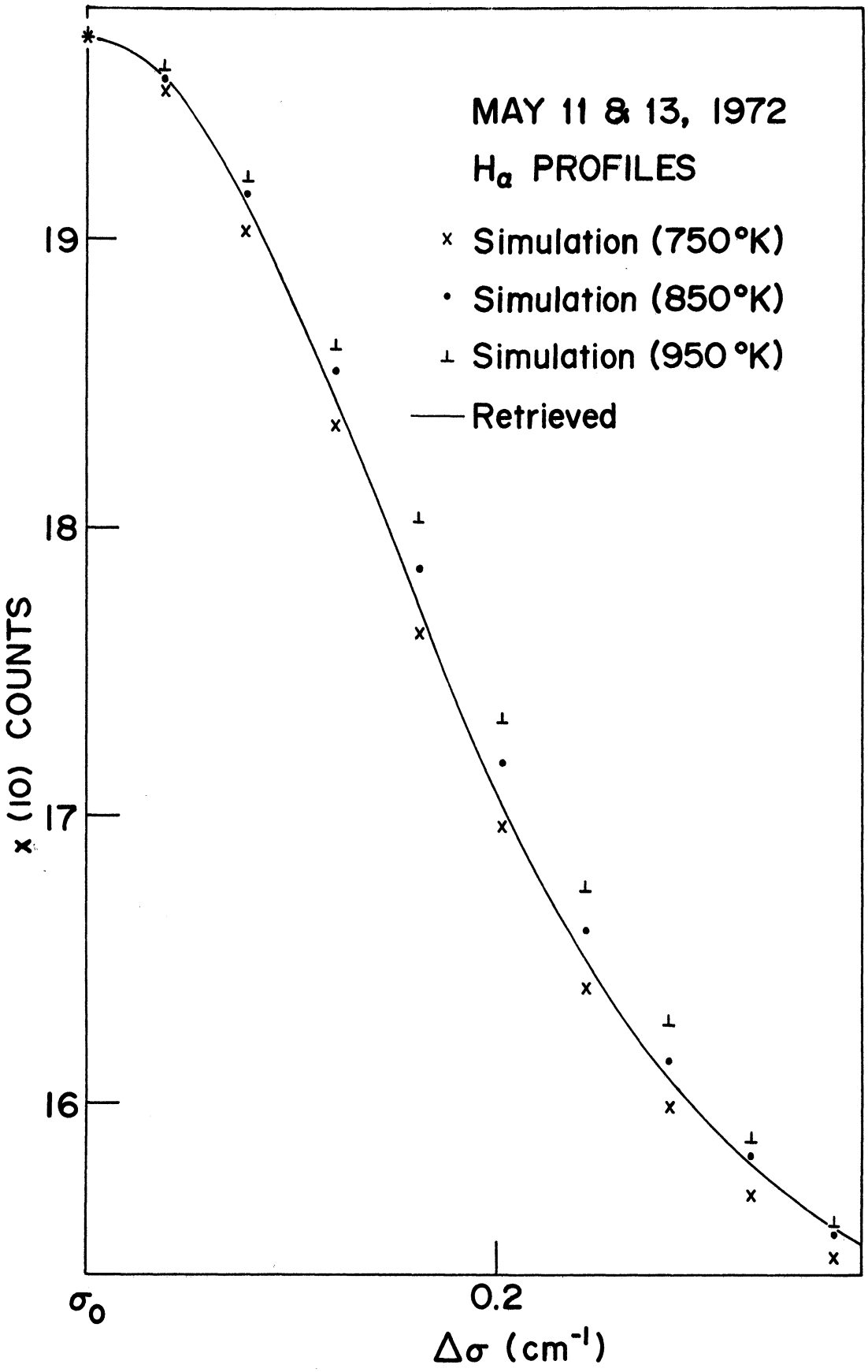

Fig. 33. An enlarged view of a segment of the fringe shown in Fig. 32. Standard deviation of the retrieved temperature is ~170 °K.

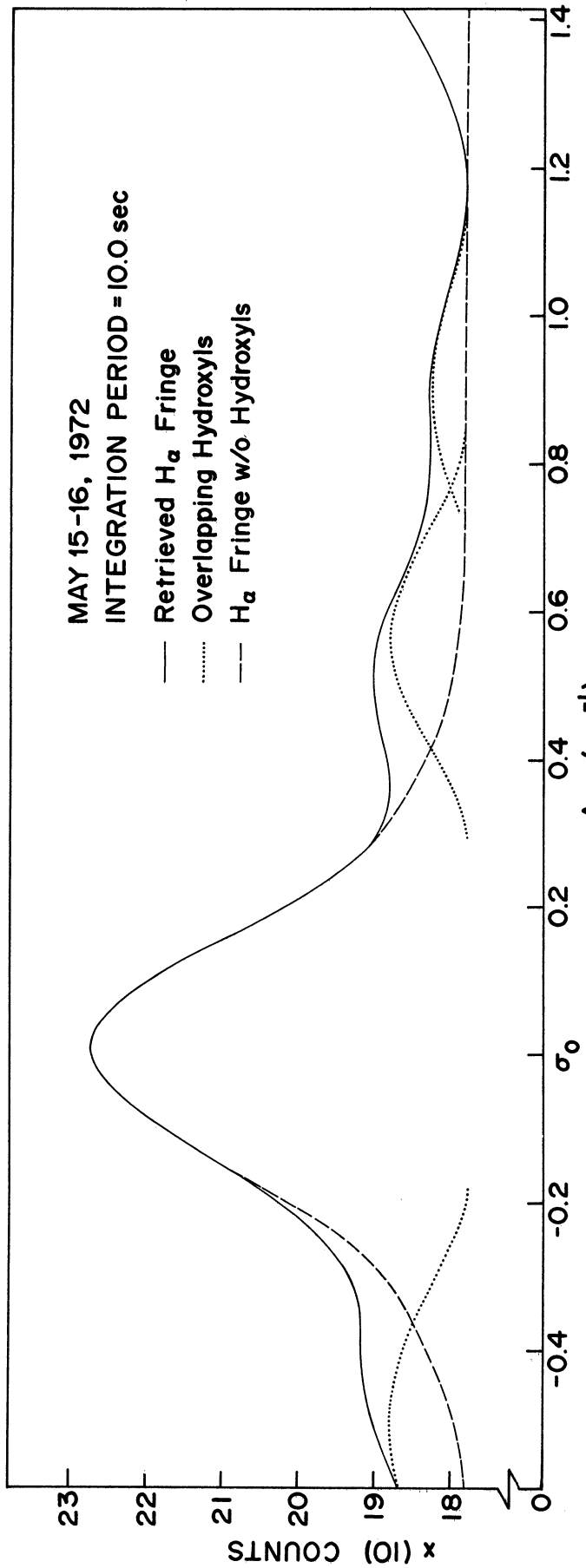

Fig. 34. A free spectral range (2.0 cm^{-1}) of an H_α fringe retrieved from the Fourier coefficients of May 15-16, 1972 addition. The solid line curve is the sum of the dashed and the dotted curves.

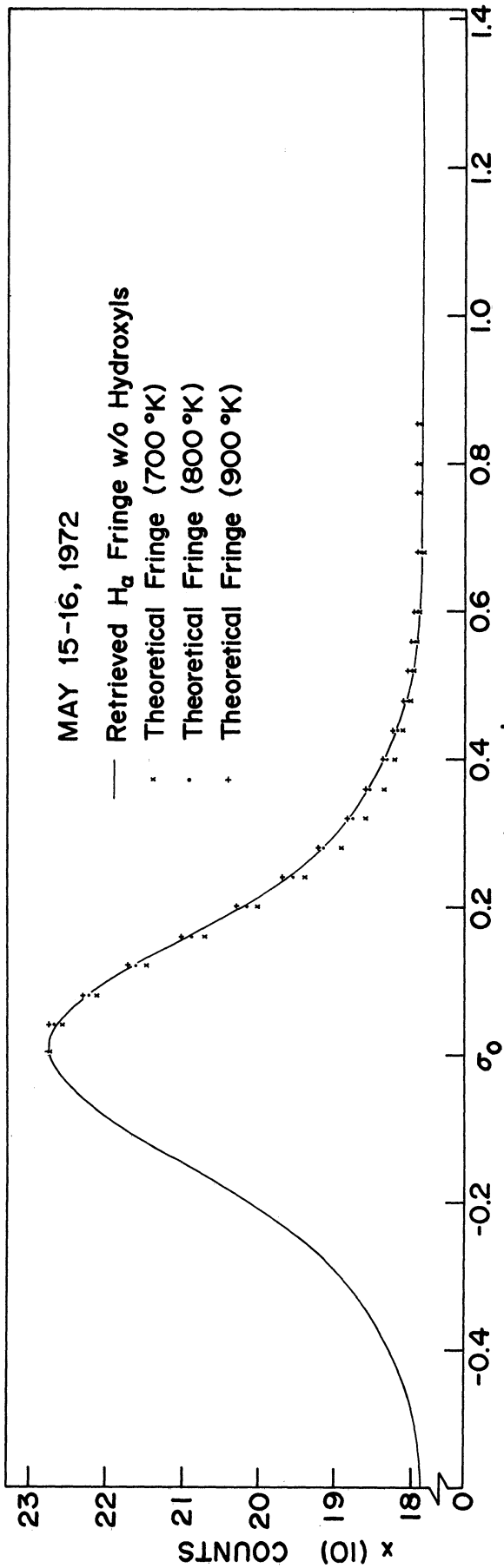

Fig. 35. Theoretically simulated H_α fringe porfiles for a range of temperatures overlaid on the 'clean' H_α fringe of Fig. 34.

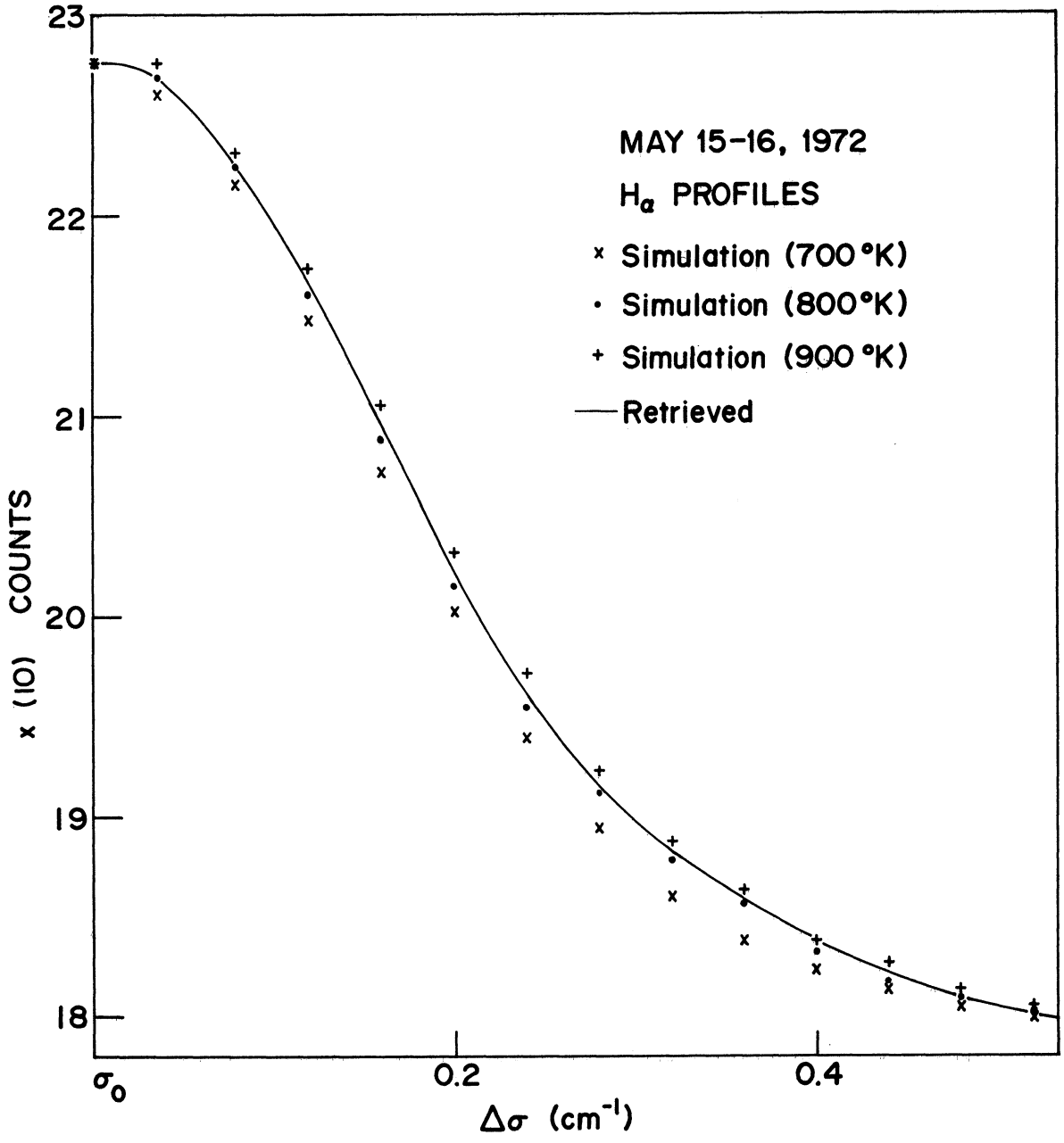

Fig. 36. An enlarged view of a segment of the fringe shown in Fig. 35. The standard deviation of the retrieved temperature is $\sim$200 ^{o}K.

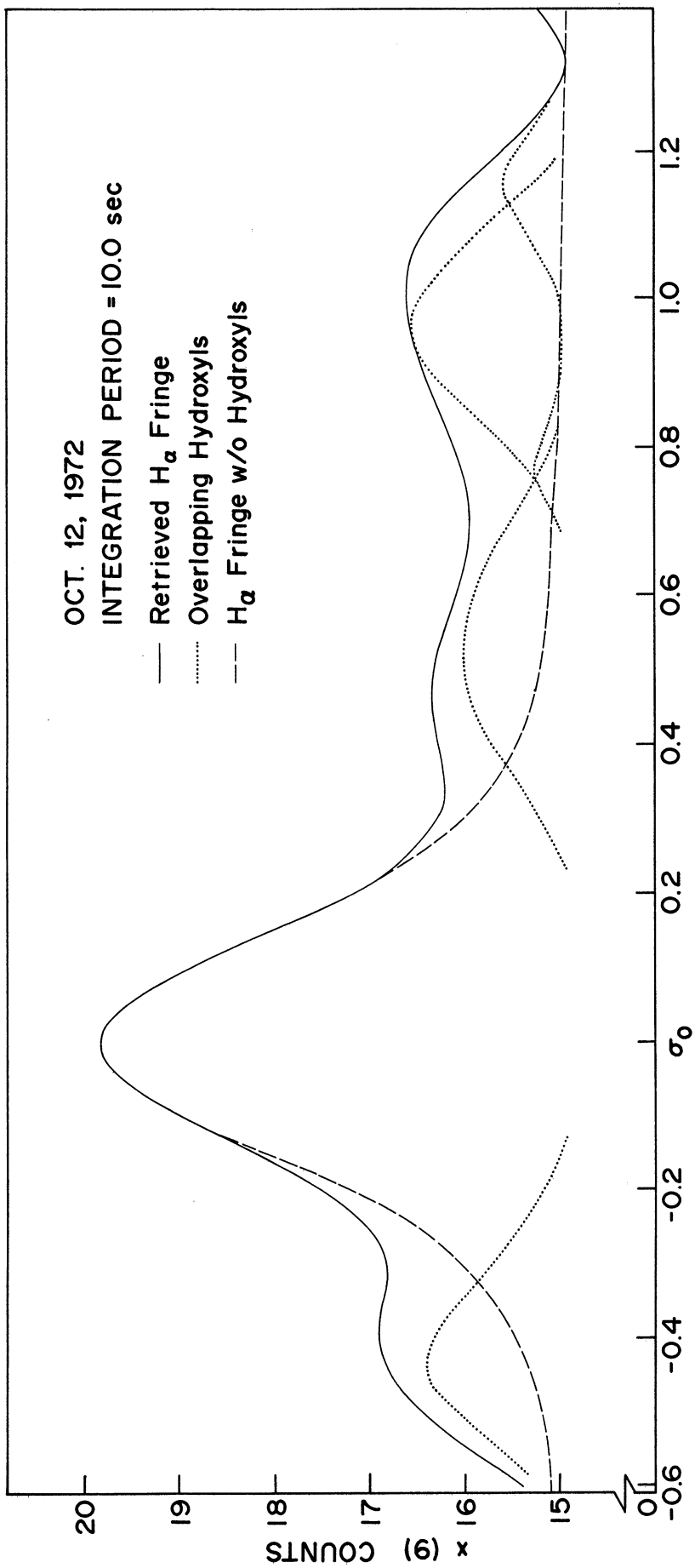

Fig. 37. A free-spectral range (2.0 cm^{-1}) of an H_α fringe retrieved from the Fourier coefficients of October 12, 1972 addition. The solid line curve is the sum of the dashed and the dotted curves.

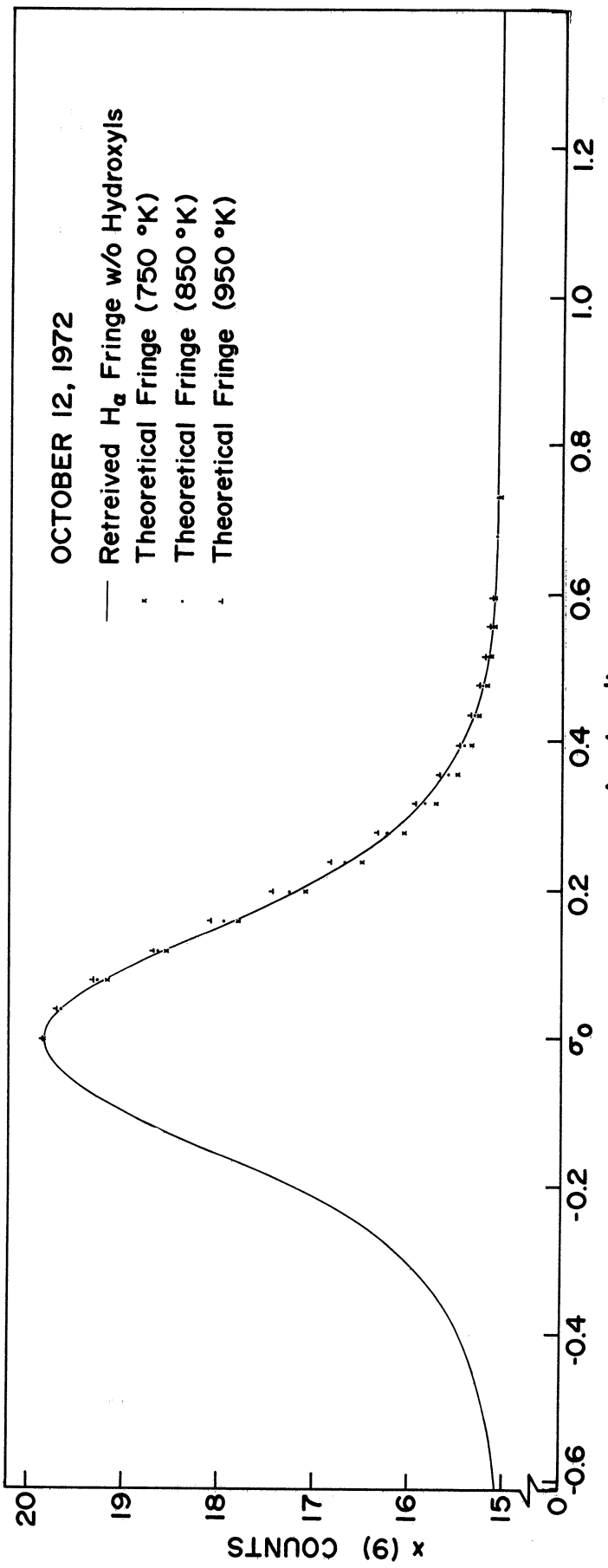

Fig. 38. Theoretically simulated H_α fringe profiles for a range of temperatures overlaid on the 'clean' H_α fringe of Fig. 37.

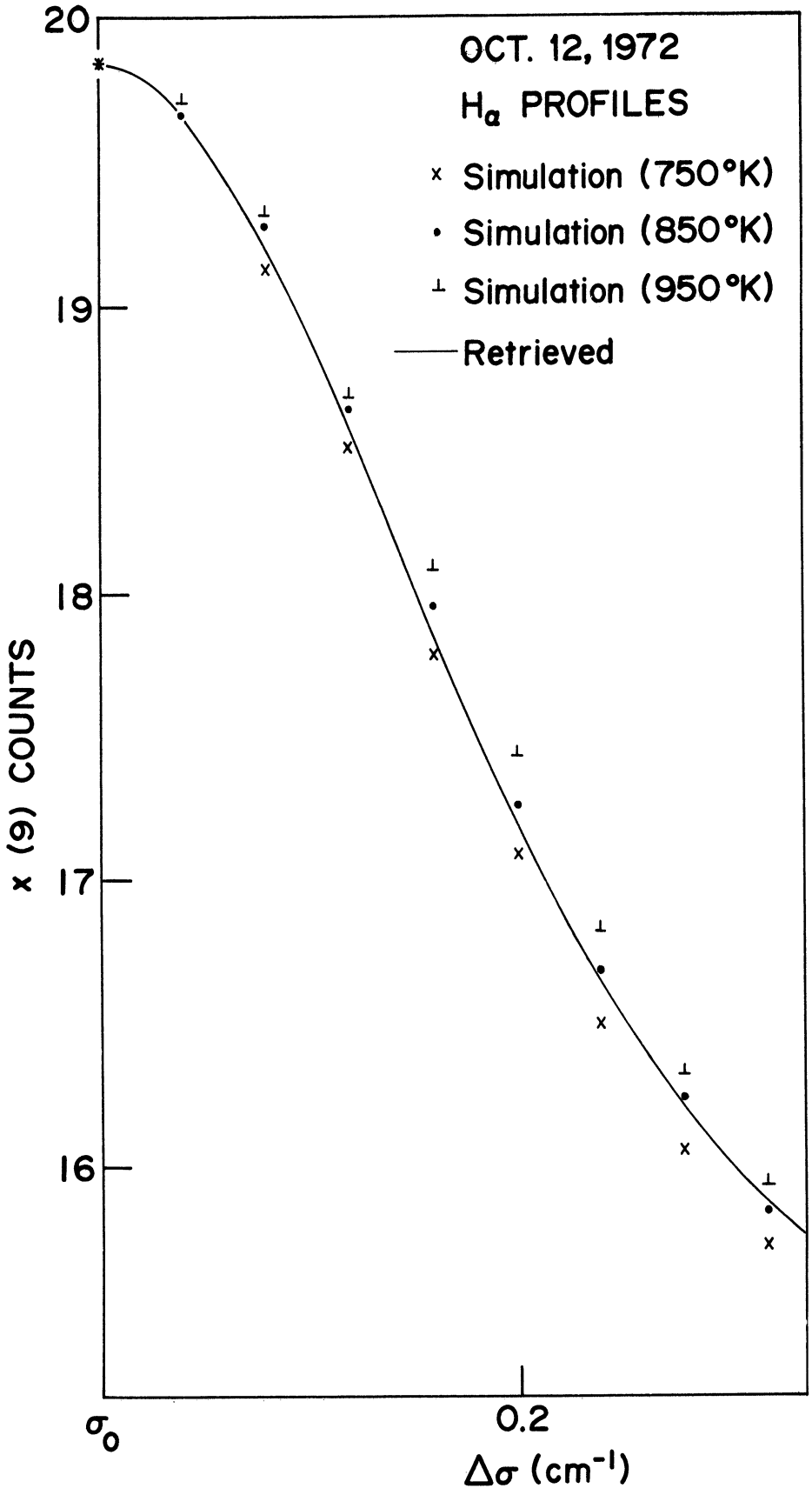

Fig. 39. An enlarged view of a segment of the fringe shown in Fig. 38. The standard deviation of the retrieved temperature is ~ 175 °K.

for December 17-18, 1971 (Fig. 25, 26 and 27) represent the behavior for both of these nights. The illumination geometry and the number of fringes added on the nights of May 10-11, 1972 and May 15-16, 1972 were the same, and the curves were also found to be nearly identical (Figs. 28, 29, 30; and Figs. 34, 35, 36); no apparent sporadic variations in the H_α intensity and temperature were noticed. Only the data gathered over the first part of the May 11-12, 1972 and May 13-14, 1972 observation nights were good, and since the illumination geometry for this period was the same, these data were added through their Fourier coefficients; the curves for the combined data are shown in Figs.31, 32 and 33. The October 12-13, 1972 data (Figs. 37, 38, 39) were collected under poor sky conditions, therefore one notices a few small amplitude signals besides the three critical hydroxyl lines in the wings of the fringe profile (Fig. 37). The common characteristics of the reduced data (see the first curve of each of the abovementioned nights) are as follows:

(i) Each curve is obtained by adding the Fourier coefficients of all the fringes obtained during a given night.

(ii) Each curve represents one free-spectral range (2.0 cm^{-1}) of the fringe, with the principal maximum (at σ_0) at the expected position of the geocoronal H_α line deduced from the laboratory hydrogen lamp calibration. The first point of the fringe reconstructed from its Fourier coefficients is at the same height as the last point which marks the beginning of a new free-spectral range.

(iii) The hydroxyl lines in the May and October, 1972 observations, which were averaged over one, two and sometimes three tracking directions, have approximately the same positions relative to σ_0 in the

free-spectral range. A slight adjustment in their positions and intensities was necessitated by the lack of precise knowledge of these parameters. The December 1971 observations were carried out with viewing mirrors continuously tracking different parts of the celestrial sphere. Therefore, there was a possibility of some galactic or stellar contamination whose superposition on the hydroxyl lines would render the determination of the exact location of the OH signals in the free-spectral range quite difficult. This is what seems to be the case since the OH lines in the December, 1971 appear to have a somewhat different position in the free-spectral range than in the other observing periods.

(iv) The 'steep-slope' of the principal maximum is practically free of any superpositions out to about $(\sigma_0 + 0.25)$ cm^{-1}. Therefore, the enlarged view of the fringe (the third figure of each sequence) usually shows the portion to about $(\sigma_0 + 0.25)$ cm^{-1}.

The geocoronal hydrogen temperatures retrieved by matching the 'steep-slope' of the measured fringe against the theoretically simulated profiles, and the measured geocoronal H_α intensities for the various observing periods are presented in Table 8. A comparison of the measured temperatures against Jacchia's (1971) exospheric temperatures; and of the intensities against Tinsley and Meier's (1971) predictions is also given in Table 8.

6.3 DISCUSSION OF THE RESULTS

6.3.1 THE MEASURED GEOCORONAL H_α INTENSITIES

The measured geocoronal H_α intensities were found to be in general agreement with Tinsley and Meier's (1971) values. The greatest discrepancy is between the October 12-13, 1972 measured

TABLE 8.

Information Retrieved from the Geocoronal H_α Doppler Profile Measurements

Observation Nights	H_α Intensity (Rayleighs)			Doppler Temperature (^oK)		
	Present Measurements	Tinsley and Meier's (1971)* Measurements	Tinsley and Meier's (1971)* Calculations	Present Measurements (mean value)	Jacchia's Exospheric Value	$\overline{\Delta T}$**
Dec. 17-18, 1971	6.6	9.0	8.0	700	900	195
Dec. 18-19, 1971	9.0	9.2	8.5	800	885	180
May 10-11, 1972	8.0	7.0	7.5	850	915	210
May 11-12, 1972 + May 13-14, 1972	9.7	6.0	6.5	800	940	170
May 15-16, 1972	9.8	7.5	8.0	850	950	200
Oct. 12-13, 1972	9.7	5.0	5.0	800	850	175

Notes:

*Comparison of the present measurements is made against Tinsley and Meier's (1971) compilations for the 1966 level of the solar activity with 900°K exospheric temperature, and approximately same geometry of illumination.

**$\overline{\Delta T}$ represents the standard deviation of the Doppler temperatures retrieved from the present measurements. $\overline{\Delta T}$ was computed in the manner described by Hays and Roble (1971).

H_α intensity and Tinsley and Meier's (1971) prediction, which may have been caused by some sporadic variations in the solar L_β flux and atomic hydrogen content of the geocorona. Tinsley (1970) mentioned that such variations are not unlikely.

To the author's knowledge, no other observatories were involved in measuring the geocoronal H_α emission on the nights of the present observations. Therefore, an attempt was made to compare the results against earlier measurements made under similar conditions. Tinsley and Meier (1971) have corrected and compiled the H_α intensities measured by the various researchers in the USSR, France, Bolivia and the USA under various conditions of the geometry of illumination and over a large part of the last solar cycle. Tinsley and Meier (1971) have also calculated theoretically the expected geocoronal H_α intensities for a wide range of exospheric temperatures, geometries of illumination and levels of solar activity. The 1966 level of solar activity with 900°K exospheric temperature was found to describe the conditions of the present measurements most closely. Therefore, Tinsley and Meier's (1971) theoretical and observational curves for the 1966 level of solar activity with 900°K exospheric temperature were used for the comparison. The illumination geometry (i. e. solar depression angle, zenith angle of observation and the azimuth of observation relative to the sun's azimuth) corresponding to each fringe used in the addition was calculated and its intensity read off Tinsley and Meier's (1971) curves for the particular geometry. An average of the intensity of all the fringes used in the final addition then represents the best available experimental and theoretical comparison for the present measurements.It should be mentioned

here that such a comparison is only approximately valid since it is difficult to find other observations which were made under 'exactly' identical set of conditions. Moreover, there is probably some uncertainty (about 15 to 20%) in the estimates of the present H_α intensity measurements.

6.3.2 THE MEASURED HYDROGEN TEMPERATURES

The geocoronal temperatures retrieved from the Doppler profile measurements of the H_α line were found to be consistently lower than the exospheric temperatures predicted by Jacchia's (1971) model. Usually the discrepancy was about 50-150°K (Table 8). An attempt was also made to determine the difference between the evening, midnight and morning sectors. It was impossible to predict the evening to morning variation due to large uncertainties in the retrieved temperatures. Therefore, the retrieved temperatures and their comparisons given in Table 8 are averaged over the duration of the fringes added. The standard deviation of the mean retrieved temperature, shown in the last column of Table 8, was calculated using the error analysis technique of Hays and Roble(1971).

The question of whether the geocoronal hydrogen temperatures should indeed represent the exospheric values is decided by theoretically estimating the difference between the hydrogen and the oxygen temperatures at and below the exobase. For this purpose, the continuity equation for heat transfer between the hydrogen and oxygen atoms below the exobase is solved in the following manner.

The equation of heat transfer for the region of interest, where collisions between the hydrogen and oxygen atoms predominate, is:

$$\frac{\partial}{\partial z}\left(\lambda_0 \frac{\partial T_H}{\partial z}\right) = \frac{dU_H}{dt} \qquad (6\text{-}1)$$

where

λ_o = coefficient of thermal conductivity as a function of altitude z

T_H = Atomic hydrogen temperature

$\frac{du_H}{dt}$ = Average rate of energy exchange in elastic collisions between the hydrogen and oxygen atoms.

$\frac{du_H}{dt}$ can be expressed as a function of the average momentum transfer cross-section, densities of the two gases and the difference between their kinetic temperatures. Equation (6-1) can be transformed to the following form by using the hard sphere approximation of Desloge (1962) for $\frac{du_H}{dt}$, and applying some simplifications (see Appendix G for the details of the derivation).

$$\frac{\partial^2 T'}{\partial \xi^2} - \frac{\alpha}{\beta} T' = 0 \qquad (6\text{-}2)$$

where

$$T' = T_H - T_o$$

$$d\xi = -n_o(z)\,dz \qquad (6\text{-}3)$$

T_o = Atomic oxygen temperature

n_H and n_o = Atomic hydrogen and atomic oxygen number densities

and, α and β are constants (see Appendix G, Equation (G-4) for their definitions).

The solution of Equation (6-2) can be expressed in the following exponential form (see Appendix G for details of the derivation).

$$T' = T_H - T_O = -\frac{\mathcal{F}_{esc}}{n_H \sqrt{\alpha\beta}} \exp\left[-\sqrt{\frac{\alpha}{\beta}} \cdot n_o(z_o)\, H_o \cdot \exp\left(-\frac{z}{H_o}\right)\right] \tag{6-4}$$

where

$\mathcal{F}_{esc}$ = Atomic hydrogen energy escape flux from the exobase

H_o = Atomic oxygen scale height at a reference altitude z_o

$\mathcal{F}_{esc}$ is calculated on the same basis as the classical escape flux. Under conditions of the present investigation ($T_H \simeq 900\ ^oK$) , one calculates the difference between the hydrogen and the oxygen temperatures at the exobase to be

$$T' = T_H - T_O \Big|_{\substack{z = z_u \\ z_u \to \infty}} \simeq -30^\circ K \tag{6-5}$$

(see Appendix G for details of the calculations). The above value of T' does not vary appreciably with the exobase height (the exponent in Equation (6-4) is negligibly small).

The result arrived at in Equation (6-5) shows that at least for the present situation of $T_H \simeq 900\ ^oK$, the hydrogen and oxygen gases are nearly in thermal equilibrium. Thus, one observes that the measured geocoronal hydrogen temperatures

are to all practical purposes equal to the exospheric temperatures. It is apparent, however, that the difference between T_H and T_o is a strong function of T; for $T_o \simeq 2000^oK$, for example, $(T_H - T_o)$ is expected to be about -500^oK.

6.3.3 INTERPLANETARY H_α

No evidence of any detectable amount of interplanetary H_α was noticed in the present measurements. In the May 1972 and October 1972 observations, two to three points on the celestial sphere, with large angular displacements from one another, were tracked for a few hours each in succession on each night of the observations. Therefore, it was possible to add together all the data taken in the same direction. A given observation night was divided into two to three 'bins', each 'bin' corresponding to a different viewing direction (right ascension and declination) on the celestial sphere. If any one of the lines in the wings of the measured fringe profile were interplanetary H_α, it should be expected to be Doppler shifted from the laboratory position of H_α differently in different 'bins'. Such was not found to be the case when this exercise was carried out for several observation nights. As a matter of fact the positions of all the lines (principal maximum and the ones in the wings) of the various 'bins' of a given night overlapped, thus proving that none of the lines in the wings of the measured fringe profile could be due to interplanetary H_α emission.

6.4 OBSERVED GALACTIC H_α EMISSION

An enhanced H_α signal was noticed when the viewing mirrors looked at some regions of the Galaxy, while performing several

almucantar runs at various zenith angles on the nights of December 17-18, 1971 and December 18-19, 1971. The Vel-Pup region showed the strongest enhancement and three interesting galactic H_α scans were obtained with mirrors positioned to look in this direction. Fig. 19 shows a typical galactic H_α scan in the Vel-Pup region. One notes a comparatively strong, Doppler shifted, double-line H_α profile in this fringe. The double line profile is characteristic of the galactic recombination line emission. A semiquantitative analysis of the observed galactic H_α emission provides the following information.

(i) The mirrors were positioned to look approximately in the direction of declination, $\delta = -38^\circ$; and right ascension, RA = 124° at the time of making the scan. The viewing direction changed by only a few degrees during the period of 15 minutes it took to complete the scan. Therefore the direction of observation lies in the Vela-Puppis region. Barth's (1970) Mariner 5 measurements also showed enhanced L_α emission in the Vela-region in accord with the theory proposed by Münch (1962). However, the Mariner 6 measurements of Barth (1970) showed no such enhancement in the Vela region, on the contrary the Vela-region indicated the weakest emission and the maximum brightness was recorded in the Ophiuchus region. In this study, it was not possible to look into the Ophiuchus region during the December 1971 observing period, therefore it cannot be shown whether Ophiuchus is the brightest region. What can be said, however, is that the Vela-region does not appear to be the weakest in the galactic H_α emission, since amongst a number of H_α scans made in the plane of the Galaxy in December 1971, only the ones in the Vela-

Puppis-region showed any detectable amount of galactic H_α emission.

(ii) The two observed galactic H_α components were found to be Doppler shifted from their respective laboratory positions deduced from the hydrogen lamp H_α calibrations. It is not possible to tell from these isolated galactic H_α scans which order of interference is being recorded. Moreover one of the galactic H_α components was found to partially superpose on the geocoronal H_α line and a hydroxyl line . Therefore, it is not possible to state the Doppler shifts quantitatively. Rough estimates made on the observed Vela region H_α intensity by measuring the peak amplitude of the signal (and relating it to intensity), and on the temperature of the emitting region by measuring the half width of one relatively overlap-free galactic H_α component (and relating it to temperature through the theoretically simulated H_α profiles), yield the lower limits on their values as $\sim$16R and $\sim 5500^{\circ}$K. The maximum peak transmission of the H_α filter was assumed in calculating the intensity.

CHAPTER VII

CONCLUSIONS AND SUGGESTION FOR FUTURE RESEARCH

7.1 CONCLUSIONS

(i) Calculations indicate a maximum expected interplanetary H_α intensity of the order of 0.06 to 0.1 Rayleigh computed on the basis of the OGO V L_α observations and the Thomas' (1971) model which is found to best describe the distribution of the interplanetary hydrogen atoms. As expected, no evidence of the interplanetary H_α emission was seen in the present observations. This is due to its extremely weak signal and a rather low sensitivity of the Fabry-Perot interferometer used in this study.

(ii) The geocoronal H_α emission is weak, Doppler stationary and has a single line profile. Its average nighttime intensity, averaged over a range of viewing directions, is less than 10 Rayleighs. The intensity is greater for small solar depression angles and drops appreciably in the antisolar direction. The measured H_α intensites are in general agreement with the earlier measurements and theoretical predictions for similar conditions of the geometry of illumination.

The measured geocoronal hydrogen temperatures are consistently lower by about 50 to 150 ^{o}K than the Jacchia (1971) model exospheric temperatures. Considerations of the energy exchange between the hydrogen and oxygen atoms below the exobase show that the measured hydrogen temperatures reported here should be about the same as the oxygen temperatures. The heat exchange analysis (Appendix G) also reveals that as the temperatures get larger, the difference between the hydrogen and the oxygen temperatures increases rapidly.

(iii) Enhanced galactic H_α emissions were observed in the Vel-Pup region as predicted by theory and the Mariner 5 measurements. The galactic H_α emission is Doppler shifted and has a double-line profile; the lower limits on its intensity and on the temperature of the emitting region are 16 Rayleighs and 5500^{o}K respectively.

7.2 SUGGESTIONS FOR FUTURE RESEARCH

The question of interplanetary H_α profiles needs to be further examined experimentally. A narrow pass band H_α filter (see Fig. 14 for specifications) is very critical for unambiguous determination of the interplanetary H_α line profiles. To observe the emission it is essential to track a given point on the **celestial** sphere, preferably in the direction of the expected maximum, for several nights in succession; and then add the data. The requirement of collecting large amounts of data may be removed when photomultiplier tubes with high quantum efficiency become available.

It should be of interest to measure simultaneously the Doppler profiles of both the geocoronal H_α line and the atomic oxygen red line (λ 6300 $\mathring{A}$) to be able to retrieve and compare the hydrogen and oxygen temperatures; theoretical indications are that the two temperatures could be upto several hundred degrees different from each other, depending upon the prevailing exospheric temperatures.

The galactic emissions are of significance to both aeronomers and astronomers alike, the two have conflicting interests in them. Therefore, it would be beneficial to both, to map the entire Galaxy by making systematic Doppler measurements of the galactic H_α line.

APPENDIX A

H_α FINE STRUCTURE AND THE POSITION OF THE GEOCORONAL H_α LINE

A.1 H_α FINE STRUCTURE

Figure A-1 depicts the low lying energy levels of atomic hydrogen. Only principal quantum numbers n = 1 and 2 are selected to illustrate the fine structure and hyperfine structure splitting of levels. The interaction of electron spin angular momentum with the orbital angular momentum gives rise to the fine structure. The $^2P_{1/2}$, $^2S_{1/2}$ degeneracy is resolved by the Lamb splitting of $^2P_{1/2}$ and $^2S_{1/2}$ levels due to interaction of the elecron with fluctuations in the quantized radiation field. The interaction of the proton with the electron magnetic moment causes splitting of each fine structure level into a doublet, giving rise to the hyperfine structure. The effects of hyperfine structure are ignorable for the purpose of the current investigation.

Figure A-2 shows, in detail, the fine structure transitions contributing to the Balmer Alpha line of atomic hydrogen. The selection rules for the total angular momentum J and orbital angular momentum L are

$$\Delta J = 0, \pm 1$$

and

$$\Delta L = \pm 1$$

The term notation used in Figure A-2 is

$$n^{2S+1} L_J, \quad \text{where } \vec{J} = \vec{L} + \vec{S}$$

Since (2S + 1) is always equal to 2 for a single electron system, it is sometimes dropped from the notation and the configuration is written

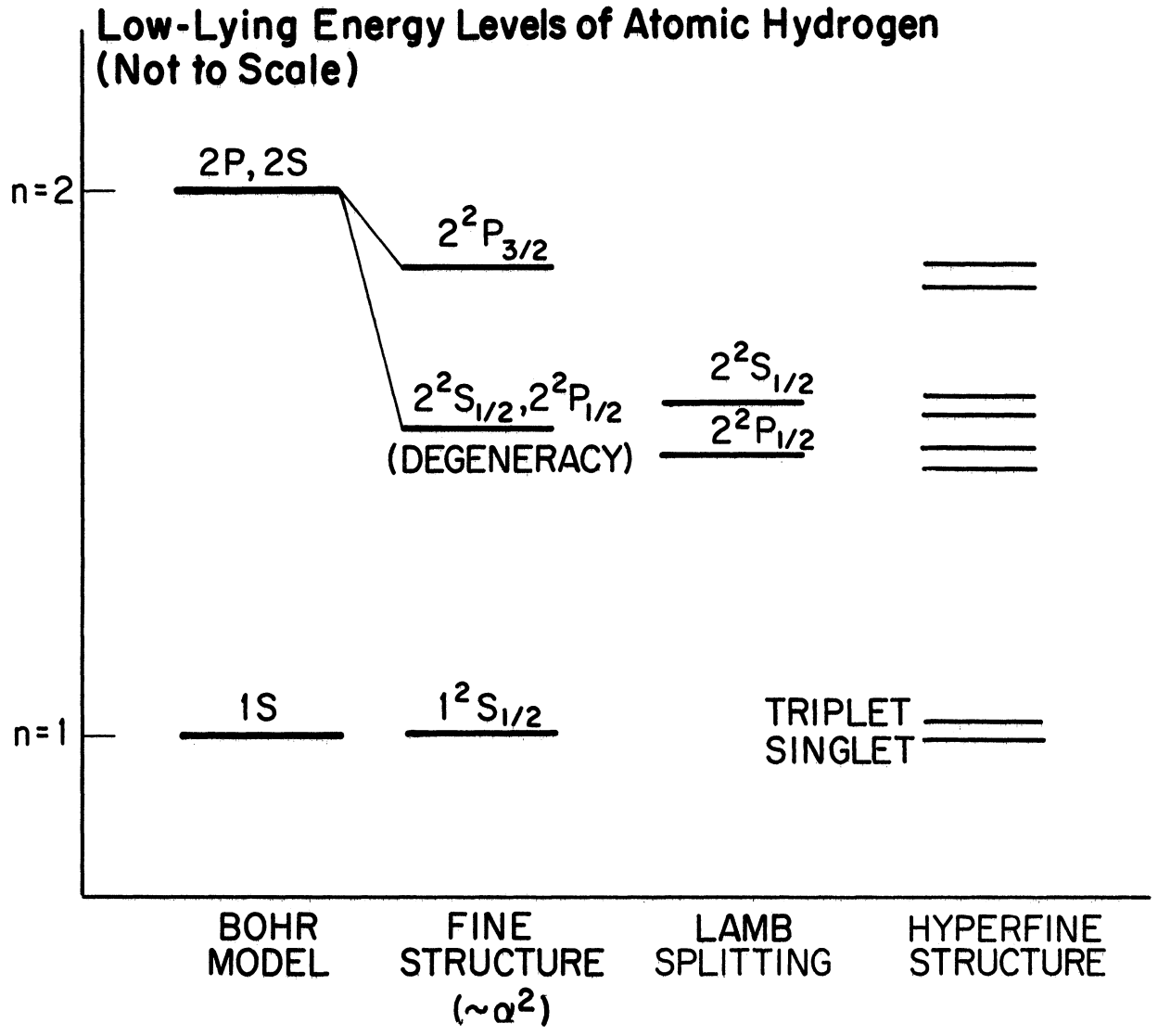

Fig. A-1. Energy level diagram of the low lying states of atomic hydrogen.

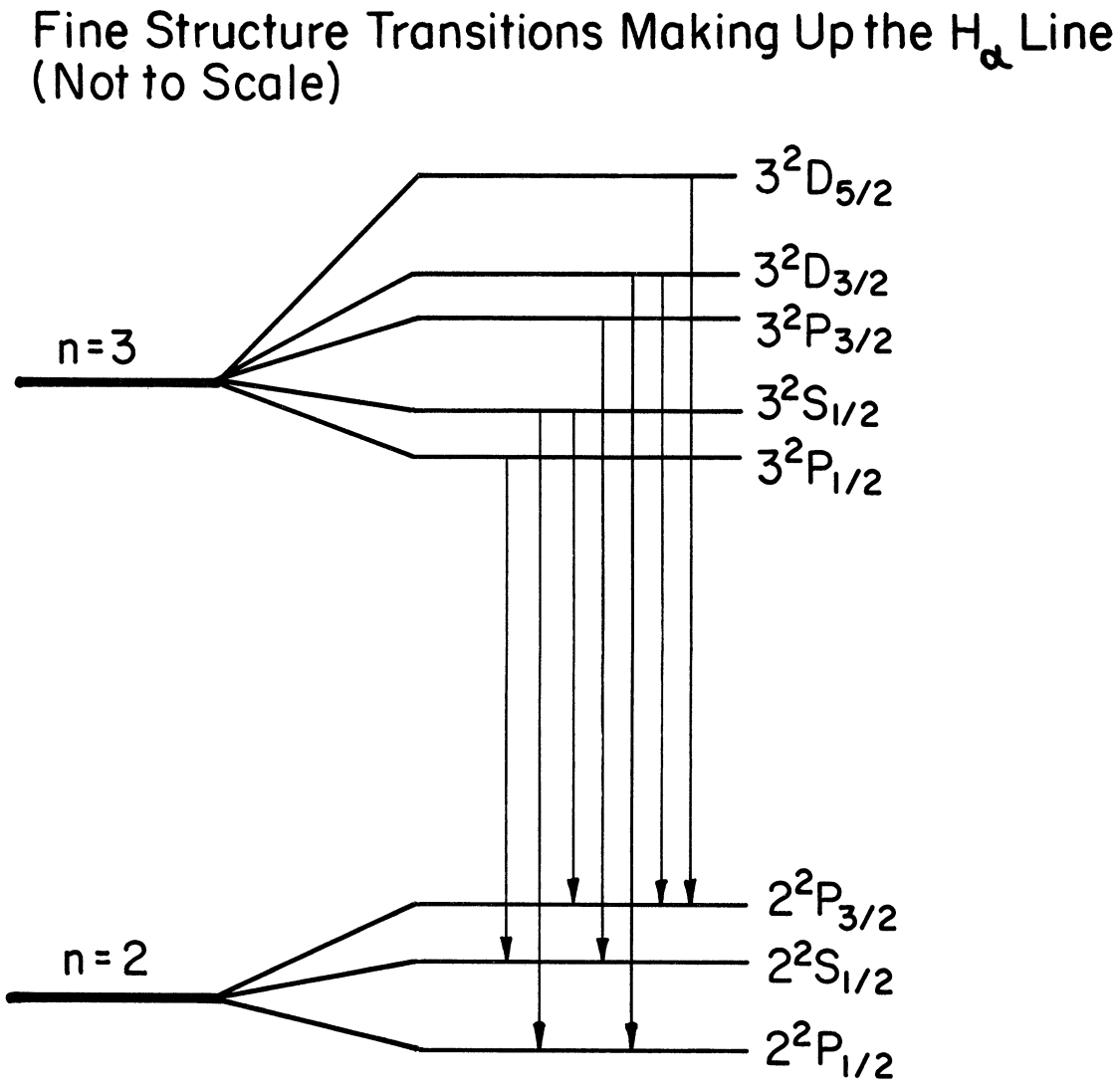

Fig. A-2. The seven fine structure components of H_α line on the basis of the selection rules $\Delta L = \pm 1$ and $\Delta J = 0, \pm 1$.

simply as,

$$^{n}L_{J}$$

For the purpose of determining the geocoronal H_α position from the position of a laboratory H_α source, it is useful to examine quantitatively the H_α fine structure on the basis of $\Delta J = 0, \pm 1$ selection rule.

Figure A-3 shows the five fine structure transitions and their separations on the basis of the selection rule for the total angular momentum J ($\Delta J = 0, \pm 1$). The relative intensities of the various fine structure transitions are represented by the vertical lines drawn at the bottom of the figure. The important features of the figure are:

1. Very weak components:

$$^{3}S_{1/2} - {}^{2}P_{3/2}$$

$$^{3}D_{3/2} - {}^{2}P_{3/2}$$

$$^{3}P_{1/2}\ (^{3}S_{1/2}) - {}^{2}S_{1/2}\ (^{2}P_{1/2})$$

2. Two strong components of approximately equal intensity which are further subclassified into:

   (i) Long wavelength component: $(^{3}D_{5/2} - {}^{2}P_{3/2})$

   (ii) Short wavelength component: $^{3}D_{3/2}\ (^{3}P_{3/2}) - {}^{2}P_{1/2}\ (^{2}S_{1/2})$

The separation between the two strong components is

$$= (0.355 - 0.036)\ \text{cm}^{-1}$$

$$= \frac{0.319}{10^{-8}} \times \lambda^{2}_{H_\alpha}\ \text{Å} = 0.1373\text{Å}$$

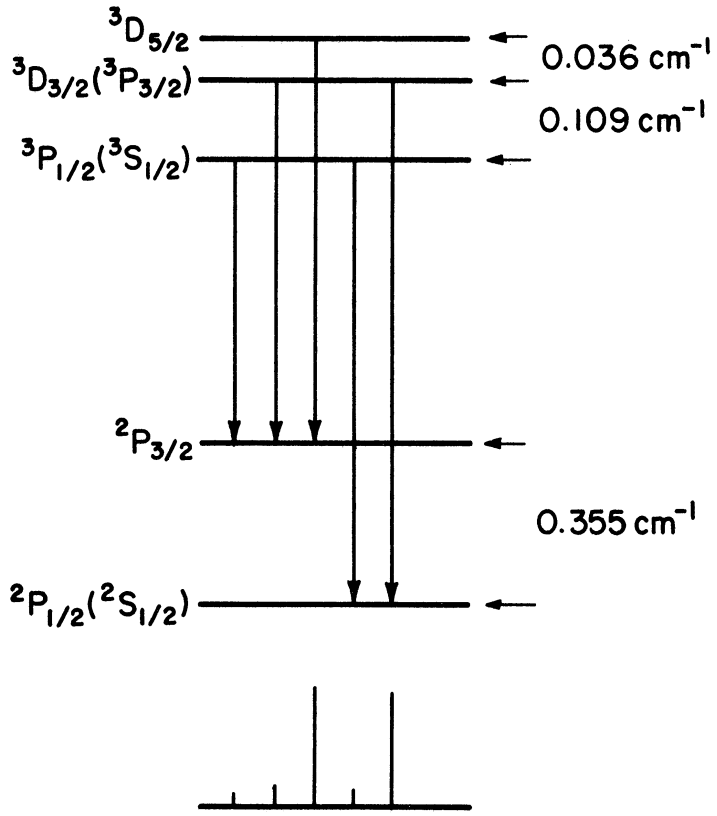

Fig. A-3. The five fine structure components of H_α line on the basis of the selection rule $\Delta J = 0, \pm 1$. The corresponding relative intensities are shown on the bottom scale.

The value of this separation between the two strong components was obtained experimentally by Williams (1938) who found it to be 0.010 cm^{-1} smaller than predicted by the theory. This discrepancy was later explained by the Lamb splitting of the ($^2S_{1/2}$, $^2P_{1/2}$) states (Lamb and Retherford, 1947). The ($^2S_{1/2}$) state lies 0.035 cm^{-1} above the $^2P_{1/2}$ state. The intensities of the transitions ($^3D_{3/2}$ - $^2P_{1/2}$) to ($^3P_{3/2}$ - $^2S_{1/2}$) are in the ratio 2.5 to 1, so that a smearing of these two closely spaced lines gives the 0.01 cm^{-1} discrepancy between the measurements and the theory (Richtmeyer et. al. 1955). The H_α fine structure has also been measured very recently by Hänsch (1972) and Hänsch et. al. (1972).

For the purpose of the current investigation, it should suffice to know that the $^2S_{1/2}$ level lies 0.025 cm^{-1} (0.0107 Å) above the 'composite strong level' of $^3D_{3/2}$ ($^3P_{3/2}$) - $^2P_{1/2}$ ($^2S_{1/2}$). This fact will be used later to determine the exact position of the geocoronal H_α.

A.2 EFFECT OF THE SEPARATION BETWEEN THE TWO STRONG COMPONENTS ON THE LABORATORY H_α LINE PROFILE

A hydrogen discharge tube was used for the purpose of laboratory H_α calibration. Presumably, dissociative recombination of H_2^+ gives atomic hydrogen in the excited state, resulting in a very broad H_α line. The width of the line greatly exceeds the instrument width of 0.065 Å. The width of the H_α profile from the lamp used is approximately 0.28 Å (corresponding to 2500 - 3000 ^oK temperature). As seen on the previous page, only two of the fine-structure transi-

tions contributing to H_α are strong, the separation between these two components is 0.1373 Å. If the H_α emission from the lamp were narrow, the two main components could be easily resolved with an instrument resolution of 0.065 Å. However, both the components emitted from the lamp are so broad (corresponding to approximately 2000 - 2500°K) that they superpose on each other giving an H_α profile which in the present case turns out to be symmetrical about the vertical drawn from the peak of the profile. This is what one will expect for two broad and equal intensity components superposing on each other. See Fig. A-4 for illustration.

A.3 GEOCORONAL H_α POSITION FROM THE HYDROGEN LAMP H_α LINE PROFILE

The geocoronal atomic hydrogen is excited from the ground state to n = 3 by solar L_β (see Fig. 5). The only allowed fine structure transitions from n = 1 to n = 3, using the selection rules $\Delta L = \pm 1$ and $\Delta J = 0, \pm 1$ are:

$$^1S_{1/2} - {}^3P_{3/2}$$

and

$$^1S_{1/2} - {}^3P_{1/2}$$

i.e. only $^3P_{3/2}$ and $^3P_{1/2}$ fine structure levels of the n = 3 state are populated. This also implies that the geocoronal H_α will be composed of the following fine structure transitions (according to the selection rules $\Delta L = \pm 1$ and $\Delta J = 0, \pm 1$):

$$^3P_{3/2} - {}^2S_{1/2}$$

and

$$^3P_{1/2} - {}^2S_{1/2}$$

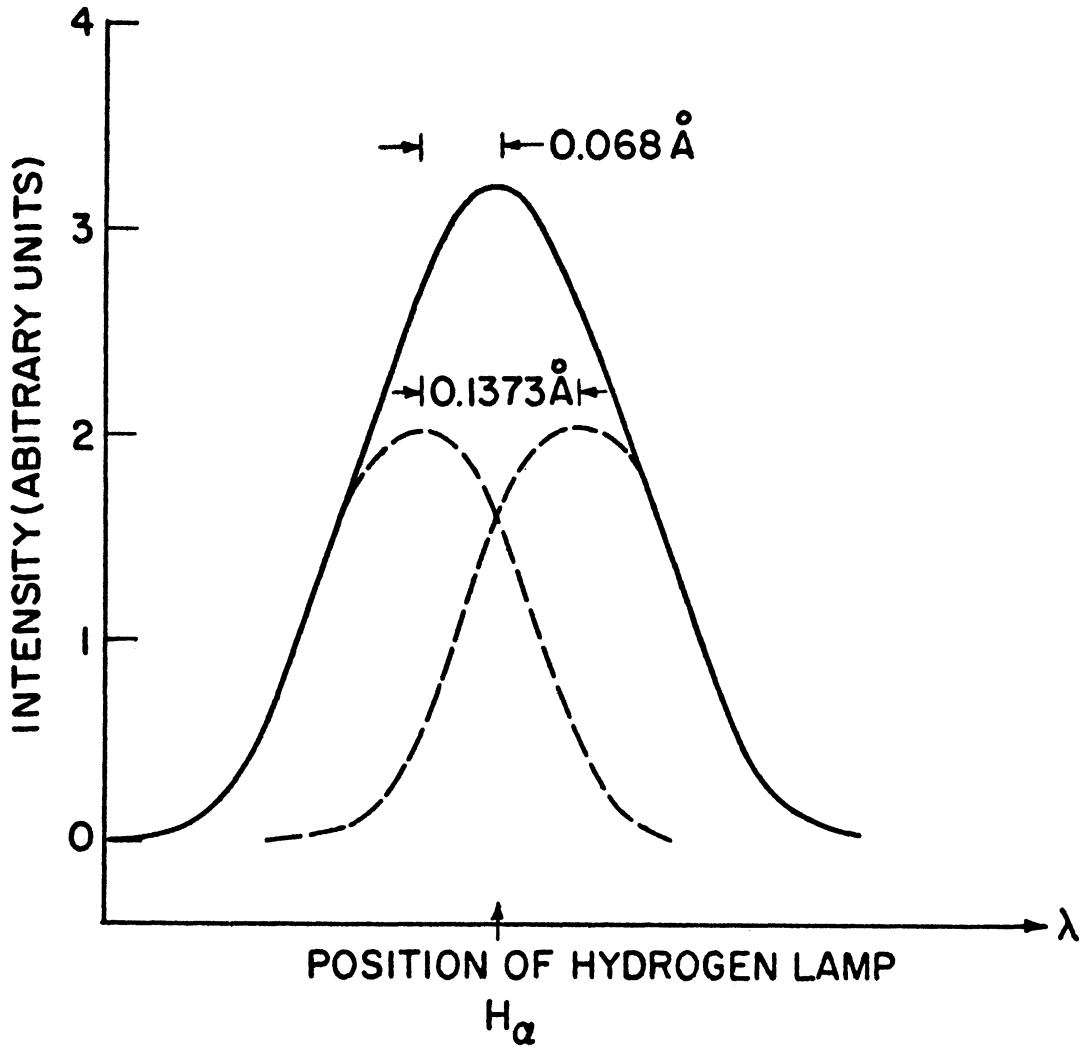

Fig. A-4. Sketch illustrating the addition of two equally intense and broad H_α fine structure components emitted by a loboratory hydrogen lamp.

($^3P_{1/2}$ - $^2S_{1/2}$) transition is extremely weak compared to ($^3P_{3/2}$ - $^2S_{1/2}$) transition. Therefore, geocoronal H_α may be taken as the result of one single transition ($^3P_{3/2}$ - $^2S_{1/2}$). This also means that the geocoronal H_α will be one single emission line and its profile can be used as such to derive the Doppler characteristics of the emission feature.

As mentioned earlier, the laboratory lamp H_α profile is symmetric about a vertical drawn from the peak of emission so that the two strong components making up this profile must lie at equal distances on either side of the peak. Thus, the peak of the shorter wavelength components which is the composite of the ($^3P_{3/2}$ - $^2S_{1/2}$) and ($^3D_{3/2}$ - $^2P_{1/2}$) must lie 0.0686 Å (= 0.1373/2) to the left of the peak of the observed lamp (H_α) profile. But, as explained earlier, only ($^3P_{3/2}$ - $^2S_{1/2}$) is responsible for geocoronal H_α emission and that the $^2S_{1/2}$ level lies 0.025 cm^{-1} (0.0107 Å) above the experimental 'composite level' described above. Therefore, the position of the geocoronal H_α emission is

$-(.0686-.0107)$ Å, relative to the laboratory lamp H_α, or

= 0.0579 Å to the left of the peak of laboratory H_α profile. The positions of the various above mentioned components are illustrated in Fig. A-5.

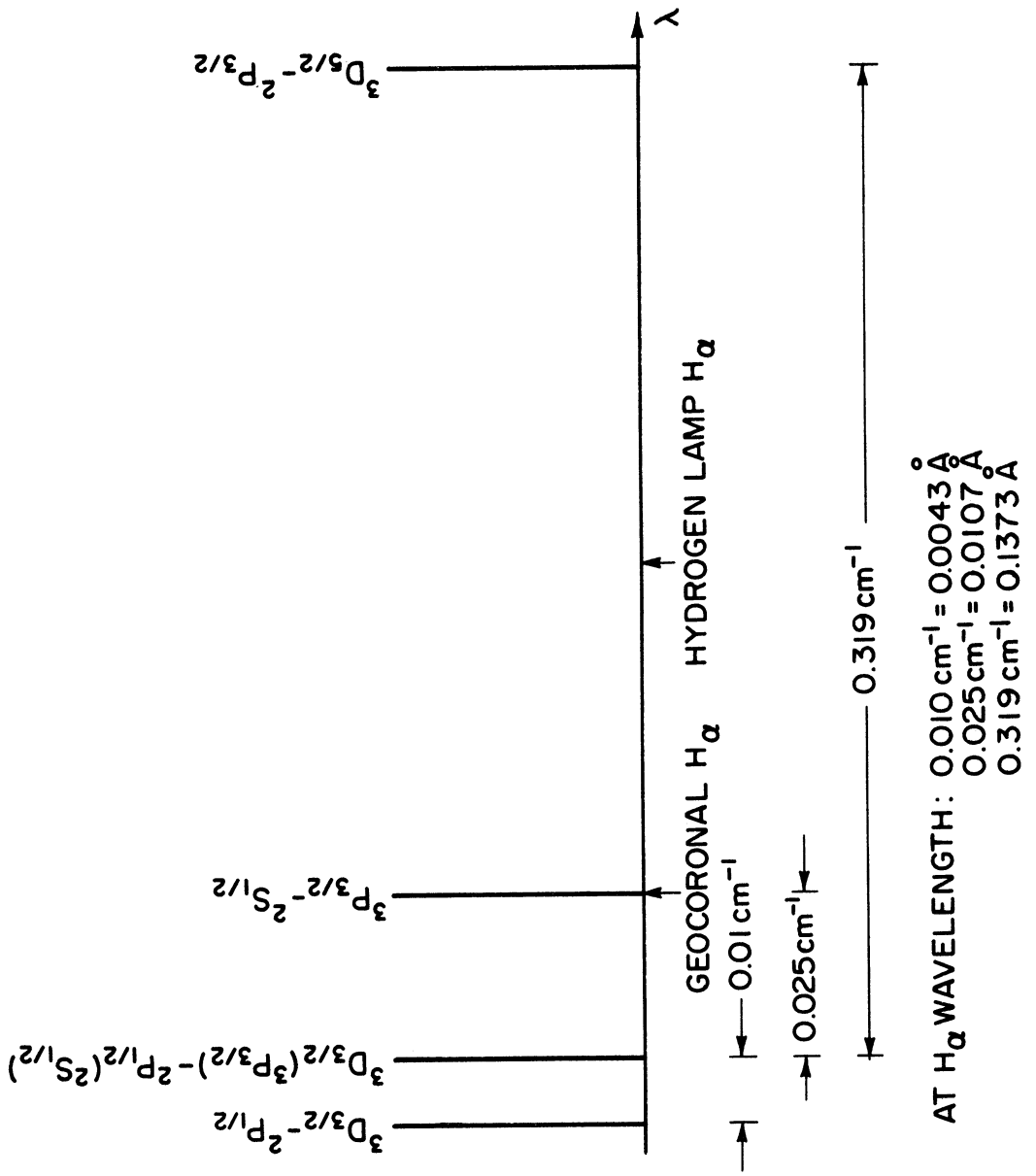

Fig. A-5. Diagram illustrating the relative positions of the geocoronal H_α and the laboratory hydrogen lamp H_α.

APPENDIX B

INTERPLANETARY HYDROGEN

B. 1 ORBITS OF BANKS' INTERPLANETARY HYDROGEN ATOMS

Due to relatively small kinetic energy of the hydrogen atoms, their orbital motion should be the same as that of the dust grains at the moment of release. Co-rotation of the dust is more likely (Wall, 1967), therefore hydrogen atoms, at the moment of release should be in direct orbit around the sun, with a velocity

$$v = v_o (r_o/r)^{1/2}$$

where v_o = 30 km. sec^{-1} at 1 AU

r_o = 1 AU

r = distance from the sun

After the release of neutral hydrogen atoms, their motion is governed by two competing influences, namely the solar gravitational force and the radiation pressure.

The solar Lyman α radiation pressure, at a distance r from the sun = $(\pi \mathcal{F}_\nu)_r \cdot \alpha_\nu \cdot h\nu/c$

where $(\pi \mathcal{F}_\nu)_{1AU}$ = Solar L_α line center flux at 1AU. Its value near the last solar maximum was ~ 2.8 x 10^{11} photons · $cm.^{-2}$ $sec.^{-1}$ $\mathring{A}^{-1}$ (Bruner and Parker, 1969).

and $(\pi \mathcal{F}_\nu)_r = (\pi \mathcal{F}_\nu)_{1AU} \cdot \left(\frac{r_o}{r}\right)^2$, $r_o = 1AU$

α = Absorption coefficient per atom = $f_{12} \pi e^2/mc$

f_{12} = 0.4162 (oscillator strength for L_α transition)

c = velocity of light

e = charge of an electron

m = mass of an electron

h = Planck's constant

ν = frequency of L_α

Thus, the solar L_α radiation pressure at a distance r from the sun is calculated to be

$$1.82 \times 10^2 / r^2 \quad \text{dynes}$$

The solar gravitational force on a hydrogen atom is

$$G \frac{M \cdot m_H}{r^2}$$

where G = Universal Gravitational Constant $= 6.7 \times 10^{-8}$ dyne·cm^2·gm^{-2}

M = Mass of the sun = 1.99×10^{33} gm

m_H = Mass of hydrogen atom = 1.67×10^{-24} gm

r = Distance from the sun

Therefore, the solar gravitational force at a distance r from the sun

$= 2.22 \times 10^2 / r^2$ dynes

And, the ratio between the above two forces is

$$R_{rs} = \frac{\text{Radiation Pressure}}{\text{Solar Gravitational Force}} = 0.82$$

Thus it is seen that even at the solar maximum the sun's gravitational force is somewhat larger than the radiation pressure. Pure gravitational focusing may not occur since the magnitudes of the two aforesaid forces are almost exactly equal. It is, however, apparent that Banks' (1971) general statement concerning the motion of neutral hydrogen atoms being 'rectilinear' at the moment of release is improper. More exactly the motion of the hydrogen atoms after their release from the dust grain, at a distance r from the sun is still dictated by the inverse square law of force, the force being the resultant of the gravitational force of the sun and the radiation pressure. In the above calculations for the magnitude of these two forces, conditions of solar maximum were assumed. On extrapolating Tousey et. al. (1964) measurements of the solar L_α flux in 1959 and 1962,

it is suspected that nearly a factor of five reduction in solar L_α line center flux from solar maximum to solar minimum will take place. Hence, at solar minimum, the effect of radiation pressure is reduced by nearly a factor of five and the solar gravitational force becomes the dominating factor in determining the motion of neutral hydrogen atoms after their release.

B. 2 MEAN FREE PATH FOR CHARGE EXCHANGE

In the following, the mean free path for charge exchange, $(mfp)_{CE}$ of interstellar hydrogen with the solar wind protons is calculated.

$$(mfp)_{CE} = \frac{V_{IS}}{n'_p \, v_p \sigma_{CE}}$$

where

$(mfp)_{CE}$ = mean free path for charge-exchange of the interstellar hydrogen

V_{IS} = Velocity of cold interstellar hydrogen, assumed to be $\sim$10 km. sec.$^{-1}$

n'_p = Solar wind proton number density downstream of the shock boundary

V_p = Solar wind velocity (= 400 km. sec^{-1})

σ_{CE} = Resonance charge exchange cross-section (= 2 x 10^{-15} cm^2, McDaniel, 1964)

Taking

$$(n_p)_{1AU} = 5 \text{ protons} \cdot \text{cm}^{-3}$$

and, for the shock boundary at 20 AU (Patterson et. al., 1963) one obtains $(n_p)_{20AU} = 5(\frac{1}{20})^2 = 1.25 \times 10^{-2}$ protons cm^{-3}

The value of proton density downstream of the shock, n'_p is taken four times its value upstream of the shock (Parker, 1962). Therefore,

$$n'_p = 5 \times 10^{-2} \text{ protons} \cdot \text{cm}^{-3}$$

With aforesaid values of the various parameters, one obtains

$$(\text{mfp})_{CE} \cong 16 \text{ AU}$$

Similarly, for the shock front at 50AU and $V_{IS} = 20$ km·sec, one obtains

$$(\text{mfp})_{CE} \cong 210 \text{ AU}$$

B.3 ABSOLUTE VALUE OF n_o in BLUM-FAHR MODEL

The Blum-Fahr model assumes an exponential form for the radial distribution of the cold hydrogen stream from the direction of the solar apex., i.e.

$$n(r) = n_o \exp(-r_c/r) \qquad \text{(B.3-1)}$$

where $n(r)$ = density of cold component at a distance r from the sun

r_c = penetration depth or the e-folding distance of the cold hydrogen density. Fahr (1970) calculated $r_c = 4$AU for the epoch of Vela-4 observations.

n_o = the interstellar hydrogen density at infinity.

The validity of the exponential law lies in the fact that n(r) has a vanishing value for small r's and its value approaches n_o for large r's, i.e.

Lt. $n(r) \to 0$, which means that most of the cold interplanetary hydrogen in the vicinity of the sun is lost by charge exchange and photoionization, and
$r \to o$

Lt. $n(r) \to n_o$, i.e., the solar system is immersed in the interstellar medium of density n_o.
$r \to \infty$

Fig. B-1 shows Fahr's (1970) interplanetary hydrogen density distribution in the direction of the solar apex as a function of the

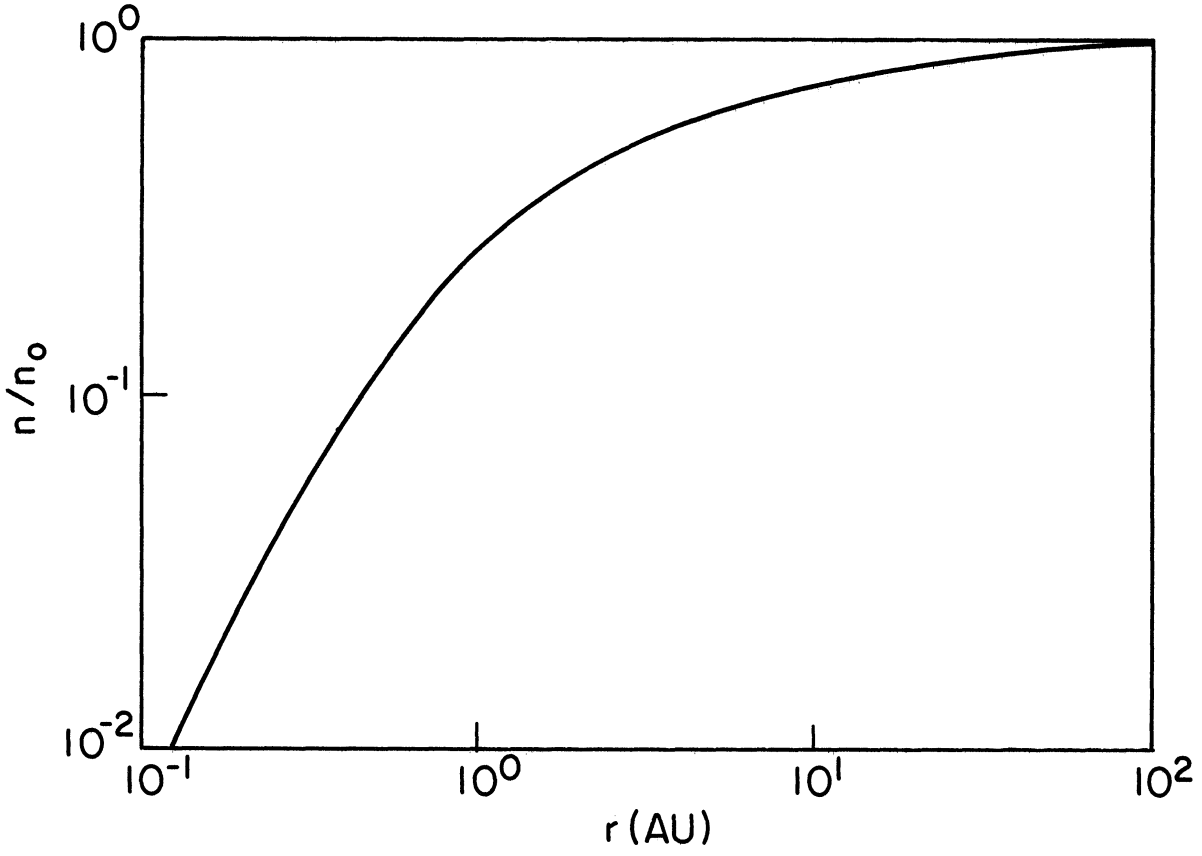

Fig. B-1. Density of the interplanetary hydrogen in the direction of approach as a function of the distance from the sun (Fahr, 1970).

distance from the sun.

The intensity (in Rayleighs) of the interplanetary L_α resulting from the resonance scattering of the solar L_α on the interplanetary hydrogen atoms, is given by

$$I = 10^{-6} \int_{r_0}^{\infty} (\pi F_\lambda)_{1AU} \cdot \left(\frac{r_0}{r}\right)^2 \cdot \alpha \cdot n(r)\, dr \qquad \text{(B. 3-2)}$$

All the terms appearing in the above expression have been defined in Sec. B. 1.

Fahr (1970) assumed a value of 4. 4 ergs $cm^{-2} sec^{-1}$ (2. 692 x 10^{11} photons $cm^{-2} sec^{-1}$) for the solar L_α flux at 1AU for the time of the Vela-4 L_α measurements (Chambers et. al., 1970). For I = 160 R measured by Vela-4, Blum-Fahr find n_o = 0. 06 H atoms · cm^{-3}.

The same value of n_o should be obtained on the basis of the OGO V L_α measurements of December 1969 reported by Bertaux and Blamont (1970). Bertaux and Blamont (1970), however arrive at a value of n_o which is a factor of 6 to 10 smaller than Fahr's (1970) value. The following simple calcualtion points out that Bertaux and Blamont's (1970) results for n_o are erroneous.

At the time of the December 1969 measurements of the L_α intensity reported by Bertaux and Blamont (1970), OGO V was between 19 and 21 earth radii and a maximum of 280 R of L_α was attributed to the solar L_α scattering on the interplanetary hydrogen atoms. The solar L_α line center flux at 1AU used by Bertaux and Blamont (1970) for December 1969 is 4. 7 x 10^{11} photons · cm^{-2} sec^{-1}. Therefore, with the help of Equation (B. 3-2), one finds that the Vela-4 and OGO-V L_α intensities are in the following ratio.

$$\frac{I_{B\text{-}B}}{I_{B\text{-}F}} = \frac{\left[n_o\,(\pi \mathcal{F}_\lambda)\right]_{B\text{-}B}}{\left[n_o\,(\pi \mathcal{F}_\lambda)\right]_{B\text{-}F}} \qquad \text{(B. 3-3)}$$

(subscripts B-B refer to Bertaux and Blamont (1970) and B-F to Blum - Fahr)

Hence

$$(n_o)_{B\text{-}B} = \frac{280}{160} \times \frac{2.7 \times 10^{11}}{4.7 \times 10^{11}} \times 0.06$$

or $$(n_o)_{B\text{-}B} \simeq 0.06 \quad \text{H atoms. cm}^{-3} \qquad \text{(B. 3-4)}$$

Thus, n_o derived from both the OGO-V (Bertaux and Blamont, 1970) and the Vela-4 measurements (Fahr, 1970) has the same value, and not a factor of 6 to 10 different as mentioned by Bertaux and Blamont(1970).

B. 4 DERIVATIONS OF SOME EXPRESSIONS IN SEC. 2. 7 (THE DOPPLER PROFILE CALCULATIONS)

B. 4. 1 EXPRESSION (2-10) FOR $d\mathcal{J}/d\lambda$: The reader is referred to Sec. 2. 7 and Fig. 6 for the definitions of the various symbols used here.

The Doppler shift of the emission line for the line of sight velocity V_r of the emitting atoms, is

$$\lambda - \lambda_o = \lambda_o \frac{V_r}{c} \qquad \text{(B. 4-1)}$$

or

$$\lambda - \lambda_o = \frac{\lambda_o}{c} V_o \cos\theta \qquad \text{(B. 4-2)}$$

θ can be expressed in terms of ϕ, R_s and R_e using the following sine law

$$\frac{\sin\theta}{R_e} = \frac{\sin\phi}{R_s} \qquad \text{(B. 4-3)}$$

On substituting Equation (B. 4-3) in Equation (B. 4-2), one obtains the following expression for the wavelength shift

$$\lambda-\lambda_o = \frac{\lambda_o V_o}{c}\sqrt{1-\left(\frac{R_e}{R_s}\right)^2 \sin^2\phi} \qquad \text{(B. 4-4)}$$

On differentiating Expression (B. 4-4), one obtains the following relationship for $d\lambda/dR_s$,

$$\frac{d\lambda}{dR_s} = \frac{\lambda_o V_o}{c}\cdot\left(\sqrt{1-\left(\frac{R_e}{R_s}\right)^2\sin^2\phi}\right)^{-1}\cdot\frac{R_e^2}{R_s^3}\cdot\sin^2\phi \qquad \text{(B. 4-5)}$$

The change in intensity dJ (in Rayleighs) within an interval of distance dr about I is given by :

$$dJ(R_s) = \eta(R_s)\,dr \times 10^{-6} \qquad \text{(B. 4-6)}$$

r can be expressed in terms of ϕ, R_s and R_e by the following relation :

$$r^2 + 2rR_e\cos\phi + (R_e^2 - R_s^2) = 0 \qquad \text{(B. 4-7)}$$

The quadratic Equation (B. 4-7) has the following two roots

$$r_{\pm} = -R_e\cos\phi \pm \sqrt{R_s^2 - R_e^2\sin^2\phi} \qquad \text{(B. 4-8)}$$

r_+ is the only valid root, since

$$\lim_{R_s\to R_e} r_+ \longrightarrow 0$$

and (B. 4-9)

$$\lim_{R_s\to R_e} r_- \longrightarrow -2R_e\cos\phi$$

On denoting the valid root r_+ simply by r, one has

$$r = -R_e\cos\phi + \sqrt{R_s^2 - R_e^2\sin^2\phi} \qquad \text{(B. 4-10)}$$

sothat

$$\frac{dr}{dR_s} = \frac{1}{\sqrt{1-\left(\frac{R_e}{R_s}\right)^2\sin^2\phi}} \qquad \text{(B. 4-11)}$$

On Substituting Equations (B. 4-5) and (B. 4-11) in Equation (B. 4-6), one obtains the following expression for $d\mathcal{J}/d\lambda$ in units of Rayleighs per Angstrom:

$$\frac{d\mathcal{J}}{d\lambda} = \left(\eta(R_s)\cdot R_s^3\right)\cdot\left(\frac{c}{\lambda_o V_o}\cdot\frac{1}{R_e^2}\times 10^{-6}\right)\cdot\frac{1}{\sin^2\phi}\times\left(1.5\times 10^{13}\right) \quad \text{(B. 4-12)}$$

which is same as Expression (2-10) of Sec. 2.7.

B. 4. 2 BOUNDS OF $(\lambda-\lambda_o)$:

The expression for the wavelength shift is given by (B. 4-4) as

$$\lambda-\lambda_o = \frac{\lambda_o V_o}{c}\sqrt{1-\left(\frac{R_e}{R_s}\right)^2\sin^2\phi}$$

case (i) $\phi \leq \pi/2 \quad (R_s \geq R_e)$

$$\text{lt.}_{R_s\to R_e}\ (\lambda-\lambda_o) \longrightarrow \frac{\lambda_o V_o}{c}\cos\phi$$

and

$$\text{lt.}_{R_s\to\infty}\ (\lambda-\lambda_o) \longrightarrow \frac{\lambda_o V_o}{c}$$

Therefore for the case $\phi \leq \pi/2$,

$$\frac{\lambda_o V_o}{c} > (\lambda-\lambda_o) > \frac{\lambda_o V_o}{c}\cos\phi \quad \text{(B. 4-13)}$$

case (ii) $\phi \geq \pi/2 \quad (R_s < R_e)$

In this case, for $(\lambda-\lambda_o)$ to be a real quantity, the limits are

$$\frac{\lambda_o V_o}{c} > (\lambda-\lambda_o) > 0 \quad \text{(B. 4-14)}$$

If one expresses the wavelength shift in terms of a non-dimensional parameter x, defined as,

$$x = \frac{\lambda-\lambda_o}{(\lambda_o V_o/c)} \quad \text{(B. 4-15)}$$

one obtains the following two conditions for the two abovementioned cases

$$\phi \leq \pi/2 : \quad 1 > x > \cos\phi \quad \text{(B. 4-16)}$$

$$\phi \geq \pi/2 : \quad 1 > x > 0 \quad \text{(B. 4-17)}$$

B. 4. 3 THE INTEGRATED INTENSITY

On integrating Expression (2-18) of Sec. 2. 7 over λ, one obtains the integrated intensity of the emission, i. e.

$$\mathcal{I}(R) = k' \int \frac{1}{\sin\phi} \cdot \frac{1}{\sqrt{1-x^2}} \cdot \exp\left(\frac{-r_c\sqrt{1-x^2}}{\sin\phi}\right) d\lambda \qquad \text{(B. 4-18)}$$

where, $\mathcal{I}(R)$ is the integrated intensity in Rayleighs

and $$x = \frac{\lambda-\lambda_o}{(\lambda_o V_o/c)} \qquad \text{(B. 4-19)}$$

so that

$$d\lambda = \frac{\lambda_o V_o}{c} dx \qquad \text{(B. 4-20)}$$

and for $\phi \leq \pi/2$, the limits of integration are $1 > x > \cos\phi$

Therefore, Expression (B. 4-18) becomes

$$\mathcal{I}(R) = k' \frac{\lambda_o V_o}{c} \int_{\cos\phi}^{1} dx \frac{1}{\sin\phi} \cdot \frac{1}{\sqrt{1-x^2}} \cdot \exp\left(\frac{-r_c\sqrt{1-x^2}}{\sin\phi}\right) \qquad \text{(B. 4-21)}$$

or

$$\mathcal{I}(R) = k' \frac{\lambda_o V_o}{c} \cdot \frac{1}{\sin\phi} \int_{\cos\phi}^{1} dx \cdot \frac{1}{\sqrt{1-x^2}} \exp\left(\frac{-r_c\sqrt{1-x^2}}{\sin\phi}\right) \qquad \text{(B. 4-22)}$$

let

$$r_c/\sin\phi = b \qquad \text{(B. 4-23)}$$

and

$$\sqrt{1-x^2} = w \qquad \text{(B. 4-24)}$$

so that

$$\frac{x\,dx}{\sqrt{1-x^2}} = \frac{-dw}{\sqrt{1-w^2}} \qquad \text{(B. 4-25)}$$

and the limits of integration are $0 > w > \sin\phi$. Therefore Expression (B. 4-22) becomes

$$\mathcal{I}(R) = k' \frac{\lambda_o V_o}{c} \cdot \frac{1}{\sin\phi} \int_{0}^{\sin\phi} dw \; \frac{e^{-bw}}{\sqrt{1-w^2}} \qquad \text{(B. 4-26)}$$

let

$$w = \sin\beta \text{, so that } dw = \cos\beta\, d\beta \qquad \text{(B. 4-27)}$$

and the limits of integration are, $\phi > \beta > 0$

Expression (B. 4-26) thus transforms to :

$$\mathcal{J}(R) = k' \frac{\lambda_0 V_0}{c} \frac{1}{\sin\phi} \int_0^{\phi} e^{-b\sin\beta} \, d\beta \qquad \text{(B. 4-28)}$$

A numerical integration on the right hand side of Equation (B. 4-28) will provide $\mathcal{J}(R)$ as a function of ϕ.

APPENDIX C

CALIBRATION OF OPTICAL COMPONENTS

Transmission and reflectance characteristics of the various optical components of the present Fabry-Perot interferometer were determined with the help of a Heathkit Monochromator Model EU-701. Viewing mirrors, glass and quartz plates, lenses etc. were checked for transmission. The Fabry-Perot etalons were calibrated for both transmission and reflectance. As an illustration, the technique for the calibration of the Fabry-Perot plates is presented below.

Prior to calibrating the optical component, the monochromator itself is calibrated to determine the offset between monochromator reading and the actual wavelength. This is done using a light source with known wavelengths of emission. In the present case, the Deuterium source of the monochromator assembly was used and monochromator readings were compared against standard D_α and D_β wavelengths for corrections, if any.

Dark current of the photomultiplier tube of the monochromator detector unit is determined next. A monochromator source is then selected in accordance with the desired range of wavelength scan. Normally a Deuterium light source is employed for 1750 to 4500 $\mathring{A}$ range and a Tungsten light source for 3500-30000 $\mathring{A}$ range. With the entrance slit open sufficiently wide to allow detectable light level, the intensity of the source is measured.

The Fabry-Perot plate is then inserted as shown in Fig. C-1 for the experimental set up. The transmitted intensity is recorded as a function of the wavelength. The transmission $T(\lambda)$ is given by the

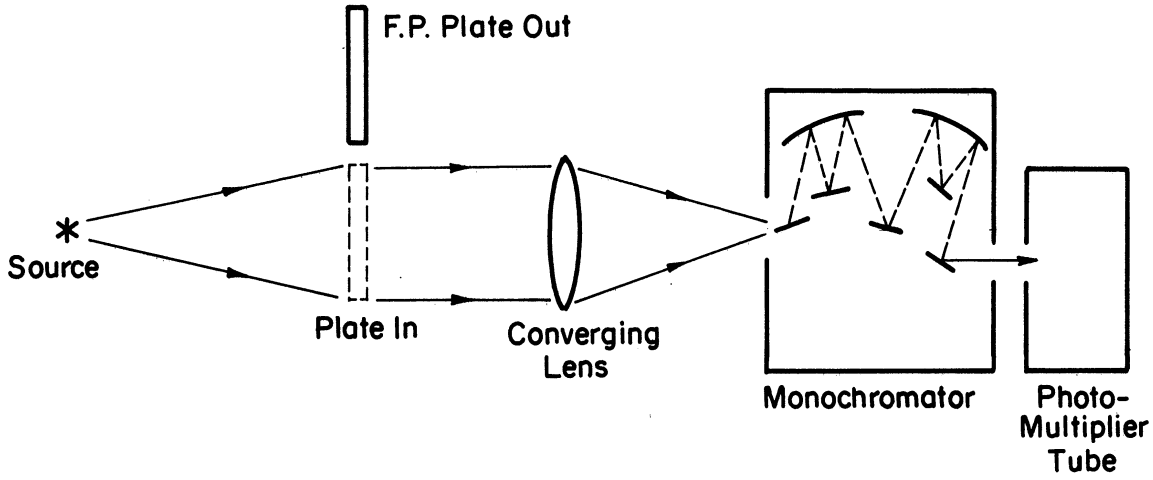

Fig. C-1. Experimental set-up for deriving the reflectivity of the Fabry-Perot plates from the transmission measurement.

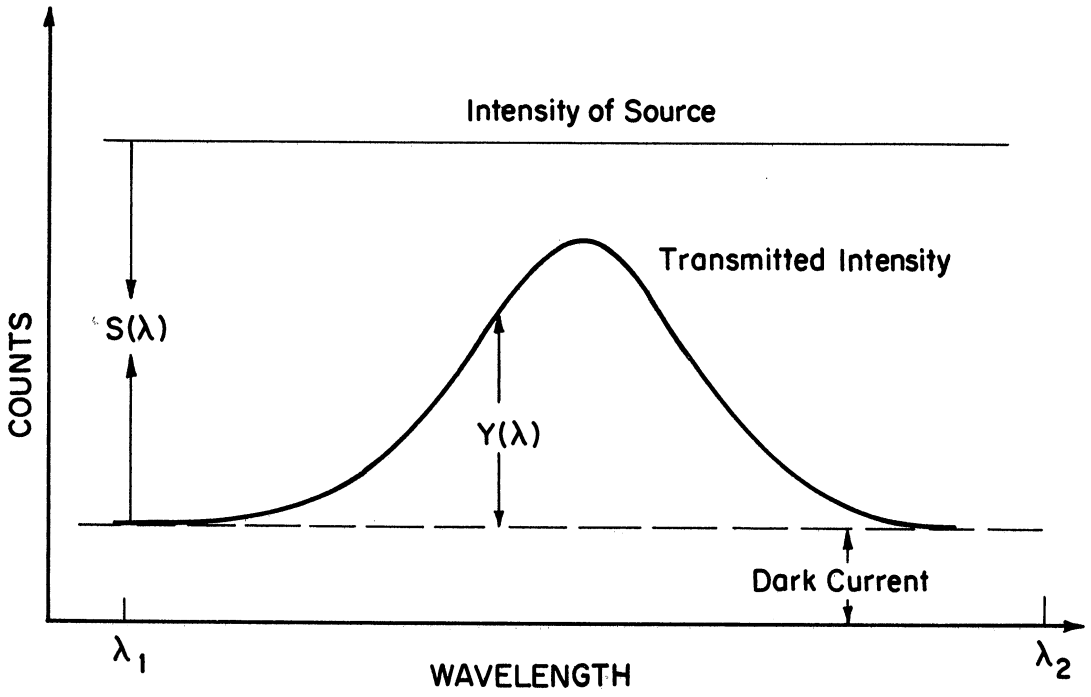

Fig. C-2. Illustration of the terms used for computing the transmission of an optical component.

relation

$$T(\lambda) = S(\lambda)/Y(\lambda)$$

where $S(\lambda)$ = Intensity of source - Dark Current

and $Y(\lambda)$ = Transmitted Intensity - Dark Current

(See Fig. C-2 for illustration of these parameters)

The reflectivity $R(\lambda)$ is then given by

$$R(\lambda) = 1-T(\lambda)$$

But if the plates have a certain amount of absorption, the reflectivity will be given by

$$R(\lambda) = 1-A(\lambda) - T(\lambda)$$

Since a direct measurement of the absorption of the plates is difficult, a 'direct' measurement of the reflectivity of the plates was made using an experimental set up shown in Figs. C-3(a and b). It was found that, at and about the H_α wavelength, absorption by the plates was negligible.

The same principle was employed to determine the transmission and reflectance of other optical components.

For the calibrations of various optical components, an on line PDP-8 computer was used to perform real time computations of the transmission or reflectance. Typically, a filter calibration took about 30 minutes.

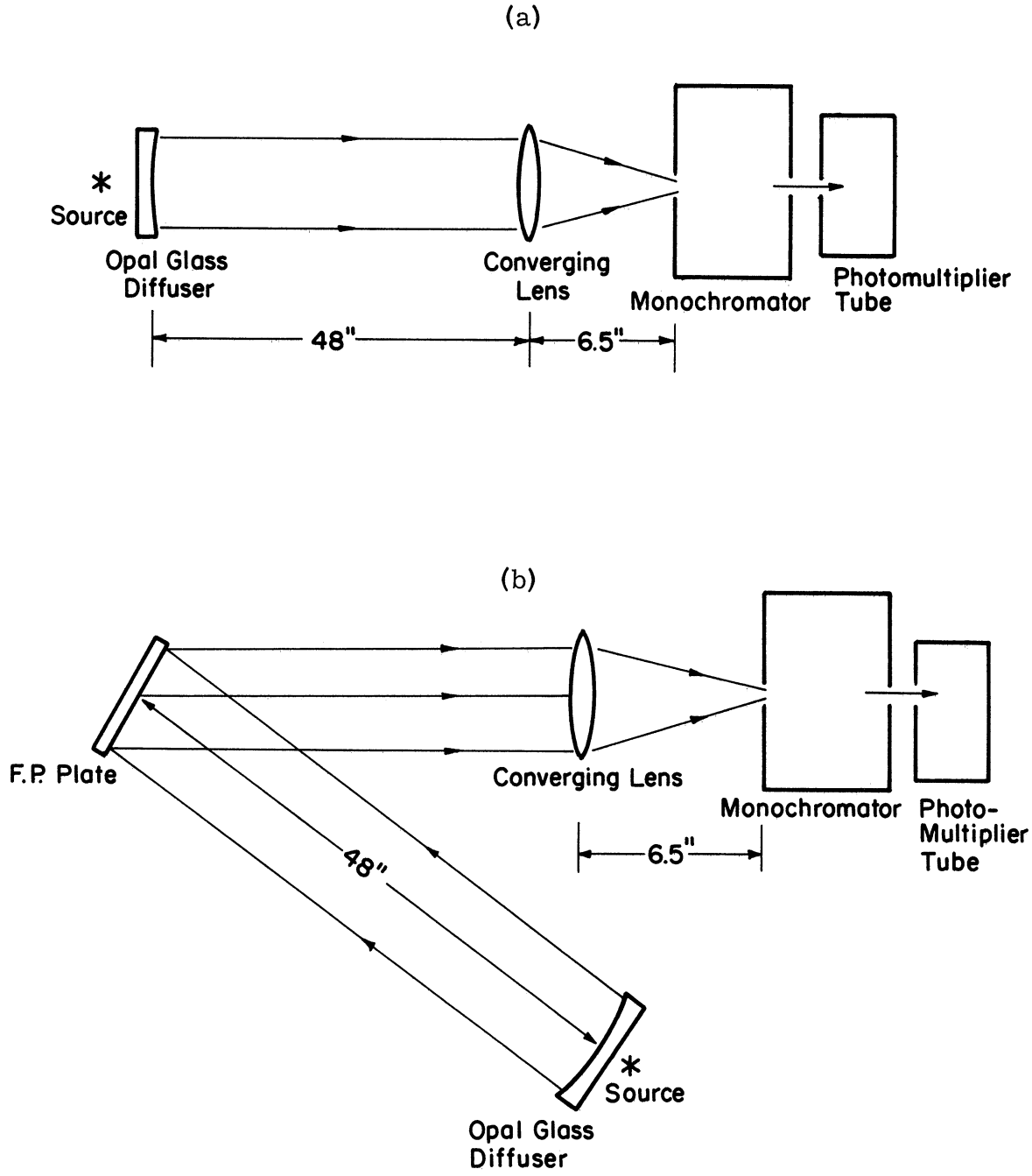

Fig. C-3. Experimental set-up for measureing the reflectivity of the Fabry-Perot plates 'directly'.

APPENDIX D

DETAILS OF THE FABRY-PEROT INTERFEROMETER

D. 1 INTRODUCTION

The operating parameters of the Fabry Perot interferometer used in the current work are presented in Table 7. Fig. D-1 represents a block diagram of the Fabry-Perot section of both the Michigan and Huntsville airglow facilities. A schematic drawing of the interferometer, associated electronic components and data recording systems is shown in Fig. D-2. The mechanical layout of the observatory has been described in detail by Roble (1969). Only the features of the layout modified in some respects or otherwise pertinent to the present H_α investigation will be described in Sec. D. 2. The optical adjustment and calibration procedures will be given in Sec. D. 3.

D. 2 MECHANICAL DETAILS

The etalon flats are made out of fused quartz. They are 3. 81 cm. thick with an effective diameter of 13. 3 cm. The MAO Fabry Perot plates have a dielectric reflective coating only over a central diameter of 13. 3 cm. The HAO plates on the other hand, are coated over the entire 15. 0 cm. diameter. The effective diameter of the HAO plates is, however still 13. 3 cm. since a black annodized aluminum spacer ring of ID = 13. 3 cm. and OD = 15. 0 cm. is placed between the plates. The formation of ghost images is prevented by cutting the quartz flats such as to maintain a 30 minute wedge on the unpolished faces. A precise spacing between the plates is maintained with the help of three small spacer 'discs' of 0. 25 cm. thickness and slightly less than 0. 6 cm. diameter. These discs are held in place between the plates with the help of a black annodized aluminum ring

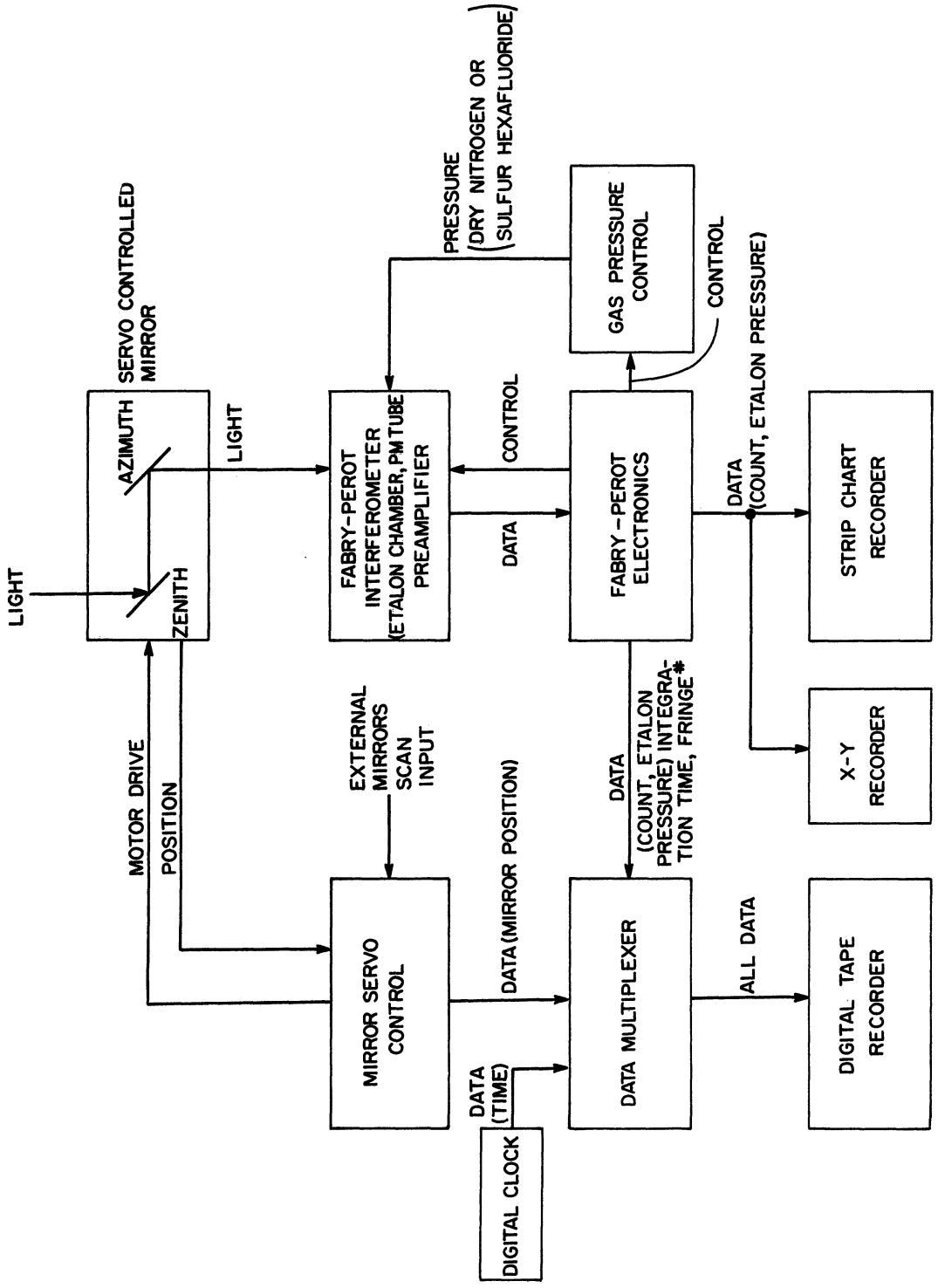

Fig. D-1. Block diagram of the Fabry-Perot section of the Michigan and Huntsville Airglow Observatories.

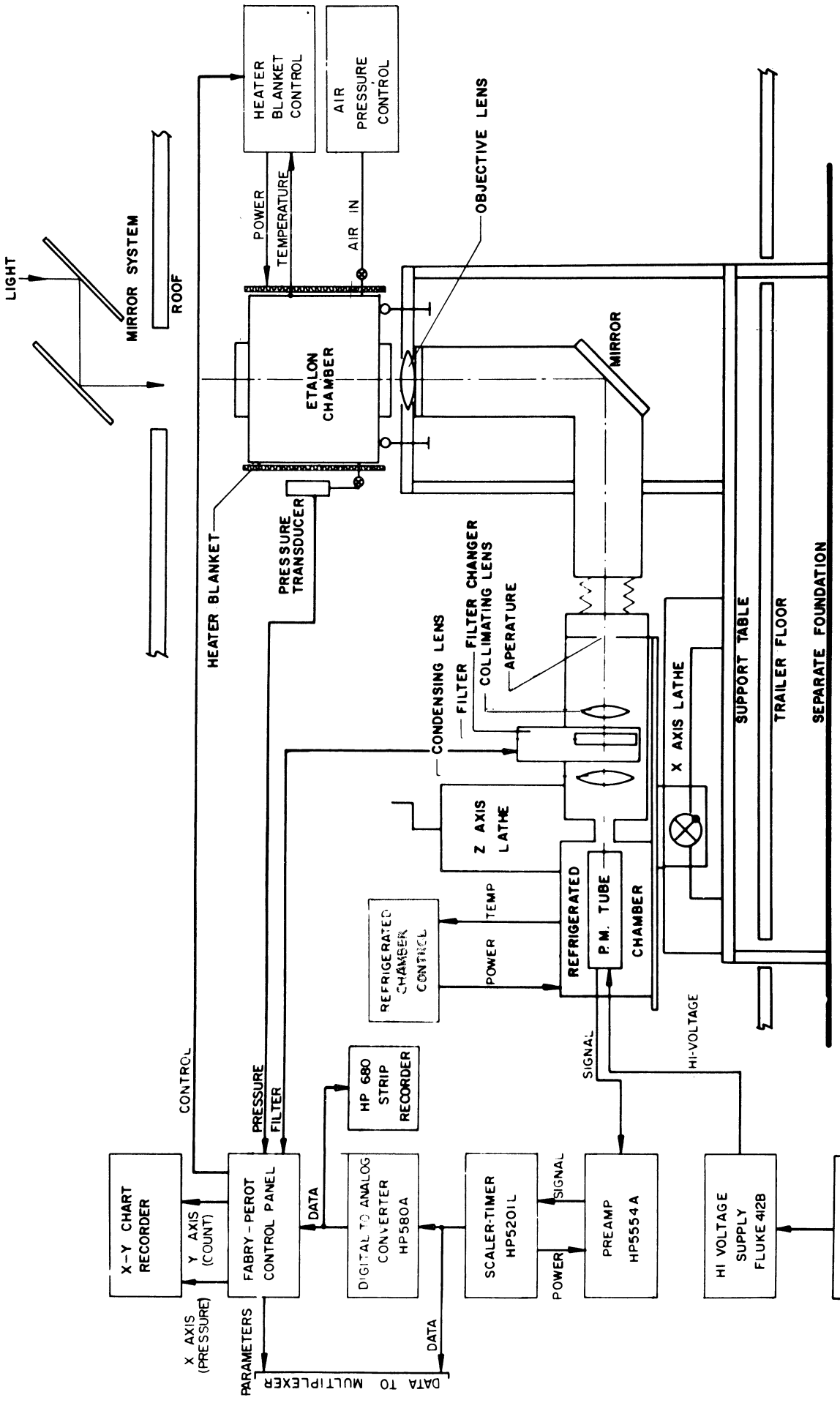

Fig. D-2. Schematic of the Fabry-Perot interferometer and associated components.

of 15.0 cm. (6 in) OD, 13.3 cm. (5.25 in) ID and nearly 0.16 cm (1/16 in) thickness, having three equi-spaced holes of about 0.63 cm. (0.25 in) diameter (Fig.D-3). The holes are large enough for the discs to slip in easily. The thickness of the ring is quite a bit smaller than the thickness of the 0.25 cm. discs so that slight warping of the ring due to minor temperature variations in the chamber do not affect the spacing between the plates.

The details of the horizontal mounting of the plates and spacer in the etalon chamber are shown in Fig. D-4. The central axis of the etalon points vertically up. The design of the mounting is similar to the one employed by Nilson and Shepherd (1961). The gravitational sagging of the plates may be prevented by mounting them vertically, but the ultimate instrument width is limited by the uniformity in the dielectric coatings and the reflectivity of the plates so that no great improvement would result by resting the plates on edge. Furthermore, demands placed on the instrument resolution for H_α investigation are not all that severe as to require alternate mounting schemes. The inner plate holder is thermally insulated from the outer pressure chamber. Any changes in the temperature of the outer chamber are, however transmitted to the inner chamber via convection currents in the scanning gas. The outer chamber is maintained at a constant temperature by a wire wound heater blanket around it. A proportional controller is used in conjunction with a thermistor to regulate the temperature of the chamber. Experience has shown that during the course of a scan, the chamber remains thermally stable. Recently it has also been possible to record on a magnetic tape the temperature of the chamber, along with the rest of the data at the end of each integration period.

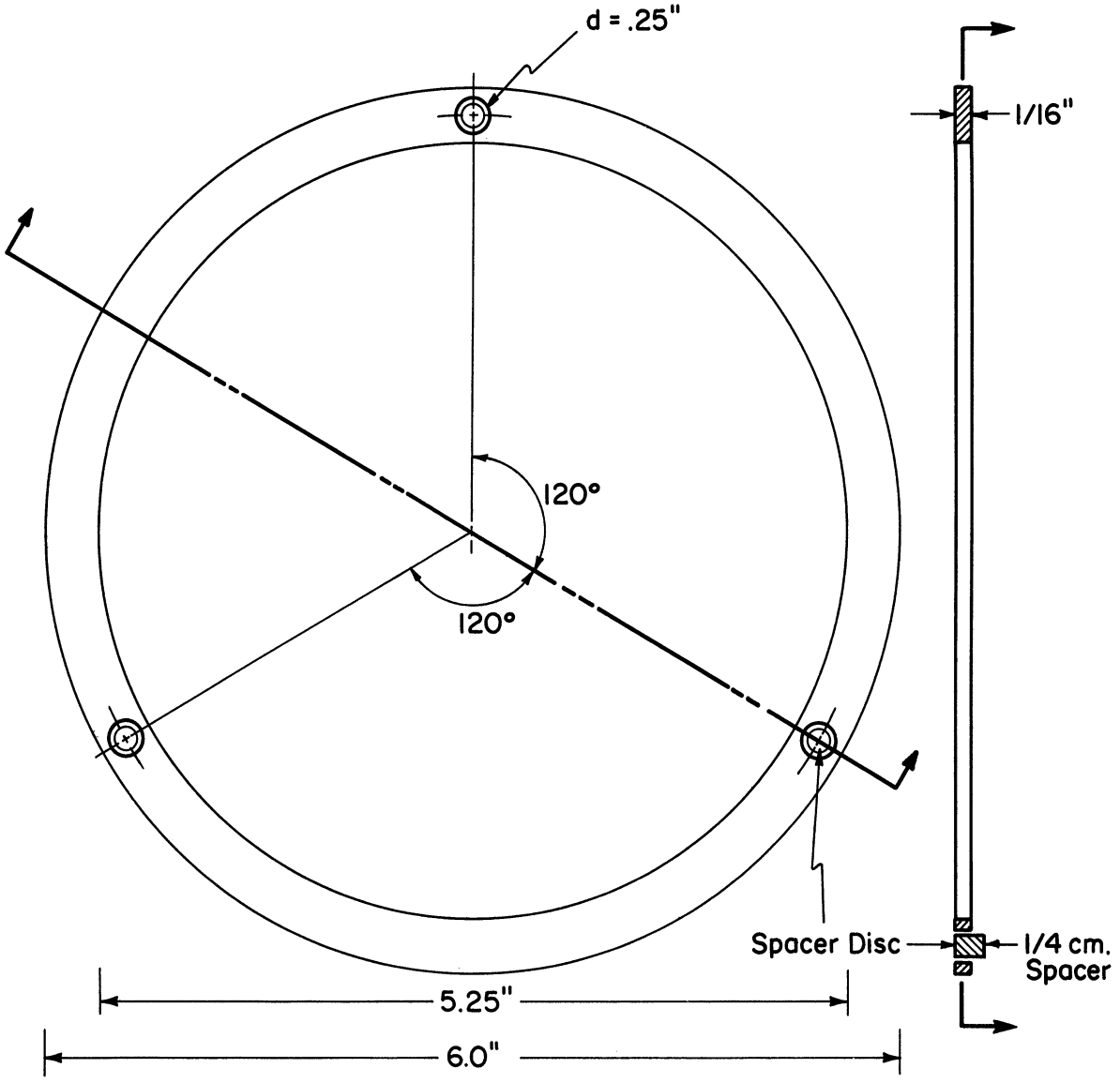

Fig. D-3. Drawing of the Aluminum ring designed to hold the spacer discs in place.

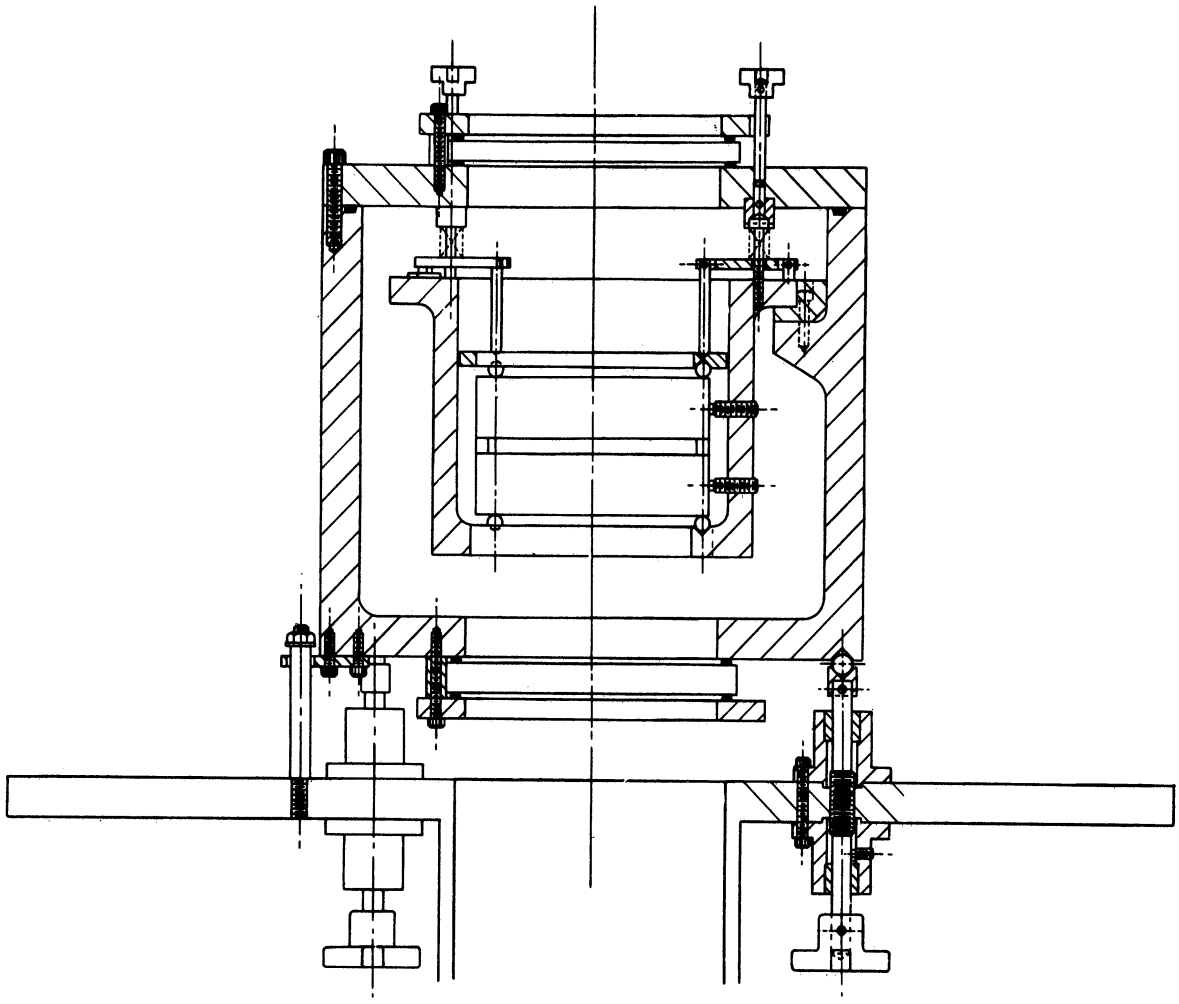

Fig. D-4. The Fabry-Perot interferometer etalon chamber and etalon plate holder.

If sporadic temperature changes do occur, they can now be considered in the data reduction procedure.

A wavelength scan across the profile of radiation is accomplished by varying the pressure of the scanning gas in the etalon chamber. A linear pressure scan is achieved by means of a high precision micrometer valve (Nupro model SS-4-S) which allows supersonic gas flow into the chamber resulting in a linear mass flow rate. The free spectral range at H_α wavelength for the 0.25 cm. spacer Fabry-Perot system is nearly 7.5 PSI pressure of dry nitrogen gas. When the system was being used for $\lambda 6300\text{Å}$ work, a 1 cm. spacing between the plates was sufficient and more than twice the free-spectral range could be scanned with a 5 PSI change of pressure of dry N_2. A 5 PSI (above the atmospheric pressure) pressure gauge was, therefore adequate for $\lambda 6300\text{Å}$ work. Two alternatives were weighed when the spacing was changed to 0.25 cm. First, the old 5 PSI pressure gauge could still be used if a new scanning gas with refractive index considerably higher than that of N_2 were used. For equal amount of pressure change, sulfur hexafluoride (SF_6) was found to scan almost three times the wavelength interval as dry N_2. Experience with SF_6 has shown that this gas is so viscous that purging time runs into tens of hours and therefore an incredibly large quantity of the gas is consumed while still purging the system. SF_6 is also considerably more expensive than high pure dry nitrogen. A second alternative, namely changing the pressure gauge to a higher range while still using dry nitrogen for scanning was eventually selected. A 10 PSI (above the atmospheric pressure) pressure gauge (adequate for the free spectral range scan at the H_α wavelength) Stratham Temperature Compensated Pressure

Transducer model PA 731 TC-25-350 was connected directly to the etalon pressure chamber. The strain sensitive wire elements of the transducer are arranged in the form of a Wheatstone bridge. A 6.9 Volt DC power supply was used to excite the transducer. An amplified output of the transducer is fed into the X-axis of an analog recorder. The sensor output is also digitized and recorded on a magnetic tape.

D.3 INSTRUMENT CALIBRATION AND ADJUSTMENT PROCEDURE

For general optical adjustment, alignment and calibration purposes of the entire Fabry-Perot, certain standard light sources were used. The general characteristics of such sources (a mercury lamp, a Helium Neon Laser and hydrogen lamp) are briefly presented below.

Preliminary adjustments and calibrations were preformed with the help of a water cooled, electrodeless mercury lamp. When cooled to an optimum temperature of $39^{o}F$, an $0.02\ cm^{-1}$ wide mercury line at 5461 $\mathring{A}$ results when the lamp is excited by a 100 MHz oscillator. A feedback pump was used to circulate water for cooling purposes through the outer jacket of the lamp.

Routine calibrations for determining the instrument performance were performed using a Perkin Elmer Model 5800 Gas Laser which is a d-c excited source of 6328 $\mathring{A}$ radiation with a collimated output beam approximately 1 mm in diameter. The output power is nearly 0.25 milliwatts. This laser contains a He-Ne plasma tube and two dielectrically coated quartz mirrors for producing a coherent beam of 6328 $\mathring{A}$ radiation. The laser output frequency is controlled by a piezoelectric crystal device. Maximum drift in the output frequency is ± 1 MHz per day in the closed loop. The coherence in the

beam is destroyed by a diffusing globe suspended above the etalon.

The laboratory position of the H_α line (in terms of the pressure of the scanning gas) is determined with the help of a hydrogen lamp. Light from such a lamp is directed on to a diffuser globe suspended above the etalon. The globe enables one to fill the entire plate area with uniform illumination. The filament type hydrogen lamp and its power supply are obtained from the ultra violet section of a model-13 Perkin Elmer Universal Direct Ratio Spectrophotometer. The filament requires an A. C. current of nearly 7 amp. at 2 Volts and a D. C. arc current of 0. 3 amp at 60 to 90 Volts. The power supply regulates the D. C. arc current to a constant value to ensure a non-fluctuating radiation output from the lamp. Experience has shown that the lamp has a stable output for not more than 10-15 minutes after first truning it on. Sometimes, turning the temperature of the arc to a maximum value helped stabilize the output, but only at the expense of the life-span of the lamp. The lamp has a life duration of about 200 hrs. under normal operating conditions. The hydrogen lamp in the Perkin Elmer spectrometer was meant for U-V region but for current H_α investigation, Balmer α radiation was isolated from the output of the lamp by passing it through a narrow band filter tuned at H_α wavelength.

Preliminary alignment and adjustments of the Fabry-Perot are carried out in the beginning. Under normal operating conditions, these adjustments need not be performed often. He - Ne laser calibration runs are, however made quite regularly and the instrument response deduced from the laser line shapes helps one determine whether or not optical alignments and adjustments are required at that time. The mounting of the optical box (which houses an aperture lens, an H_α

filter in a filter wheel and a condensing lens) on a lathe with motion in three axes makes the alignment procedure somewhat less complicated. Following steps are taken for preliminary alignment and adjustments of the system.

(i) Etalon chamber alignment: The etalon chamber is aligned such that the hole leading from the roof to the etalon fills the entire etalon field of view when viewed from the focal plane of the objective lens.

(ii) Aperture adjustment: The optical box is adjusted such that the image of aforesaid hole centers on the aperture.

(iii) Alignment of aperture lens, filter and condensing lens: A laser beam from the He-Ne laser is used to align the optical components of the optical box.

(iv) Preliminary plate adjustment: A crude adjustment of the plates for parallelism is carried out while the plates are outside the etalon chamber. After putting the aluminum ring and the spacer discs between the plates, interference fringes are formed with the help of a mercury lamp. Viewing the fringes from above, the eye is moved radially outward from the central spot. The fringes appear to grow in size. The plates are then turned relative to each other for the maximum parallelism, until a minimal growth in size of the fringes is observed. After this preliminary adjustment, the plates with the spacer are installed in the etalon chamber.

(v) Mirror adjustment: Diffuse light from the mercury lamp described earlier is allowed to illuminate the plate area uniformly. Green mercury line ($\lambda 5461 \mathring{A}$) fringes are formed in the focal plane of the objective lens. An opal glass or similar screen is installed in place of the aperature plate. The screen has a hole at the position of the aperture. The 45^{o}

mirror and the lathe are adjusted such that the central bright fringe of the interference fringe pattern is centered exactly on the hole in the screen.

(vi) Focusing of the fringes: The opal glass screen is now placed, with a cross mark, in the expected position of the photocathode of the detector which itself is housed in a thermoelectric cooler assembly. Once again, the interference fringes due to diffuse mercury light (from mercury lamp) incident on top of the etalon are formed on the opal glass screen. The central bright spot is then centered on the cross-mark of the screen with the help of adjusting screws on the optical box and the photomultiplier tube housing.

(vii) The pressure of the scanning gas is then held stationary at the fringe peak and both the optical box and the tube housing are adjusted to yield maximum photon count rate.

(viii) Final plate adjustment: Light from a He-Ne laser is directed on to a diffuse screen in the image plane of the fringes. The fringes are viewed from top of the etalon. The pressure of the scanning gas is held stationary at a value for which a reasonably bright central spot is obtained. The eye is then moved in concentric circles about the central bright spot. If the intensity of the fringes appears to vary along this path, the plates require finer adjustment for parallelism. This is accomplished by putting pressure on one or more of the three pressure points (which coincide with the position of the spacer discs) until no intensity variation along concentric paths about the central spot is noticed. At this point the plates are parallel to each other, as best as possible. Now if one views the fringes, once again radially out from the center, they still appear to grow in size. This limitation

is caused by the spherical defect in the plates, i.e., by natural gravitational sagging of the plates and by a non-uniform dielectric deposit on them.

(ix) Mercury lamp, He-Ne laser and hydrogen lamp calibrations: Once the entire Fabry Perot optics has been adjusted and aligned, calibration runs with above mentioned sources are carried out. Mercury line source is used for a reliable and quick evaluation of the instrument response. Since the lamp is a single isotope mercury source, a monochromatic radiation (λ 5461Å) which is sufficiently narrow and gaussian in shape is obtained. Various instrument parameters (e.g. finesse etc.) deduced from mercury line calibration are simply indicative of the instrument behavior and their values may not, as such, be used at H_α wavelength which is removed from λ5461Å by more than a thousand angstroms. The reflectivity of the plates at $^{\lambda}H_\alpha$, e.g., is very different from that at λ5461Å.

He-Ne laser is normally used to deduce instrument parameters at its wavelength (λ6328Å). It is much more convenient to use the laser than the mercury lamp if calibration runs are to be made routinely several times prior to, during and after the night sky observations. Laser wavelength is also much closer to H_α wavelength and the reflectivity of the plates does not change very much from 6328 to 6562.8Å. This implies that the instrument function derived from the laser calibration is pretty representative of the instrument behavior at $^{\lambda}H_\alpha$. Of course, when the instrument parameters were required to be known precisely at $^{\lambda}H_\alpha$, certain wavelength corrections had to be applied to the various broadening functions deduced at λ6328Å from the laser calibration.

Ideally, one would want to carry out only one single calibration at H_α wavelength, by using the technique of microwave excitation of water vapor. Balmer α line obtained from such a source is generally very narrow and may perhaps be used in place of the laser, thus giving the instrument functions at ${}^{\lambda}H_\alpha$ and laboratory position of H_α at the same time. Since such a device is very expensive and an ordinary hydrogen lamp and a He-Ne laser were already available, they were used instead. As mentioned earlier, the hydrogen Balmer α line obtained from the lamp is extremely broad, it could simply be utilized to tune the H_α filter and to determine the laboratory position of the H_α. In order to tune the filter at ${}^{\lambda}H_\alpha$, a crude calibration run with hydrogen lamp is made first. The pressure of the scanning gas is then held stationary at the peak of the interference fringe. The filter is then tilted until maximum photomultiplier counts are recorded.

APPENDIX E

EQUATORIAL COORDINATE TRANSFORMATION AND THE OBSERVATION SITES

Since the existing Fabry-Perot interferometer mirror system did not have an equatorial mount, a coordinate transformation from the equatorial (right ascension RA, and declination δ) to the horizontal (azimuth a, and zenith z) system of coordinates was necessary to allow the needed observations to be carried out. Such a spherical transformation yields sets of azimuth and zenith angles (as a function of the time of night) at the observer's latitude and longitude, for the given right ascension and declination.

If

HA* = Hour angle of the celestial body or point to be tracked

HAΥ = Hour angle of the First Point of Aries

Then

$$RA^* = HA\Upsilon - HA^*$$

or

$$HA^* = HA\Upsilon - RA^*$$

where RA* is the right ascension of the celestial point to be tracked. Thus, knowing the RA* of the celestial body, one can determine its hour angle at any instant. The hour angle of the First Point of AriesΥ is taken as reference, since Υ partakes in the common diurnal motion of the stars and its hour angle changes at the same rate as the hour angle of the stars. The difference of the HAΥ and the HA*, therefore remains constant.

If the latitude of the observer is ϕ, the transformation relations from equatorial to horizontal systems of coordinates are:

$$\cos z = \sin\delta \sin\phi + \cos\delta \cos\phi \cos h$$

where, h is the hour angle of the celestial body or point being tracked (h = HA*).

Having thus computed the zenith distance z, one can determine the azimuth angle a by the following relation

$$\cos a = \frac{(\sin\delta - \sin\phi \cos z)}{\sin z \cos\phi}$$

where, a lies between 0 and 180°
and,

a = Westerly for $h < 180^{\circ}$

a = Easterly for $h > 180^{\circ}$

and, the bounds on the zenith angle z are

$$180^{\circ} \geq z \geq 0^{\circ}$$

For $z > 90^{\circ}$, the celestial body is below the horizon. For the sun, the solar depression angle is

$$\text{Dep.} = z - 90^{\circ}$$

For the definitions of the various angular distances used in the above discussions, see Barlow and Crossby (1961). For illustration, see Fig.E-1, where x is the celestial body or the point to be tracked.

The value of HAΥ for the particular time and night of observation is taken from the appropriate Air Almanac.

Table 9 lists the various observation sites selected for the geocoronal Balmer α observations in December 1971, May 1972 and October 1972.

The declination and right ascension of the observation

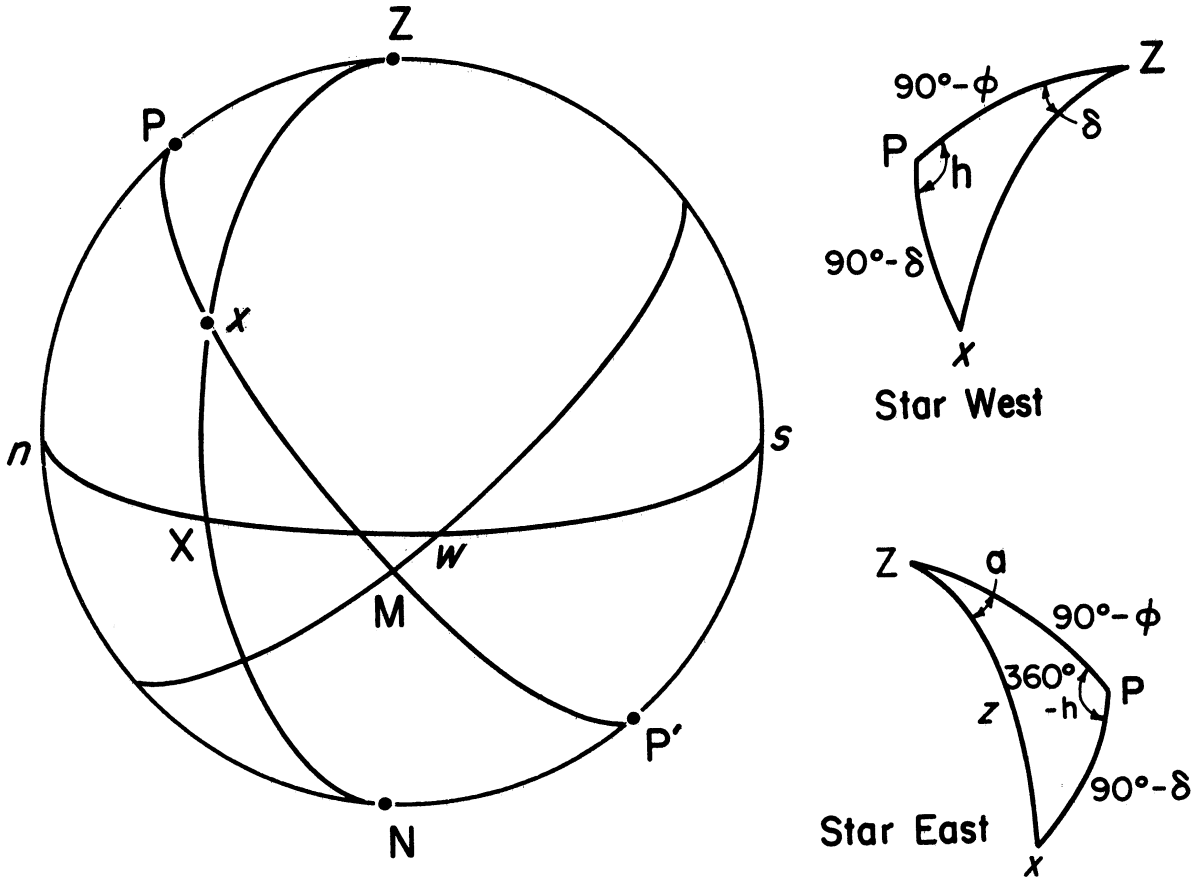

Fig. E-1. Geometry for the equatorial coordinate transformation.

TABLE 9.

OBSERVATION SITES

Observation Period	Declination (deg)	Right Ascession, RA (deg)	Approximate duration of tracking
May, 72*	-36.0	188.0	Until 2300 local time
	-18.0	212.0	2300-0100 local time
	+ 1.0	308.0	0100-morning local time
Oct., 72**	-10.0	12.0	Until midnight
	+ 1.0	52.0	After midnight

Note: December 1971 observations* were such that

(1) Zenith angle of the observations was between 70 and 75^{o}

(2) Azimuth angle of the observations relative to the solar azimuth angle was between 0 and 30^{o}

* Observations were made at HAO, MSFC (Latitude = 34.6^{o}N, Longitude = 86.6^{o}W)

** Observations were made at MAO, Ann Arbor (Latitude = 42.2^{o}N Longitude = 83.7^{o}W)

site are converted to the azimuth and zenith angles of observation as a function of the time of night. Solar azimuth and depression angles for the time of observation are also computed using a coordinate transformation similar to the one for observation sites. As an illustration, the geometry of illumination for the night of May 10-11, 1972 is presented in Table 10 .

The tabulation of solar depression angle begins with the time when the sun is below the horizon. The zenith angles of the sun prior to such time are not tabulated. No observations were carried out for solar depression angle less than 15^{o}.

The convention used for azimuth angles is as follows:

NES quadrants: North = 0^{o}, East = 90^{o}, South = 180^{o}

NWS quadrants: North = 0^{o}, West = 90^{o}, South = 180^{o}

The appearance of NES (or NWS) after a figure for azimuth angle represents the quadrant for that angle. Azimuth angles for all subsequent times are in that particular quadrant until a change of quadrant is indicated by an NWS (or NES) after a figure for azimuth angle.

TABLE 10.

May 10-11, 1972 Geometry of Illumination

	SUN		DIRECTION OF OBSERVATION	
GMT	Azimuth(deg)	Depression(deg)	Azimuth(deg)	Zenith(deg)
2300	80.8NWS		135.0NES	90.5
2310	79.5		136.5	89.1
2320	78.2		138.0	87.7
2330	76.9		139.5	86.3
2340	75.5		141.0	85.0
2350	74.2		142.6	83.7
2400	72.9		144.2	82.5
0010	71.5		145.9	81.3
0020	70.1		147.6	80.2
0030	68.7		149.3	79.1
0040	67.3	1.1	151.1	78.1
0050	65.8	3.0	152.9	77.1
0100	64.3	4.9	154.8	76.2
0110	62.8	6.7	156.7	75.4
0120	61.3	8.6	158.6	74.6
0130	59.7	10.4	160.6	73.9
0140	58.0	12.1	162.6	73.2
0150	56.4	13.9	164.6	72.6
0200	54.6	15.6	166.7	72.1
0210	52.8	17.2	168.8	71.7
0220	51.0	18.9	170.9	71.3
0230	49.1	20.4	173.0	71.0
0240	47.1	22.0	175.1	70.8
0250	45.1	23.5	177.3	70.7
0300	43.0	24.9	179.4	70.6
0310	40.9	26.3	178.4NWS	70.6
0320	38.7	27.6	176.3	70.7
0330	36.4	28.9	174.1	70.9
0340	33.9	30.0	172.0	71.2
0350	31.5	31.2	169.9	71.5

TABLE 10.

May 10-11, 1972 Geometry of Illumination (continued)

	SUN		DIRECTION OF OBSERVATION	
GMT	Azimuth(deg)	Depression(deg)	Azimuth(deg)	Zenith(deg)
0400	29.0	32.2	167.8	71.9
0410	26.4	33.2	171.5NES	53.1
0420	23.8	34.0	174.5	52.8
0430	21.0	34.8	177.5	52.7
0440	18.2	35.5	179.5	52.6
0450	15.4	36.1	176.5NWS	52.7
0500	12.5	36.6	173.5	52.9
0510	9.5	37.0	170.6	53.2
0520	6.6	37.3	167.6	53.6
0530	3.6	37.5	164.7	54.0
0540	0.6NES	37.5	161.9	54.6
0550	2.4	37.5	159.1	55.3
0600	5.4	37.4	156.4	56.1
0610	8.4	37.1	99.0NES	75.5
0620	11.4	36.8	100.5	73.5
0630	14.3	36.3	102.1	71.5
0640	17.2	35.7	103.7	69.5
0650	20.0	35.0	105.3	67.5
0700	22.7	34.3	107.0	65.5
0710	25.4	33.5	108.7	63.5
0720	28.0	32.6	110.5	61.6
0730	30.6	31.6	112.3	59.7
0740	33.1	30.5	114.2	57.8
0750	35.5	29.3	116.2	55.9
0800	37.8	28.0	118.3	54.1
0810	40.1	26.8	120.5	52.3
0820	42.2	25.4	122.8	50.5
0830	44.4	24.0	125.2	48.8
0840	46.4	22.5	127.7	47.1
0850	48.4	21.0	130.4	45.5

TABLE 10.

May 10-11, 1972 Geometry of Illumination (continued)

	SUN		DIRECTION OF OBSERVATION	
GMT	Azimuth(deg)	Depression(deg)	Azimuth(deg)	Zenith(deg)
0900	50.3	19.5	133.2	44.0
0910	52.2	17.9	136.2	42.5
0920	54.0	16.2	139.3	41.1
0930	55.7	14.5	142.6	39.8
0940	57.4	12.8	146.1	38.6
0950	59.1	11.0	149.7	37.5
1000	60.7	9.3	153.6	36.6
1010	62.3	7.4	157.6	35.7
1020	63.8	5.6	161.7	35.0
1030	65.3	3.7	166.0	34.4
1040	66.7	1.9	170.4	34.0

APPENDIX F

EFFICIENCY OF THE FABRY PEROT INTERFEROMETER USED

A standard calibrated low brightness source was not available at the time of making the H_α observations, therefore photomultiplier count rate was theoretically related to the intensity of the source of emission in Rayleighs in the following manner.

The recorded signal output, Y_{max}, at the peak of emission can be most approximately related to the 'effective' transmission of the Fabry Perot interferometer by the following relation (Hays and Roble, 1971).

$$Y_{max} = I_o = 10^6 \quad \frac{A\Omega}{4\pi} R_y \; T \; Q_e \; \frac{1-R}{1+R}$$

or

$$Y_{max/R_y} = 10^6 \quad \frac{A\Omega}{4\pi} T \quad Q_e \; \frac{1-R}{1+R} \text{ counts sec}^{-1}\text{Rayleigh}^{-1}$$

where
- A = Etalon plate area exposed to the incident radiation
- Ω = Instrument solid angle determined by the dimension of the aperture and the focal length of the objective lens
- R_y = Intensity of the source of emission in Rayleighs
- T = Effective transmission of the entire optical system
- Q_e = Quantum efficiency of the photomultifplier tube at $^{\lambda}H_\alpha$
- R = Reflectivity of the plates at $^{\lambda}H_\alpha$
- $\frac{1-R}{1+R}$ = Reflective loss on the etalon surfaces at $^{\lambda}H_\alpha$

$A\Omega/4\pi$ of the current instrument has been calculated with the knowledge of the geometry. With an aperture of diameter 0.436 cm and and objective lens of focal length 121.9 cm, a full field view of 0.2^o is obtained. Therefore, for an effective diameter of 13.3 cm of the Fabry-Perot plates, one gets:

$$\frac{A\Omega}{4\pi} = 1.35 \times 10^{-4}$$

The value for quantum efficiency Q_e of the photomultiplier tube at H_α wavelength was taken directly from the characteristic curves supplied by the manufacturers. Its value at $^{\lambda}II_\alpha$ for the particular tube used is 4.5%.

Reflectivity R of the two Fabry-Perot plates was measured in the manner described in Appendix C. At the H_α wavelength, R was found to have a value of 0.83, so that reflective loss

$$\frac{1-R}{1+R} = 9.3 \times 10^{-2}$$

The optical transmission of each of the optical components of the Fabry-Perot optics was measured individually in a manner described in Appendix C. The transmission of the H_α filter was measured to be 0.29 at 6562.8Å. All other optical components (azimuth and zenith tracking mirrors, glass plates above and beneath the etalon, two quartz etalon surfaces, objective lens, 45° mirror, collimating lens, condensing lens and two plexiglass surfaces) were found to have a transmission of about 0.9 at 6562.8Å. The overall transmission was thus found to have a value

$$T = 9.35 \times 10^{-2}$$

Taking $Q_e = 4.5\%$ at $^{\lambda}H_\alpha$ (from the manufacturer's specification curve), and using the above mentioned values of $\frac{A\Omega}{4\pi}$, $\frac{1-R}{1+R}$ and T, one calculates

$$CSR = (^{Y}_{max}/R_y) \simeq 0.05 \text{ count sec}^{-1} \text{ Rayleigh}^{-1}$$

where, CSR is the efficiency at H_α wavelength in counts $\text{sec}^{-1}\text{Rayleigh}^{-1}$.

In arriving at this figure for the efficiency of the particular Fabry-Perot interferometer two approximations were made.

(i) The quantum efficiency the photomultiplier tube was taken from the specification curves supplied by the company. Experience has shown

that the value of quantum efficiency quoted in the specifications of a certain model photomultiplier tube is only approximately true and individual tubes may have a somewhat different value.

(ii) The expression for count rate per Rayleigh was derived on the basis of the signal count rate at the peak of emission rather than considering the whole Doppler profile of the signal broadened by the instrument.

The CSR was later measured directly at 6300 $\mathring{A}$ when a calibrated low brightness radioactive source was available. The experimental value was then compared against the value calculated at 6300 $\mathring{A}$ by the method described in this Appendix. The calculated figure for CSR was found to be within 15% of the measured value.

Therefore, it can be concluded that the Fabry-Perot used for the present investigation yields nearly 0.05 count. sec^{-1} $Rayleigh^{-1}$ at 6562.8$\mathring{A}$ and this value is correct to within 15%.

APPENDIX G

SOLUTION OF THE HEAT TRANSFER EQUATION

The continuity equation for the energy exchange in elastic collisions between the hydrogen and oxygen atoms below the exobase will be solved and an analytic expression for the difference between the hydrogen and oxygen temperatures will be arrived at. For the region of interest where collisions between hydrogen and oxygen atoms predominate, the heat transfer equation is

$$\frac{\partial}{\partial z}\left(\lambda_o \frac{\partial T_H}{\partial z}\right) = \frac{du_H}{dt} \qquad \text{(G-1)}$$

where,

λ_o = Coefficient of thermal conductivity, as a function of altitude z

T_H = Atomic hydrogen temperature

$\frac{du_H}{dt}$ = Average rate of energy exchange in elastic collisions between the hydrogen and oxygen atoms.

$\frac{du_H}{dt}$ can be expressed as a function of the average momentum transfer cross-section, densities of the two gases and the difference between their kinetic temperatures. Desloge (1962) has obtained a general expression for $\frac{du}{dt}$, and on applying his special case for hard spheres to the particular situation at hand, one obtains the following form for $\frac{du_H}{dt}$

$$\frac{du_H}{dt} = 4\mu' k \bar{\sigma} n_H n_o \sqrt{\frac{8k}{\pi}} \cdot \left(\frac{T_H}{m_H} + \frac{T_o}{m_o}\right)^{1/2} \cdot (T_H - T_o) \qquad \text{(G-2)}$$

where,

k = Boltzmann constant

$\overline{\sigma}$ = Average Momentum transfer cross-section

n_H = Atomic hydrogen number density

n_o = Atomic oxygen number density

T_H = Atomic hydrogen temperature

T_o = Atomic oxygen temperature

m_H = Mass of a hydrogen atom

m_o = Mass of an oxygen atom

$\mu' = \frac{m_H m_o}{(m_H + m_o)^2}$

Substituting Equation (G-2) in Equation (G-1), one obtains the following differential equation:

$$\frac{\partial^2 T_H}{\partial \xi^2} - \frac{\alpha}{\beta}(T_H - T_o) = 0 \qquad \text{(G-3)}$$

where

$$d\xi = -n_o(z)\, dz$$

$$\alpha = \frac{k}{4}\sqrt{\frac{8kT_H}{\pi m_H}} \cdot \overline{\sigma} \qquad \text{(G-4)}$$

$$\beta = \frac{2}{3}\frac{k}{\overline{\sigma}}\sqrt{\frac{8kT_H}{\pi m_H}} \quad \text{(Banks, 1966)}$$

and

$$\lambda_o = \beta \frac{n_H(z)}{n_o(z)}$$

n_H and n_o = Atomic hydrogen and atomic oxygen number densities. n_H is assumed constant between the lower boundary z_o and the exobase

The following approximations were made in order to arrive at Equation (G-3) :

(i) $m_H \ll m_o$, so that

$$\mu' \simeq 1/16$$

and

$$\left(\frac{T_H}{m_H} + \frac{T_o}{m_o}\right)^{1/2} \simeq \sqrt{\frac{T_H}{m_H}} \qquad \text{(G-5)}$$

(ii) an exponential variation of n_o over altitude z was assumed, so that

$$\xi = \int_z^\infty n_o(z)\, dz = H_o\, n_o(z) \qquad \text{(G-6)}$$

where

H_o = Atomic oxygen scale height at the lower boundary z_o and assumed to be constant

The solution of Equation (G-3) has the following exponential form:

$$T' = A \exp\left(\sqrt{\frac{\alpha}{\beta}}\,\xi\right) + B \exp\left(-\sqrt{\frac{\alpha}{\beta}}\,\xi\right) \qquad \text{(G-7)}$$

where

$$T' = T_H - T_o \qquad \text{(G-8)}$$

One applies the following boundary conditions in order to solve for the constant A and B.

(i) At the lower boundary, $z = z_o$, the hydrogen and oxygen gases are assumed to have the same kinetic temperatures, so that

$$T_H = T_o \Big|_{z=z_o} \quad \text{or} \quad T' \Big|_{z=z_o} = 0 \qquad \text{(G-9)}$$

which implies that A=0

(ii)At the upper boundary, the exobase ($z \to \infty$; $\xi \to 0$) , however, the atomic hydrogen energy escape flux, $\mathcal{F}_{esc}$, satisfies the following condition:

$$-\lambda_o \frac{\partial T'}{\partial z}\Big|_{\substack{z=z_u \\ (z_u \to \infty)}} = \mathcal{F}_{esc} \qquad \text{(G-10)}$$

With the help of Expressions (G-6) and (G-10), one obtains

$$B = -\frac{\mathcal{F}_{esc}}{n_H \sqrt{\alpha\beta}} \tag{G-11}$$

Therefore, the expression for the altitude variation of the difference between the hydrogen and the oxygen temperatures is :

$$T_H - T_O = -\frac{\mathcal{F}_{esc}}{n_H \sqrt{\alpha\beta}} \exp\left[-\sqrt{\frac{\alpha}{\beta}} \cdot n_o(z_o) H_o \exp\left(-\frac{z}{H_o}\right)\right] \tag{G-12}$$

This expression requires knowledge of the rate of loss of energy, $\mathcal{F}_{esc}$, carried away by the escaping hydrogen atoms. This quantity is given by the expression

$$\mathcal{F}_{esc} = \frac{n_H m_H}{2\sqrt{\pi}} \frac{1}{\gamma^{3/2}} \left[e^{-\gamma v_{esc}^2} \left\{(\gamma v_{esc}^2)^2 + 2(\gamma v_{esc}^2) + 2\right\}\right] \tag{G-13}$$

where

$$\gamma = m_H / 2kT_H \text{ , and, } v_{esc} = \text{escape velocity} \tag{G-14}$$

This result is derived on the same basis as the classical escape flux (Chamberlain, 1963) calculated for a critical level above which there are no collisions. Combining Equations (G-12) and (G-13) one finds,

$$T_H - T_O = -\sqrt{\frac{3}{2}}\, T_H\, e^{-\gamma v_{esc}^2} \left[(\gamma v_{esc}^2)^2 + 2(\gamma v_{esc}^2) + 2\right] \tag{G-15}$$

This expression clearly illustrates the reduction in the hydrogen temperatures at high oxygen temperatures, where

$$T_H \longrightarrow \frac{T_o}{1+\sqrt{6}} \quad \text{as} \quad T_o \longrightarrow \infty \tag{G-16}$$

Under normal conditions in the atmosphere such as were investigated here ($T_H \simeq 900\ ^oK$) the hydrogen cooling effect is small with

$$T_H - T_o \simeq -30\ ^\circ K \qquad \text{(G-17)}$$

However, at temperatures of which occur at mid day and during magnetic storms, the hydrogen temperature will be several hundred degrees below the oxygen temperature.

REFERENCES

Abramowitz, M, and I. A. Stegun, Handbook of Mathematical Functions, Dover Publications 1965 .

Adams, T. F., The Diffusion of Lymanα through the Galaxy, Bull. Am. Astron. Soc. 2, 179, 1970 .

Adams, T. F., On Lyman Alpha Emissions from the Galaxy, Astron. & Astrophys, 12, 280, 1971 .

Allen, C. W., Astrophysical Quantities, Univ. of London, The Athlone Press, 1964.

Armstrong, E. B., Observation of the Airglow H_α Emission, Planet. Space Sci, 17, 407, 1967 .

Axford, W. I., A. J. Dessler, and B. Gottleib, Termination of Solar Wind and Solar Magnetic Field, Ap. J. 137, 1268, 1963 .

Auer, L. H., Transfer of Lyman Alpha in Diffuse Nebulae, Ap. J. 153, 783, 1968 .

Banks, P. M., Charged Particle Temperatures and Electron Thermal Conductivity in the Upper Atmosphere, Ann. de Geophys. 22, 577, 1966.

Banks, P. M., Interplanetary Hydrogen and Helium from Cosmic Dust and the Solar Wind, J. Geophys. Res., 76, 4341, 1971.

Barlow and Crossby, Mathematical Astronomy, 1961.

Barth, C. A., Mariner 6 Measurements of the Lyman-Alpha Sky Background, Ap. J. 161, L181, 1970 .

Bates, D. R. and M. Nicolet, The Photochemistry of Atmospheric Water Vapor, J. Geophys. Res. 55, 301, 1950.

Bertaux, J. L. and J. E. Blamont, Distribution of Atmic Hydrogen in the Upper Atmosphere and in the Solar System, Cospar XIII meeting Leningrad, 1970.

Bertaux, J. L. and J. E. Blamont, Evidence for a Source of an Extraterrestrial Hydrogen Lyman Alpha Emission: The Interstellar Wind, Astron. Astrophys. 11, 200, 1971.

Bertaux, J. L., A. Ammar and J. E. Blamont, OGO-5 Determination of the Local Interstellar Wind Parameters, XIV th COSPAR, Conference in Seattle, Wash. (1971). Published in Space Res. XII, Akademie Verlag, Berlin, p. 1559, 1972.

Biberman, L. M., Zh. Eksp. Teor. Fiz., 17, 416, 1947.

Biermann, L., Paper given at International Symposium on Pulsars and High Energy Activity in Supernova Remanants. Rome, 1970.

REFERENCES (continued)

Blum, P. W. and H. J. Fahr, Solar Wind Tail and the Anisotropic Production of Fast Hydrogen Atoms., Nature. 223, 936, 1969 .

Blum, P. W. and H. J. Fahr, The Distribution of Interplanetary Hydrogen, Ap. Ltrs. 5, 127, 1970a .

Blum, P. W. and H. J. Fahr, Interaction between Interstellar Hydrogen and the Solar Wind, Astron. & Astrophys. 4, 280, 1970b .

Blum, P. W., Neutral Interstellar Hydrogen and Extraterrestrial Lyman Alpha Radiation, XV COSPAR meeting, Madrid, May 1972.

Born, M. and Wolf, E., Principles of Optics, Pergamon Press, New York, 1965.

Brandt, J. C., On the Role of Secondary Scattering in the Lyman Alpha Problem, Planet. Space Sci. 9, 67, 1962a.

Brandt, J. C., The Lyman Alpha Problem and the Geocoma Hypothesis, Nature 195, 894, 1962b.

Bruner, E. C. and R. W. Parker, Hydrogen Geocorona and Solar Lyman Alpha Line, 1. Rocket Measurement of the Solar Line Profile, J. Geophys. Res., 74, 107, 1969.

Bruner, E. C. and W. A. Rense, Rocket Observations of Profiles of Solar Ultraviolet Emission Lines, Ap. J. 157, 417, 1969.

Burbidge, E. M., Proc. IAU Symposium 23, 181, 1964.

Clarke, D., P. H. Hindle, N. K. Reay and J. Ring, The Use of a Pressure-Scanned Fabry-Perot Interferometer for Twilight and Zodiacal Light Observations, J. de Phys., 28, C-2-294, 1967.

Chabbal, R., Recherche des Meilleures Conditions d'Utilisation d'un Spectrometre Photoelectrique Fabry Perot, J. Rech. Centre Nat. Rech. Sci. Lab. Bellevue, Paris 24, 138, 1953.

Chamberlain, J. W., Physics of the Aurora and Airglow, Academic Press 1961.

Chamberlain, J. W., Planetary Coronae and Atmospheric Evaporation, and Space Sci. 11, 901, 1963 .

Chambers, W. H., P. E. Fehlau, J. C. Fuller and W. E. Kunz, Anisotropic Atomic Hydrogen Distribution in Interplanetary Space, Nature 225, 713, 1970.

Chandrasekhar, S., Radiative Transfer, Dover Publications, 1952 .

REFERENCES (continued)

Chubb, T. A., H. Friedman, R. W. Kreplin, and P. Mange, Lyman Alpha Radiation in the Night Sky. Memoires Soc. Roy. Sc. Liege, 4, 437, 1961.

Daehler, M., J. E. Mack, J. O. Stoner, D. Clarke and J. Ring, Measurements of the H_α Profile in the Zodiacal Light Spectrum, Planet. Space Sci. 16, 795, 1968 .

Desloge, E. A., Exchange of Energy between Gases at Different Temperatures, Phys. Fluids, 5, 1223, 1962.

Dessler, A. J., Solar Wind and Interplanetary Magnetic Field, Review Geophys. 5, 1, 1967.

Donahue, T. M., Excitation of Lyman α in the night sky, Space Sci. Review 1, 135, 1962.

Donahue, T. M., H_α excitation in the hydrogen near the earth, Planet. Space Sci. 12, 149, 1964.

Donahue, T. M., The problem of atmoic hydrogen, Ann. Geophys. 22, 175, 1966.

Donahue, T. M. and G. E. Thomas, Distribution of Hydrogen in the Outer Atmosphere, Planet. Space Sci., 10, 65, 1963 a.

Donahue, T. M. and G. E. Thomas, Lyman α Scattering in the Earth's Hydrogen Geocorona, 2, J. Geophys. Res., 68, 2661, 1963 b.

Fabry C., and A. Perot, Ann. Chim. Phys. 7, 16, 1899.

Fahr, H. J., Interstellar Hydrogen Densities in the Surroundings of the Solar System, Nature, 226, 435, 1970 .

Fahr, H. J., Interstellar Matter and the Location of the Shock Front, Planet. Space Sci. 19, 1121, 1971a .

Fahr, H. J., Physics of Neutral Constituents in Planetary Exospheres, Physics of the Upper Atmosphere, F. Verniani (Editor) Editrice Compositori, 1971b .

Fesenkov, V. G., Zodiacal Light as the Product of Disintegration of Asteroids, Soviet Astron., A. J. (English Translation of Astronomicheskii Zhurnal) 2, 303, 1959.

Fishkova and Markova, On the Variations of the H_α Line Intensity in the Airglow Spectrum, Astronomical Circulars USSR, 208, 201, 1960 .

Fishkova, L. M., Intensity variations and space distribution of the λ6562Å HI emission in the night sky, Bull. Abastumani Astrophys. Observatory 29, 77, 1962.

REFERENCES (continued)

Gaynullina, R. H. and Z. V. Karyagina, Studies of Nightglow Spectrum in the Wavelength Region 6200-6600 Å, Izv. Astrophys. Inst. Kazakh, SSR Acad. Sci. 10, 52, 1960.

Hall, L. A. and H. E. Hinteregger, Solar Radiation in the Extreme Ultraviolet and its Variation with Solar Rotation, J. Geophys. Res. 75, 6959, 1970.

Hänsch, T. W., Repetitively Pulsed Tunable Dye Laser for High Resolution Spectroscopy, Appl. Optics, 11, 895, 1972 .

Hänsch, T. W., I. S. Shahin, A. L. Schawlow, Nature Phys. Sci., 235, 63, 1972 .

Hays, P. B. and R. G. Roble, A Technique for Recovering Doppler Line Profiles from Fabry-Perot Interferometer Fringes of Very Low Intensity, Appl. Opt. 10, 193, 1971.

Hernandez, G., Analytic Description of a Fabry Perot Photoelectric Spectrometer, Appl. Opt. 5, 1745, 1966.

Hindle, P. H., N. K. Reay and J. Ring, H_β Radiation in the Spectrum of the Night Sky, Planet Space Sci, 16, 803, 1968 .

Hinteregger, H. E., The Extreme Ultraviolet Solar Spectrum and its Variation during a Solar Cycle, Ann. Geophys., 26, 547, 1970.

Holstein, T., Imprisonment of Resonance Radiation in Gases, Phys. Rev. 72, 1212, 1947.

Hundhausen, A. J., Interplanetary Neutral Hydrogen and the Radius of the Heliosphere, Planet. Space Sci., 16, 783, 1968 .

Ingham, M. F., The nightglow spectrum II, H_α radiation in the night sky, Mon. Not. Roy. Ast. Soc. 124, 523 , 1962.

Ingham, M. F., Observations of the night sky H_α emission line, Mon. Not. Roy. Ast. Soc. 140, 155 , 1968.

Jacchia, L. G., Revised Static Model of the Thermosphere and Exosphere with Empirical Temperature Profiles, Smithson. Astrophys. Obs. Special Report, 332, 113, May 5, 1971.

Jacquinot, P., The Luminosity of Spectrometers with Prisms, Gratings or Fabry Perot Etalons, J. Opt. Soc. Amer. 44, 761, 1954.

Jacquinot, P., New Developments in Interference Spectroscopy, Rept. Progr. Phys. 23, 267, 1960.

Jeans, J. H., The Dynamical Theory of Gases, Cambridge U. Press, Fourth ed., 1925.

REFERENCES (continued)

Johnson, F. S. and R. A. Fish, The Telluric Hydrogen Corona, Ap . J. 131, 502, 1960.

Kaiser, C. B., The Thermal Emission of the F-Corona, Ap. J. 137, 945, 1963 .

Karyagina, Z. V., V. A. Mozjaeva and P. V. Shcheglov, Hα nightglow measurements made at Alma-Ata in 1967-68, Astron. Circular USSR No. 502, 5 , 1969.

Kockarts, G. and M. Nicolet, Le Probléme Aéronomique de l'helium et de l'hydrogene neutres, Ann. Geophys., 18, 269, 1962.

Krassovsky, V. I., Atmospheric Emission of Atomic Hydrogen H from Observations at Zvenigorod, Abastumani and Alma-Ata, J. Atmos. Terr. Phys., 33, 1499, 1971 .

Krassovsky, V. I. and G. I. Galperin, Trans int. astr. Un. 10, 367, 1958.

Krassovsky, V. I. and N. N. Shefov, Atlas of the Airglow Spectrum 3000-12400Å, Planet. Space Sci., 9, 883, 1962.

Kurt, V. G. and S. B. Dostovalov, Far Ultraviolet Radiation from the Milky Way, Nature, 218, 258, 1968.

Kurt, V. G. and R. A. Syunyaev, Observations and Interpretation of Ultraviolet Radiation of the Galaxy, Astr. Zh., 44, 1157, 1967 (Engl. Trans. 1968, Soviet Astron, A. J., 11, 928).

Kvifte, G., Nightglow observations at Å s during the IGY, Geophys. Publikasjoner Geophys. Norvegica, 20 (12), 12, 1959.

Lamb, W. E., Jr. and R. C. Retherford, Fine Structure of Hydrogen Atom. by Microwave Method, Phys. Rev. 72, 241, 1947 .

Larson, H. P. and K. L. Andrew, A Least Squares Deconvolution Technique for the Photoelectric Fabry Perot Spectrometer, Appl. Opt. 6, 1701, 1967.

Liwshitz, M. and S. F. Singer, Thermal Escape of Neutral Hydrogen and its Distribution in the Earth's Thermosphere, Planet. Space Sci., 14, 541, 1966.

Lunar Sample Preliminary Examination Team, Preliminary Examination of Lunar Samples from Apollo 11, Science 165, 1211, 1969.

Mack, J. E., D. P. McNutt, F. L. Roesler, R. Chabbal, The PEPSIOS Purely Interferometric High Resolution Scanning Spectrometer I, The Pilot Model, Appl. Opt. 2, 873, 1963.

REFERENCES (continued)

Mange, P., Diffusion in the Thermosphere, Ann. Geophys. 17, 277, 1961.

McAfee, J. R., Lateral Flow in the Exosphere, Planet. Space. Sci. 15, 599, 1967.

McDaniel, E. W., Collision Phenomenon in Ionized Gases, Wiley, New York, 1964.

Meier, R. R., Balmer Alpha and Lyman Beta in the Hydrogen Geocorona, J. Geophys. Res., 74, 3561, 1969.

Meier, R. R. and P. Mange, Geocoronal Hydrogen: An Analysis of the Lyman-Alpha Airglow Observed from OGO-4, Planet. Space Sci., 18, 803, 1970.

Meinel, A. B., Hydride Emission Bands in the Spectrum of the Night-sky; Ap. J., 111 207, 1950.

Morton, D. C. and J. D. Purcell, Observations of the Extreme Ultraviolet Radiation in the Night Sky Using an Atomic Hydrogen Filter, Planet. Space Sci., 9, 455, 1962.

Morton, D. C. and K. G. Widing, The Solar Lyman-Alpha Emission Line, Ap. J. 133, 596, 1961.

Münch, G., Structural Problems of Galaxies in the Light of Lyman Alpha, in Space Age Astronomy, Eds, A. J. Deutsch and W. B. Klemperer, Acad. Press., New York, p. 219, 1962.

Nicolet, M., Ozone and Hydrogen Reactions, Ann. Geophys. 26, 531, 1970.

Nilson, J. A. and G. G. Shepherd, Upper Atmospheric Temperatures from Doppler Line Widths - I, Some Preliminary Measurements on OI 5577 Å in Aurora, Planet. Space Sci., 5, 299, 1961.

Osterbrock, D. E., The Escape of Resonance Line Radiation from an Optically Thick Nebula, Ap. J., 135, 195, 1962.

Parker, E. N., Kinetic Properties of Interplanetary Matter, Planet. Space Sci., 9, 461, 1962.

Patterson, T. N. L., The Diurnal Variation of the Atomic Hydrogen Concentration of the base of the Exosphere, Planet. Space Sci., 14, 425, 1966.

Patterson, T. N. L., Diurnal Variations in Thermospheric Hydrogen, Revs. Geophys. and Space Phys. 8, 461, 1970.

REFERENCES (continued)

Patterson, T. N. L., F. S. Johnson, and W. B. Hanson, The Distribution of Interplanetary Hydrogen, Planet. Space Sci. 11, 767, 1963.

Piotrowski, S., The Collisions of Asteroids, Acta. Astron. Series a, 5, 115, 1953.

Prokudina, V. S., Observations of the Line 6562Å in the Night Airglow Spectrum, Spectral, Electrophotometerical and Radar Researches of Aurora and Airglow, No. 1, 43-44 (Results of IGY, USSR Acad. Sci. Moscow) 1959.

Purcell, J. D. and R. Tousey, The Profile of Solar Lyman Alpha, Space Research I, 590, 1960.

Reay, N. K. and J. Ring, Radial Velocity and Intensity Measurements of the Night Sky H_β Emission Line, Planet. Space Sci., 17, 561, 1969.

Richtmeyer, Kennard & Lauritsen, Introduction to Modern Physics, 1955 (p. 260) Revised Edition, McGraw Hill Book Company.

Roach, F. E., H. B. Pettit, E. Tandberg-Hanssen and D. N. Davis, Observations of Zodiacal light, Ap. J. 119, 253, 1954.

Roble, R. G., Ph. D. Thesis, University of Michigan, 1969.

Shepherd, G. G., Applications of the Fabry Perot Spectrometer to Upper Atmospheric Spectroscopy, Colloque sur les Methodes Nouvelles Spectroscopie Instrumentale, J. Phys. 28, 301, 1967.

Shklovsky, I. S., On Hydrogen Emission in the Night Glow, Planet. Space Sci., 1, 63, 1959.

Thomas, G. E., Lyman α Scattering in the Earth's Hydrogen Geocorona, 1, J. Geophys. Res., 68, 2639, 1963.

Thomas, G. E., Properties of Nearby Interstellar Hydrogen Deduced from Lyman Alpha Sky Background Measurements, Presented at the Solar Wind Conference March 21-26, 1971 Asilomar Pacific Grove, California.

Tinsley, B. A., The Circularly Symmetric Grille Spectrometer, Appl. Optics, 5, 1139, 1966.

Tinsley, B. A., Initial Results of Geocoronal Balmer Alpha Observations, Planet. Space Sci., 15, 1757, 1967.

Tinsley, B. A., Temporal Variations in Geocoronal Balmar Alpha, J. Geophys. Res., 73, 4139, 1968.

REFERENCES (continued)

Tinsley, B.A., Anisotropic Galactic Emissions at Lyman Alpha and Nearby Wavelengths, J. Geophys. Res., 79, 2327, 1969.

Tinsley, B.A., Variations of Balmer Emission and Related Hydrogen Distributions, Space Research X, 582, 1970 .

Tinsley, B.A., Extraterrestrial Lyman-Alpha, Rev. of Geophys. Space Phys., 9, 89, 1971.

Tinsley, B. A. and R. R. Meier, Balmer Alpha Distributions over a Solar Cycle: Comparison of Observations with Theory, J. Geophys. Res., 76, 1006, 1971.

Tousey, R., J. D. Purcell, W. E. Austin, D. L. Garrett and K. G. Widing, New Photographic Spectra of the Sun in the Extreme Ultraviolet, Space Res. 4, 703, 1964.

Turgeon, E. C. and G. G. Shepherd, Upper Atmospheric Temperatures from Doppler Line Widths-II. Measurements on the OI5577 and OI6300 Å Lines in the Aurora, Planet. Space Sci., 9. 925, 1962.

Verniani, F., (editor), Physics of the Upper Atmosphere, 1971, Editrice Compositori, Bologna.

Wall, J. K., The Meteoroid Environment Near the Ecliptic in the Zodiacal Lightand the Interplanetary Medium (ed. Weinberg, NASA, SP-150), 1967.

Wegener, A., Untersuchungen über die Natur der obersten Atmosphärenschichten I, Phys. Zeitschr. Leipzig 12, 170, 1911.

Weinberg, J. L., The Zodiacal Light and the Interplanetary Medium, NASA SP-150 1967.

Weller, C.S., R.R. Meier, and B.A. Tinsley, Simultaneous Measurements of the Hydrogen Airglow Emissions of Lyman α Lyman β and Balmar α, J. Geophys. Res., 76, 7734, 1971.

Whipple, F. L., A comet Model III, The Zodiacal Light, Ap. J., 121, 750, 1955.

Williams, P. E., The Size of the Solar HII Region, Ap. J. 142, 314, 1965.

Williams, R. C., The Fine Structure of H_α and D_α under Varying Discharge Conditions, Phys. Rev. 54, 558, 1938.